Multivariable feedforward control of vibrations in multi-axes flexible structures : applications to multi-axes piezoelectric actuators

Yasser Al Hamidi

SPIM

Doctoral Thesis

école doctorale sciences pour l'ingénieur et microtechniques

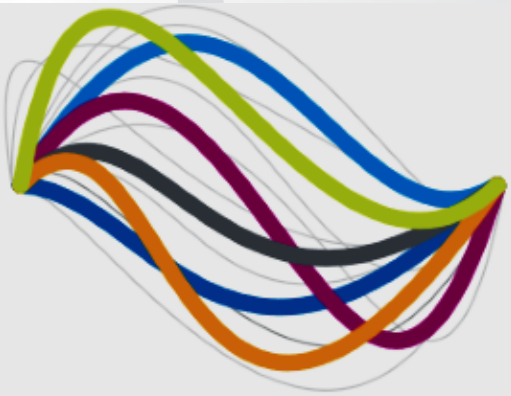

UBFC

UNIVERSITÉ
BOURGOGNE FRANCHE-COMTÉ

Multivariable feedforward control of vibrations in multi-axes flexible structures

applications to multi-axes piezoelectric actuators

Yasser AL-HAMIDI

SPIM

Doctoral Thesis

école doctorale sciences pour l'ingénieur et microtechniques

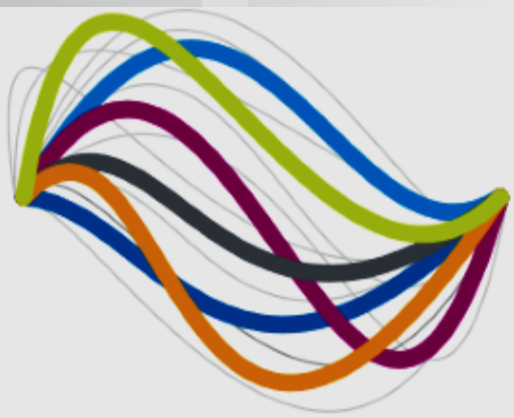

UBFC

UNIVERSITÉ
BOURGOGNE FRANCHE-COMTÉ

THESIS presented by

Yasser AL HAMIDI

Doctor's degree of
University of Bourgogne Franche-Comte´

Multivariable feedforward control of vibrations in multi-axes flexible structures

applications to multi-axes piezoelectric actuators

Research Unit: FEMTO-ST

Defended on December 14, 2017. Jury members:

Yassine HADDAB	Reviewer	Full Professor, Université de Montpellier
Antoine FERREIRA	Reviewer	Full Professor, INSA Centre Val de Loire
Mathieu GROSSARD	Examiner	Researcher, CEA Paris
Hazem NOUNOU	Examiner	Full Professor, Texas A&M University at Qatar
Philippe LUTZ	Examiner	Full Professor, Université de Franche-Comté
Micky RAKOTONDRABE	Advisor	Associate Professor with HDR, Université de Franche-Comté

Résumé:

Les actionneurs multi-axes sont de plus en plus prisés par les concepteurs de systèmes de nanopositionnement car ils permettent une réduction de l'espace occupé et de l'énergie consommée, une dextérité plus grande et une modularité avec peu de contraintes pour les applications. Certains de ces actionneurs et systèmes multi-axes sont cependant caractérisés par des oscillations mal-amorties qui compromettent de manière drastique leurs performances générales. Cette thèse concerne l'exploitation des techniques de commande en boucle-ouverte input-shaping classiquement utilisées pour amortir de manière sans capteurs les oscillations dans les systèmes mono-axes et les étendent pour qu'ils soient utilisables pour les systèmes multi-axes. Les résultats proposés dans la thèse qui sont des techniques input-shaping multivariables sont ensuite appliquées sur des actionneurs piézoélectriques classiquement dédiés pour les applications de nanopositionnement.

Abstract:

Multi-axes actuators are becoming more and more tempting to nanopositioning system designers as they enable them to save space, reduce energy consumption, increase dexterity and offer more modularity and freedom with fewer constraints to their applications. Some of these multi-axes actuators and systems exhibit however badly damped vibrations which strongly compromise their global performances. This thesis work exploits the advantages of the well-known feedforward input shaping techniques usually used to damp vibrations in monovariable (SISO) systems to present a new multivariable (MIMO) input shaping technique that can be used to damp vibrations in multi-axes systems. The approach that was used in this study is to extend a previous work that was done on multiple-input single-output (MISO) systems and generalize it for MIMO systems. The study demonstrates also the application of this newly developed technique on different piezoelectric actuators commonly used in nanopositioning systems.

Acknowledgment:

Firstly, I would like to express my sincere gratitude to my advisor Dr. Micky Rakotondrabe for the continuous support of my Ph.D. study and related research, for his patience, motivation, and immense knowledge. His guidance helped me in all the time of research and writing of this thesis. I could not have imagined having a better advisor and mentor for my Ph.D. study than him.

Besides my advisor, I would like to thank my thesis jury members: Dr. Yassine HADDAB and Dr. Antoine FERREIRA to accept to review my thesis work. Dr. Mathieu GROSSARD, Dr. Hazem NOUNOU and Dr. Philippe LUTZ to accept to be examiners.

My sincere thanks also goes to Dr. Michael Gauthier, the department head since I joined till 2016, and Dr. Philippe LUTZ, the current department head to provide me with the opportunity to join the Ph.D. school, and to ease my access to the laboratory and research facilities.

I would like to thank all nice people whom I met in the AS2M department and surrounded me with their kindness, also those whom I shared the offices with during my visits to the department.

Last but not the least, my wife for being patient and supportive during the difficult times of study and work which I went through.

SPIM

■ École doctorale SPIM 16 route de Gray F - 25030 Besançon cedex

■ tél. +33 (0)3 81 66 66 02 ■ ed-spim@univ-fcomte.fr ■ www.ed-spim.univ-fcomte.fr

UBFC
UNIVERSITÉ
BOURGOGNE FRANCHE-COMTÉ

Contents

Chapter 1

General introduction

Fields such as aerospace, biomedical and automation are increasingly reliant on microsystems to realize new concepts and configurations and to improve the performance and throughput of existent applications. The design of microsystems employs extensively smart materials due to the numerous features that do not exist in conventional materials. One of the thriving microsystems smart materials is piezoelectric materials, which occupy a growing market share estimated by around 31 billion USD. Chapter 1 of this thesis introduces some of the benchmarks in high dynamics positioning sensors and actuators' technology, and how various smart materials are embedded in a variety of applications. We shed the light on the most commonly used smart materials in the field of high dynamics positioning systems. We present a quick overview on piezoelectric materials and the qualities that made them popular. Then, we discuss nonlinearities that hinder further improvement of their performance.

Piezoelectric materials generate electric charges when subjected to mechanical stress, or deform when subjected to electrical charges. Selecting the type of piezoelectric material differs per the application, and every material offers a design trade-off. Piezoelectric materials are largely used as sensors or actuators. As sensors, the high sensing capabilities of piezoelectric materials enables designers to use them in a variety of applications such as ultrasound imaging. As actuators, the first use of piezoelectric materials was in the Atomic Force Microscope (AFM). Other applications of piezoelectric actuators extended to optical adjustment devices, piezoelectric relays, diesel fuel injectors, or micro robots to name a few. Piezoelectric components are also used in the design of miniature pumps and ultrasonic motors, which have high resolution and low noise requirements in order to function steadily.

The precise control of piezoactuators is actually a tough task due to the fact that piezoactuators possess nonlinearities and coupled dynamics. The

dynamic effects include vibrations and the creep effect. When the piezoactuator input frequency is close to the resonance frequencies, the vibrations in the output response becomes remarkably high. One approach to avoid such vibrations is to operate the piezoactuator at a frequency which is considerably lower than the dominant resonant frequency. This approach limits the use of the piezoactuators for high-speed applications like AFM. Also, at such slow operating speeds, creep becomes a main source of positioning error. Another approach is to higher the actuator resonance frequency by making it stiffer, however this reduces the actuator range of motion. Moreover, the precise control of piezoactuators is actually a more difficult task due to the fact that the hysteresis and dynamic effects of piezoactuators are coupled. Confronting these nonlinearities and badly damped vibrations calls for robust, efficient control schemes that do not impede the functions of the design or occupy more space than possible.

Feedback control schemes are generally effective in addressing external vibrations and are widely used to eliminate low frequency disturbances. Feedback is sufficient when the piezoelectric device is limited to small in-bandwidth vibration modes. Feedback control is also limited by reliance on the sensor technology, high performance sensors occupy a large space and thus cannot be easily embedded in the micro-positioning systems. Feedforward control is an alternative solution that can cover a higher bandwidth and can suppress vibrations with high frequencies or disturbances amplitudes smaller than the what feedback control-loops can detect.

Using piezoelectric materials in single axis actuation is a well-established technology and is very popular in microsystems automation. Chapter 2 presents a survey on the most commonly used feedforward techniques for single-input single-output (SISO) systems to minimize the residual vibration of flexible systems with rigid-body modes. We classify these techniques into three different categories, inversion based, time delay based and input shaping control techniques. Inversion-based feedforward control has been known to deliver accurate tracking performance in the absence of plant parameters uncertainties. In such controllers, prior information about the system under test is exploited to generate the inverse of its dynamics to use for compensation. For nonminimum-phase systems, this inversion can't be a direct-inversion due to the existence of unstable zeros, hence the need to use the so called approximate-inversions.

Another feedforward technique which was proven to be very effective in vibrations reduction and we discussed in chapter 2 is input shaping. In input shaping, the impulse sequence completely cancels residual vibration in a single mode system, as long as the natural frequency and damping ratio are perfectly known. To deal with multi-mode vibrations, input shaping

with zero placement technique allows impulse sequences to be constructed easily for systems with any number of flexible modes. Improving the robustness of SISO input shapers to account for possible modelling inaccuracies is discussed in chapter 3. In particular, the derivative constraints, which is the only possible way to improve the inherent robustness of input shapers was demonstrated. Additionally, two approaches for robustness were also discussed in this chapter. One approach is to alter the constraint of zero vibration by a constraint that limits the vibration to a small value, and the other one is to suppress a specific range of frequencies. We conclude this chapter by studying special type of command shaping that seeks to create commands that will use the maximum actuator efforts to move a system as fast as possible from one state to another, input shaping for time optimal control.

To minimize the number of actuators and simplify and streamline microsystems, developers turned their attention to multivariable actuators. Multivariable actuators enable the designers to save space and reduce energy consumption. The increasing dexterity by multivariable actuators grants the designers more modularity and freedom and less constraints on their applications. Additionally, many real flexible systems such as robots and space systems have, by nature, multiple actuators or single actuators with multiple-inputs and multiple-outputs (MIMO). Moreover, the fast and recent evolvement in the field of nanopositioning was a major drive to motivate researchers to exploit the advantages of input shaping technique so it can be extended to be used for MIMO systems, which is the core focus of this thesis. In chapter 4, we explain Pao's approach in using input shaping to control vibrations of multiple-input single-output systems (MISO) with multiple-mode of vibrations. We discuss also a modified version of this approach to shorten the shaper length to provide faster responses. Then we discuss an extension of the same approach to overcome its limitations to improve the shaper robustness with respect to either the system parameters or even one of the input matrix parameters.

We discuss also in chapter 4 the main contribution of this thesis work which is extending and generalizing Pao's MISO technique so it can be applied to damp the vibrations on multiple-input multiple-output systems (MIMO) with multiple-mode of vibrations. In this particular section of chapter 4 we present a new way for designing multivariable input shaping controller that can be used for the control of MIMO systems, and we demonstrate applying this new technique by giving examples on 2-input 2-output and 3-input 3-output systems. Finally, we discuss ways to improve the robustness of this newly developed technique at the end of this chapter.

Chapter 5 discusses different setups that were used over the course of this

study to validate the newly developed technique. The experimental setup, the characterization, the modeling and parameter estimation of three different actuators are presented in this chapter. The results of testing the newly developed multivariable technique on the three different actuators demonstrated its effectiveness in reducing vibrations of MIMO systems, which are also attached to chapter 5.

Chapter 2

High dynamics positioning based on smart materials actuators

This chapter discusses different smart materials being used in high dynamics positioning systems, their classifications and applications. The chapter focuses, in particular, on piezoelectric materials, their advantages, limitations and employment in sensors and actuators. The chapter also discusses the advantages of multiple-axis actuators over the mono ones, and presents the motivation behind the work to develop multivariable controllers for such multiple-axis actuators.

Contents

2.1 Introduction

Key industries such as aerospace, biomedical or automation are increasingly reliant on miniaturization of the mechanical systems to boost the evolutionary improvements of their designs and increase throughput of the existent applications. To meet the increasing industrial expectations, developers are continuously enhancing the key performance parameters of motion control devices, namely, actuators and sensors on the micro and nano scales.

Furthermore, miniaturized systems offer higher levels of precision and cost reduction over the life cycle of the application especially at the micro and nano scales. Microsystems appeal stems from the fact that they are highly functional and cost effective alternative to classic mechanical designs. Those miniaturized systems are progressively capable of working with new high-performance requirements in terms of force, torque, velocity or positioning resolution within a limited settling or response time in the micro and Nano scales. However, they are also increasingly confronted with mechanical disturbances which must be compensated for to obtain a satisfactory stable performance. New emerging applications included micro Unmanned Aerial Vehicles (μUAV), micro robots, Atomic Force Microscope (AFM) and micro-manipulators for cellular biology, and rotary or linear stages used in X-ray based experiments. These applications do not produce meaningful results or data unless the resolution is significantly smaller than a micron [1–3].

The design of microsystems employs the use of smart materials extensively due to numerous features that are not existent in classical materials. The concept of being responsive to numerous physical phenomena afford the control of smart materials within a limited space. By allowing the development of more competitive designs, the appealing features of microsystems' smart materials were a propelling force behind the economic growth of microsystems motion sector. One of the thriving microsystems smart materials is piezoelectric materials, which occupy a growing market share estimated around 31 billion USD. The market for piezoelectric devices is projected to grow by 4.8% by 2022 [4].

In this chapter, in Section.2.2, we introduce some of the benchmarks in high dynamics positioning sensors and actuators' technology, and how various smart materials are embedded in a variety of such applications. In Section.2.3 we shed light on the most commonly used smart materials in the field of high dynamics positioning systems. In Section.2.4 and Section.2.5, we present a quick overview on piezoelectric materials and the qualities that made them popular. Then, we discuss nonlinearities that hinder further improvement of their performance, and how feedback and feedforward controls are used to address them.

2.2 Context: High dynamics positioning

The accelerated industrial demand to integrate automation into various systems is one of the thrusting forces behind the growing performance expectations from sensors and actuators. Parameters such as velocity, position, force and torque are continuously required to be delivered with higher resolution and minimum settling or response time. Thus, to make the automation process sufficiently effective, the sensors and actuators integrated in the systems must demonstrate high precision and accuracy. Reductions in the weight, mass and cost have been a primary development direction for promoting the integration of production streamlining. In addition, increasing the throughput is contingent on reducing the settling time of the positioning actuators. These development directions dictated the agenda for manufacturers, researchers and designers since the first employments of sensors and actuators.

Historically, some of the first sensors and actuators were deployed in harsh environments and were required to manifest high levels of sensitivity and robustness in the newly emerging uncharted engineering elds. One of those rising fields was in the early 20th century, aimed at enabling the dawn of underwater engineering, submarines used hydro acoustic transducers to estimate the depth of the sea floor. Due to being isolated from land, and being challenged by the increasing pressures underwater, the newly invented submarines needed small, low-frequency, high-power transducers. In addition, sensors and transducers on board had to be as light as possible so they do not limit the presence of other systems in the submarines [5]. Later, the emergence of silicon-based piezoelectric integrated circuits in the 1950s accelerated the demand for high precision actuators that can take more loads without compromising the resolution of the actuated motion [6, 7]. The expanding industries of aerospace engineering, underwater engineering, biomedical and automotive engineering increased the need to more stable and reliable micro-positioning actuating and sensing capabilities in order to be competitive in terms of performance [8].

The exciting opportunities in the new realms of engineering cannot be reaped with establishing robust control methods to address the new challenges rising in the uncharted physical ranges. The need to develop and enhance the performance of high dynamics transducers stems from the convoluted and complex control issues and extreme operating requirements of stress, speed and stability in the nano and micro scales. The first remarkable success at those miniature scales has been the first commercialization of Atomic Force Microscope (AFM) and Scanning Tunneling Microscope (STM) at the 1980s. AFM and STM needed high resolution displacement of the sample with an extremely high resolution and minimum vibrations. In addition, the volume

allotted for the actuators was very small. This called for the development with less mechanical parts to increase the precision and reduce the weight and volume. Smart materials, especially piezoelectric materials, presented the opportunity for this development [20–24].

Micro-positioning actuators carved a place for themselves in laser optical scanning systems and optical stabilization platforms used in biology, aerospace and astronomy. A common example of the profound need for accurate responsive micro-positioning system is elevation gimbal system, which is used to track the relative velocity and position of the target. Elevation gimbal systems are commercially used in tracking the departing and arriving airplanes [14–19, 154]. The need for smaller, lighter, more accurate, precise and less complex transducers attracted developers to smart materials. The design selection of the appropriate smart material to be embedded in the actuators and sensors of motion control systems requires a deep understanding of the requirements of the system, the advantages and limitations of different smart materials. The following section discusses some of the most common smart materials in use in high dynamics applications.

2.3 Smart materials in high dynamics positioning

Smart materials are one of the most vivid research fields in materials science, therefore, encompassing all smart materials is out of the scope of this thesis. However, we glance over the most popular smart materials used in high dynamics actuation and influence the evolution of several engineering applications. In this context, smart materials can be described as materials that can sense changes in their environment and respond by changing the materials properties and/or geometry [25]. Smart materials are characterized with multiple coupled active fields. An example of this is the piezoelectric materials, where an interchanging effect takes place between the mechanical strain and electrical charges. Smart materials with ability to accurately manipulate mechanical properties are widely used in high resolution sensors and actuators. Their varieties offer a wide range of design solutions to meet diverse performance requirements and operating conditions [25, 26].

2.3.1 Classification of smart materials

Smart materials can be classified into two classes: passive and active smart materials [62]. Passive materials can act merely as sensors while active materials can act as actuators or sensors, with a few exceptions where the material can only act as an actuator such as electrothermal materials. Therefore, active materials are extensively used in positioning devices. Smart materials vary greatly in terms of their stimulus inputs and output effects. In Fig.2.1, some of the most common active materials are classified per their

input stimulus. The output effect differs from one material to another.

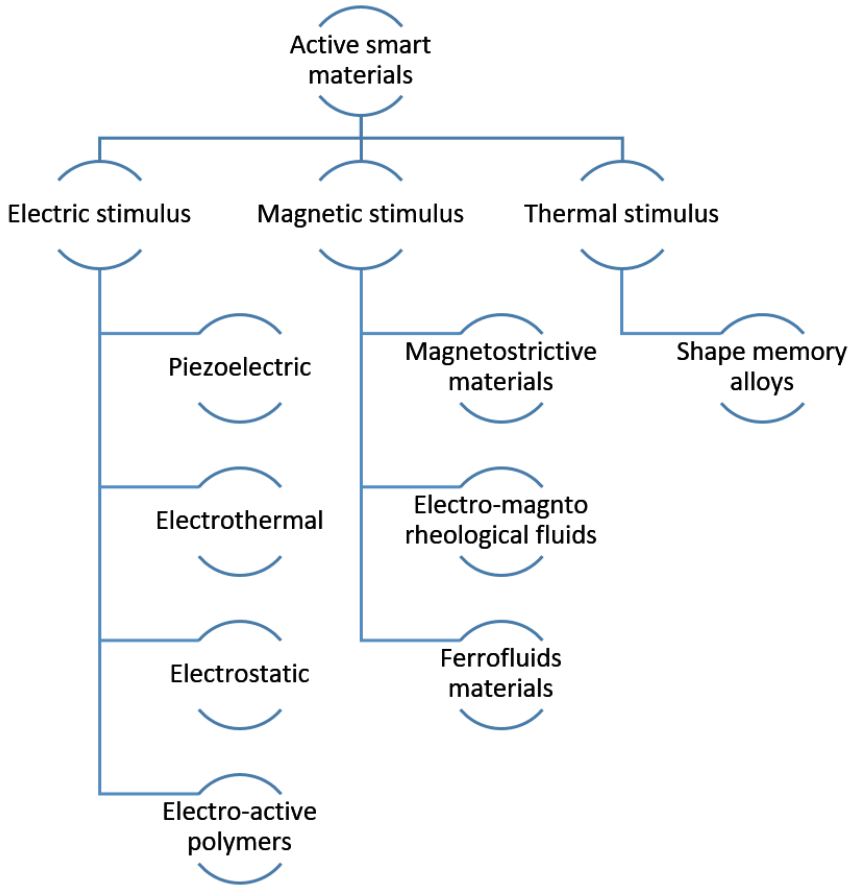

Figure 2.1: Classification of common smart materials per their stimulus.

For example, shape memory alloys retain their original shape, piezoelectric materials exhibit mechanical strain in response to electrical voltage and electro-magnetorheological fluid change their internal viscosity. The output effect of smart materials actuators can be the subject of another type of classification. This variety of the input and output endows designers with several solutions for their desired applications. Here we briefly discuss the characteristics of a few of the most common smart materials used in high dynamics positioning applications. This is by no means an inclusive list of materials as it focuses on applications pertaining to the topic of this thesis. These materials are: electrothermal, electrostatic, shape memory alloys, magnetostrictive and photostrictive materials. This section will be followed with a separate Section.2.4 to discuss piezoelectric materials as they are the main focus in this dissertation.

2.3.2 Applications Of Smart Materials

2.3.2.1 Electrothermal actuators

Electrothermal actuators are based on the thermal expansion phenomena. As the electric current heats up the active component of the actuator, the thermal expansion yields a deformation that generates a moderate amount of displacement and large amount of force used for micro positioning. Common materials for electrothermal actuators are crystal silicon and polycrystalline silicon [63]. The small amount of deflection is amplified via several geometric arrangement to produce large displacement. The electrothermal film actuators also enjoy high levels of resolution. The thermal expansion offers high amounts of force within a small area [64]. Electrothermal actuators are easy to fabricate, hence, they can be found in a wide range of MEMS actuator applications. Electrothermal actuators have been used to generate linear and/ or rotary motion [65] and multi-axis actuation [66]. Fig.2.2 shows an example for thermal bimorph actuator. To reduce the power consumption in such type of actuators, a micro position lock [68] or MEMS mechanical rack and tooth latches [69] can be designed so the actuator does not consume energy when it is locked in its position.

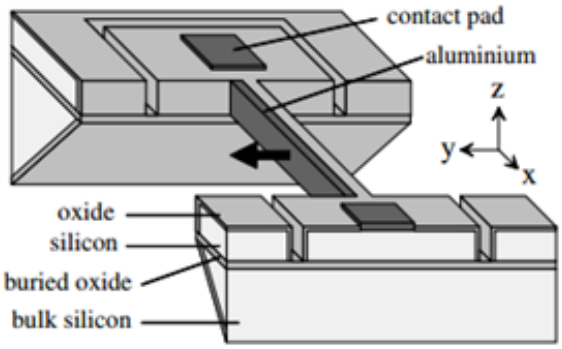

Figure 2.2: Vertical bimorph actuator [67].

2.3.2.2 Electrostatic actuators

Electrostatic actuators operate on the principle of attraction and repulsion between charged conductors. Electrostatic actuators were classically neglected since the power generated could not compare to the power output of electromagnetic actuators. However, electrostatic actuators started to find a new interest since their power output managed to compete with the power of electromagnetic actuators in the microscale [63, 70]. Electrostatic actuators are popular due to their capabilities to handle high frequencies as well as their low power consumption requirements. These two advantages,

along with reasonable ease of mass fabrications, led to their implementation in hard disk drives. Fig.2.3-(a) shows the basic mechanical components of a conventional disk drive servo system [71]. The READ/WRITE heads are fixed to the surface of a ceramic slider, which is mounted on the end of a flexible stainless-steel suspension. The base of the suspension is attached to a rigid aluminum arm, which is actuated using an electromagnetic voice-coil motor (VCM). Fig.2.3-(b) shows a secondary electrostatic actuator which is placed between the slider and gimbal of the conventional suspension. Such two-stage control systems, which utilize the VCM in combination with the high-bandwidth electrostatic actuator, were proposed as solution to overcome both the bandwidth and low frequency tracking accuracy limitations of the conventional servo system [71]. Despite of the advantages of electrostatic materials, the main drawback is that electrostatic actuators are restricted in a relatively small range of displacement and force. The maximum force obtained from a simple comb electrostatic actuator is 1 mN [63].

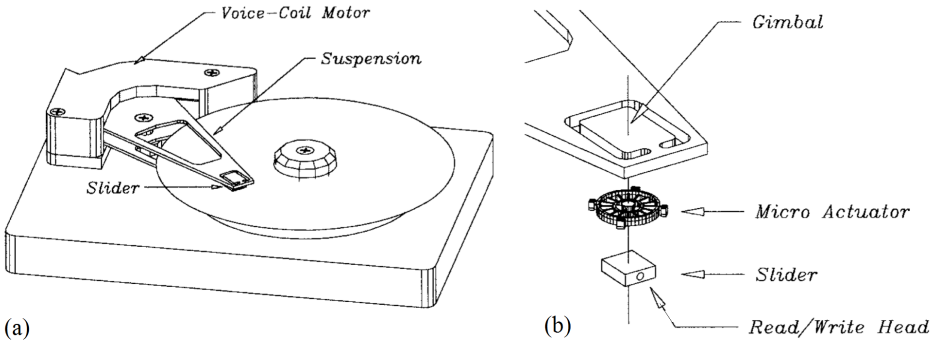

Figure 2.3: (a) The basic mechanical components of the conventional servo system (b) Exploded view of microactuator/slider assembly [71].

2.3.2.3 Shape memory alloys

One of the first smart materials which was discovered was shape memory materials, and its most common subclass of Shape Memory Alloys (SMAs) in 1932 by Arne Ölander [27]. SMAs working principle is based on recuperating the original shape after being subjected to a certain stimulus. The plastic strain recovers completely when the alloy is heated above a certain temperature known as memory transfer temperature, which is different per the alloys composition [28]. The most common commercially available memory alloys are nickel-titanium alloys, known as NiTinol and copper-aluminum-nickel alloy. A third type of SMAs is iron-based alloys. However, they are outperformed by nickel-based alloys in terms of thermo-mechanical behavior. SMAs are noted for their free recovery, constrained recovery, actuator

function, super elasticity and high damping capacity. These properties allowed the successful implementation of smart materials where the thermal effect is the main controllable stimulus.

SMAs have been used as safety and control actuators in ovens and hydraulic systems to prevent overheating [29]. SMAs possess a high force-to-weight ratio. They are compact and can be formed into any desired geometry to replace classic mechanical elements such as springs or cantilever beams. These characteristics led to the implementation of SMAs in robotics and automation applications. SMAs are also commonly used in structural biomedical applications where they can be found in bone plates. In civil engineering, SMAs are used to reduce the effect of earthquakes of environment impact. Another example of SMAs uses is couplings and fittings, which are widely used in aerospace hydraulic systems [30, 31] as show in Fig.2.4.

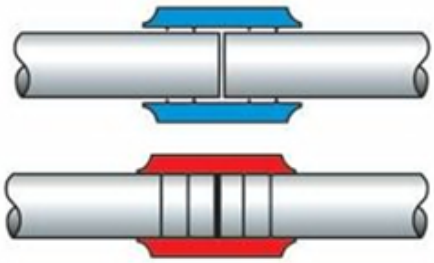

Figure 2.4: Hydraulic couplings for aerospace applications. As the coupling warms, it creates a reliable metal-to-metal seal. Courtesy: Aerofit.

In general, SMAs are advantageous in applications that requires handling substantial amounts of stress and loads due to their high materials strength and elasticity.There are a few limitations in SMAs to be considered during the design process. First, the energy efficiency of SMAs is low in comparison with alternative smart materials. SMAs convert heat into mechanical work at an efficiency that rarely exceeds 10%, which confines their implementation to applications that can afford high energy expenditure. Second, shape memory alloys have a low bandwidth since the cyclic performance requires that the alloys are being cooled down to go through another cycle. This time delay limits practicality in applications that require automated, fast repetitive actuation. SMAs suffer from high hysteresis, which limits the actuation paths. In addition, the achievable strains of shape memory alloys do not exceed 10%, thus limiting the range of positioning [32]. The temperature range of operation is also limited due to the fact that SMAs are responsive and sensitive to temperature changes.

2.3.2.4 Magnetostrictive materials

All magnetic materials exhibit physical deformation in the presence of active magnetic fields, however, some materials exhibit this change more than other, which is known as giant magnetostriction. Giant Magnetstriction is caused by either applying of magnetic field accompanied with change in magnitude and linear deformation, or by changing the direction of the field of a fixed magnitude which causes a rotating deformation. Fig.2.5 shows the deformation of the magnetostrictive materials when subjected to a magnetic field. Magnetostriction is evident in crystalline rare earth alloys. In magnetostrictive materials, magneto-elasticity occur, where change in elastic moduli accompanies changes in magnetization.

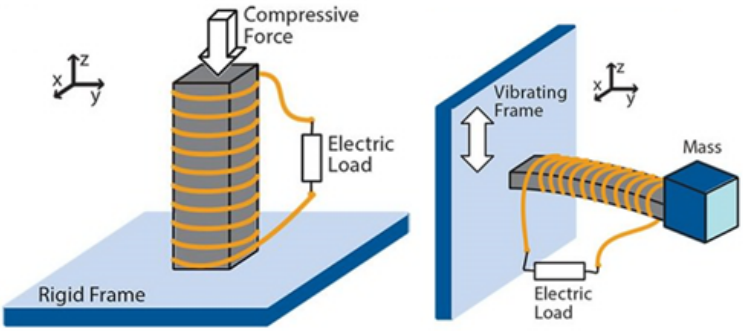

Figure 2.5: Magnetostrictive materials working principle [72].

The magnetostrictive materials offer a number of design advantages. Magnetostruictive actuators and sensors do not need a physical contact to interface with their control. Magnetorstricive materials are capable to work with high frequencies and operate in high temperature ranges. Some of the design examples include acoustic underwater systems. Developed from the magnetosrictive material, several transducers models are commercially available such as Tonpillz transducer, ring type (rare earth ring) and flextensional transducers. Due to the relatively high strain and force capability, magnetostrictive materials outperform piezoelectric materials where the actuators work directly against axial load. An example of this is diesel engine fuel injectors [14]. The transducers are bound by the properties of magnetostricive materials as the strain rates are limited, as well as the materials' tensile strength. They are usually brittle, which calls for caution in handling. The biggest limitation in the use of magnestricive material is that generating the magnetic field consumes significant amounts of energy.

2.3.2.5 Photostrictive materials

Photostrictive materials are a sub-class of smart materials that depend on the principle of light matter interaction. Subjecting the sample to light

yields strain in the sample with no significant thermal outcome. Photostrictive materials differ in compositions classification and their origin, there are four major materials groups with photostrictive material characteristics: ferroelectrics, polar, non-polar semiconductors and organic polymers. Photostrictive materials offer the advantage of dispensing of wiring unlike piezoelectric material, or magnetic field such as magnoetostrive materials. However, the displacements achieved with fast speeds are limited. Photostrictive materials have a number of developed applications such as wireless control of flexible structure, optical micro positioning, and photophones, optical projection systems and optorobots. However, a major limitation to the use of photostrictive materials is the small incremental nature of actuation, which affects the response time [33].

2.4 Piezoelectric actuators for high dynamics positioning

2.4.1 Operating principle

Piezoelectricity is the phenomena of materials to generate electrical charges when subjected to mechanical stress, or to deform when subjected to electrical charges. This is referred to as direct or inverse piezoelectric effect respectively as shown in Fig.2.6. At the molecular level, piezoelectric materials are composed of atoms of positive or negative charges that are in equilibrium. When subjected to mechanical stress (Fig.2.7), the electric equilibrium is broken, inducing a polar moment which creates charges in the materials. On the other hand, applying electric charges on the material (Fig.2.8) causes the induced displacement of atoms, thus causing deformation and displacement of the atoms of the solid structure. Quartz crystals are one example of piezoelectric materials that are commonly used for resonators. PZT ceramics (lead zirconate titanate) are common in actuator applications. Other piezoelectric materials are also found in small sensors and small actuators. They include GaAs, AlN, ZnO, and piezoelectric polymers such as PVDF [154]. Selecting the type of piezoelectric material differs per the application, and every material offer a design trade-off. The polymers are used to form into complex shapes. Ceramics offer high stiffness but are brittle.

2.4.2 Examples of applications of piezoelectric materials

Piezoelectric materials are one of the most commonly used smart materials. They are used in a variety of applications as actuators or sensors. The first use of piezoelectric actuators was in the Atomic Force Microscope (AFM), where the piezoelectric actuator controls the position of the sample as shown in Fig.2.9. Other applications of piezoelectric actuators extended to optical

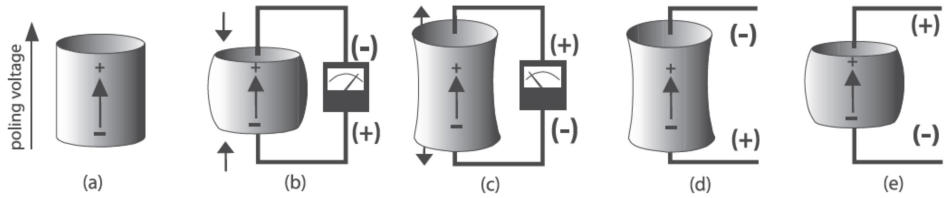

Figure 2.6: Schematic representation of direct and inverse piezoelectric effect [8].

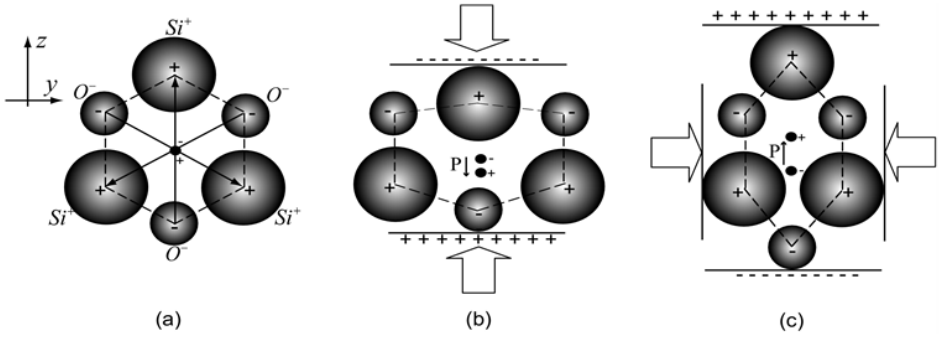

Figure 2.7: Direct piezoelectricity effect ay molcular level [153].

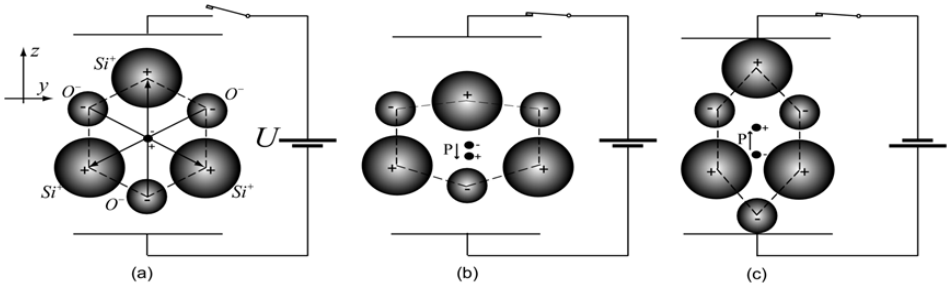

Figure 2.8: Inverse piezoelectricity effect ay molcular level [153].

adjustment devices, piezoelectric relays, diesel fuel injectors, micro robots, or micro pumps to name a few. Piezoelectric actuators can be implemented in many motor types that either depend on one-stroke principle or depend on a rotor-like principle. Some of these motors are the inchworm, micro-push motor, Padeborn Rowing motor and traveling wave motor. Piezoelectric components are used in the design of miniature pumps and ultrasonic motors, which have high resolution and low noise requirements in order to function steadily [35]. Another major application of piezoelectric materials is in micro and nano-positioning stages, which are commercially available from companies such as Physik Instrumente (PI) and NewPort. Commercial rotary actuators are based to operate within a resolution 100 nm. They offer

accurate lateral motion within three axes, X, Y and Z. Lateral and rotary actuators can be found in scanning mode or in the stepping mode. In order to ensure the high resolution of displacement range, open loop, closed loop and hybrid control schemes modes are used [36–38]. All of these aforementioned applications benefit from the extremely fast and precise response of piezoelectric materials.

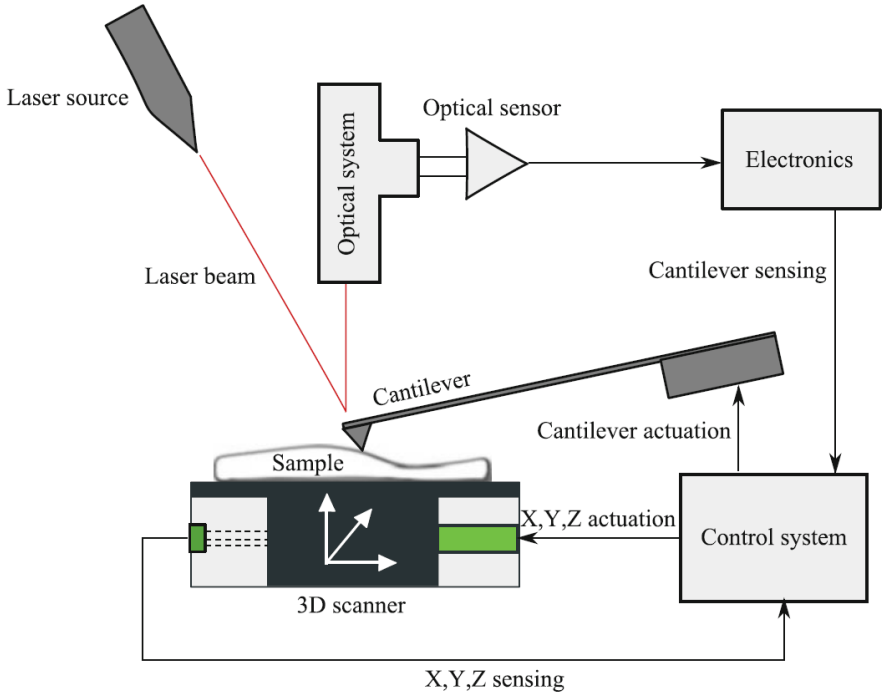

Figure 2.9: Schematic of Atomic Force Microscope (AFM) working flow [154].

The piezoelectric materials can be also deployed as sensors in applications that require high capabilities to sense pressure such as ultrasound imaging [152], where piezoelectric sensors are used to sense the high-frequency ultrasonic waves. The high sensing capabilities of the piezoelectric materials enable the designers to use them in effective control loop schemes, further reducing the error in the desired applications [34]. Piezoelectric transducers are a popular choice for structural vibration control applications. The high electro-mechanical coupling coefficient empowers piezoelectric transducers with excellent sensing and actuating capabilities. In addition, the light weight and non-intrusive nature of piezoelectric transducers implementation without compromising the structural integrity of the vibrating structure. The advantages of using piezoelectric materials are listed in Section.2.5.

The numerous applications of piezoelectric materials can not be satisfactory if the nonlinearities associated with piezoelectric structures are not compensated for. For example, the control problems of flexible structures are complex due to their high order of transfer function and various nonlinearities such as creep and hysteresis. This instigated the research to study the most effective design and control schemes to manipulate the piezoelectric structures effectively [38–40, 54].

2.4.3 Mono and multi axis actuators

Using piezoelectric materials in single-axis actuation is a well-established technology and is very popular in microsystems automation. However, to minimize the number of actuators and simplify and streamline microsystems, developers turned their attention to multi-axis actuators. Multi-axis actuators enable the designers to save space and reduce energy consumption. The increasing dexterity by multi-axis actuators grants the designers more modularity and freedom in and less constraints on their applications [42]. The development of multi-axis piezoelectric actuators is contingent on finding efficient solutions to compensate for nonlinearities, cross-couplings and badly damped vibrations. Due to the small size available for miniaturized multi-actuation devices, embedding precise feedback sensors cannot be easily implemented, thus restricting multi-axis actuations in industrial settings. This calls for the development of self-sensing based [60, 61] and feedforward control solutions.

Self-sensing of a piezoelectric actuator suggests that the actuator to utilize its direct effect in order to be its own sensor at the same time. This principle incorporates employing the charge on the actuators electrodes that appears during its deformation (actuation) to perform a measurement(sensing). Self-sensing techniques are good to be used in medium or high frequency applications. However, they lose performances when the signals involved are of low or constant frequency. This limitation hinders the utilization of self-sensing in many applications such as micromanipulation and microassembly where it is important to maintain the displacements or the forces constant during several tens of seconds [61, 146, 154].

On the other hand, feedforward techniques have been effectively presented as a solution to overcome the limitation of feedback control techniques in their needs to high performance and bulky sensors to satisfy the requirements of the micro/nano world [61]. Input shaping is one of the feedforward techniques which we discuss in the following chapters in its single-input single-out version. Then we follow this with multivariable input shaping technique which allows to deal with multi-axis actuation and is the core contribution of this dissertation.

2.5 Motivation

In this section, we list the most relevant advantages and limitations of piezoelectric actuators to our study. We also briefly present an overview of the most prominent nonlinearities affecting the performance of piezoelectric actuators and the controls used to suppress them.

2.5.1 Advantages of piezoelectric actuators

We have mentioned a few qualities that make piezoelectric materials an appealing choice for micro-positioning as cost are dropping due to high batch manufacturing techniques. Hereby, we further list those advantageous characteristics.

- High precision and accuracy: piezoelectric actuators enjoy a sub-micrometer precision. Commercial piezoelectric linear stages can constantly deliver accurate and precise micro positioning with resolution better than 10 nanometers. Any small changes in the actuation voltage are easily translated into motion.

- High bandwidth: piezoelectric materials are capable of handling high bandwidth in sensing and actuation functions. Megahertz frequencies can be sensed and actuated, which enable piezoelectric actuators to operate in a very large broad of applications, regardless of their expected frequencies.

- High force density: piezoelectric ceramics based actuators can exert high force amount relative to the voltage of actuation. Several kN can be acquired within tens of micrometers.

- High energy efficiency: piezoelectric materials do not waste large amounts of energy in by-products such as waste heat or friction. The voltage expenditure is easily translated directly into motion.

- Reduction of mechanical components: the use of piezoelectric materials assists in reducing the mechanical components typically required for motion actuation. Since the voltage is directly translated into the desired actuation, several mechanical components in intermediate kinetic transmissions are eliminated as well as several associated issues such as wear and tear and the need for lubrication.

- High range of operating temperature ranges: although major changes in the temperature will ultimately cause a drift in the results of positioning, which will require recalibration for more accurate results, piezoelectric ceramics enjoy a low thermal expansion coefficient. Therefore, piezoelectric ceramics can operate with remarkable precision in

a range of temperatures between cryogenic temperatures near 0 K to high temperatures.

As these advantages are driving the implantation of piezoelectric materials in microsystems, to reach a satisfactory performance, several inherited nonlinearities limit and degrade the quality of piezoelectric actuators output and must be confronted.

2.5.2 Limitations of piezoelectric actuators

To enhance the tracking performance of piezoelectric traducers, several nonlinearities must be compensated for. The strategies that can be adopted to counter these nonlinearities can classified into feedback, forward and hybrid control schemes. Creep, hysteresis, thermal expansion and vibrations are in the lead performance limitations. Here, we briefly discuss these limitations.

- Creep: The creep phenomenon is defined as the progressive time-dependent plastic deformation of a material under constant load and temperature. Creep in piezoelectric materials is defined as the drift in deformation after applying a constant electric field at constant temperature. The observation of creep is made by applying a step voltage to the piezoelectric actuator and record the drift that occurs right after the transient part as shown in Fig.2.10. Piezoelectric creep can result in significant loss in precision, especially when operating over extended periods of time at an offset position from the center of the piezoactuators positioning range [73].

  To model the effects of creep, the actuators outputs are measured over extended periods of time at low frequencies and low-input magnitudes, so the effects of vibrations and hysteresis nonlinearities can be neglected.

- Hysteresis: Hysteresis in piezoelectric systems is a nonlinear phenomenon in which forth and back displacement paths are different [74, 75]. The amplitude of the hysteresis h/H x 100% is calculated from the input-output map shown in Fig.2.11, and it varies according to the input voltage frequency. Hysteresis is another nonlinearity which degrades the piezoelectric actuators performance. It is path-dependent, which means that the performance of actuators, varies per its state and position. The main challenge in modeling hysteresis nonlinearity is to capture the variation of the input-to-output slope. The ascending and descending curves of the hysteresis nonlinearity tend to be different and tend to be amplitude dependent. As in the case of creep, hysteresis control is reliant on the accurate mathematical modeling to characterize and predict the behavior of the piezoelectric actuator. Some of the most cited and used hysteretic models are Preisach

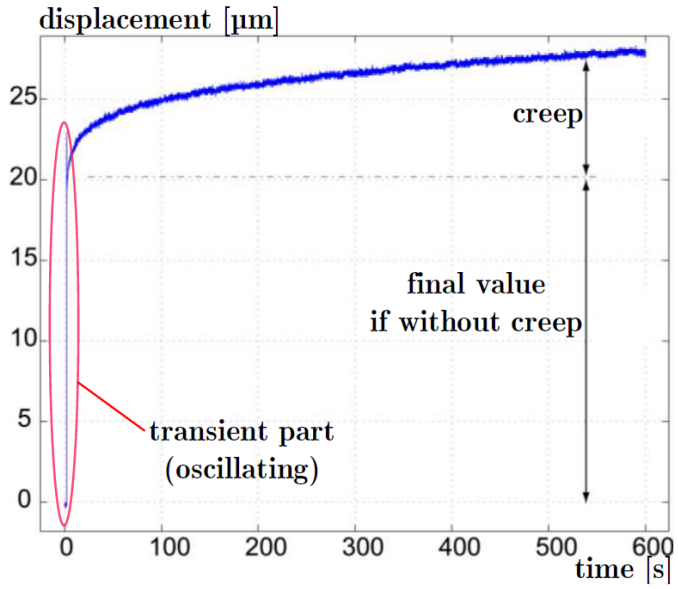

Figure 2.10: Example of creep in piezoelectric cantilever

model and PrandtlIshlinskii model [45–50]. Some of the most cited and used hysteretic models are Preisach model and Prandtl-Ishlinskii model. These models are used to predict and correct for the distortion by varying the voltage input accordingly, as shown in Fig.2.12.

- Cross-coupling: as the modern efforts are focused on the multi-axis actuators to reduce the number of embedded actuators, a new non-linearity must be considered during design. When voltage is applied through the electrodes of one axis for actuation, a smaller displacement occurs on the other axes. This effect is known as cross-coupling, and it is known to limit the performance of piezoelectric scanners used in AFM devices as it introduces large error in positioning and undesired high dynamics vibrations.

- High vibrations: highly undampened vibrations occur at positioning actuation at a fast pace from a rest position to another. High vibrations affect the quality of the output positioning and result in increased settling time. Eliminating or reducing such undesired vibrations is the core business and the main focus of this thesis.

These aforementioned unwanted characteristics cause loss of positioning precision when actuators are used during long range applications, or when positioning is needed over extended periods of time, or during high-speed positioning. Fig.2.13 shows SPM experimental results performed at low scanning

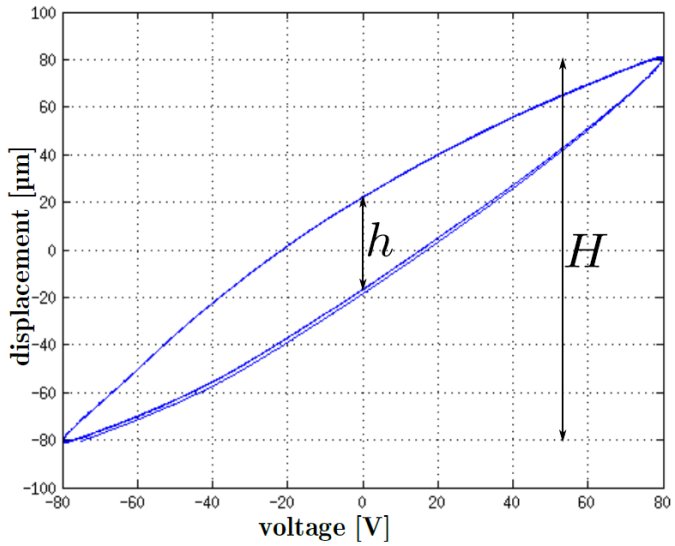

Figure 2.11: Example of Hysteresis in piezoelectric cantilever.

speeds to study the effects of hysteresis and creep. The low scanning rate allows to neglect the effects of induced vibrations. The image in Fig.2.13-a is distorted due to hysteresis and creep effects since it was obtained without any compensation compared to the image with compensation shown in Fig.2.13-d. The major cause of the shift to the image to the right is the hysteresis effect Fig.2.13-b. When the hysteresis effects are compensated, the effects of creep become dominant as shown in Fig.2.13-c. The distortions due to creep and hysteresis have been effectively removed in Fig.2.13-d which shows the importance of creep and hysteresis compensation to achieve precision scanning.

Fig.2.14 shows experimental results on the same SPM setup but performed at higher scan-rate to include induced vibrations in the study in addition to creep and hysteresis. The images to the left do not have compensation, while the images to the right are obtained after engaging the compensation. at low scanning rates like 5 Hz the vibrational effects are negligible and the main cause of image distortions is creep and hysteresis as seen in Fig.2.14-a and b. When the scan rate is increased to 30 Hz, ripples appear in the image obtained without compensation Fig.2.14-c, due to induced vibrations. Increasing the scan rate further As the scan rate is increased further Fig.2.14-e leads to severe distortions in the acquired image due the induced vibrations. The vibration-caused distortions can be greatly reduced with the addition of compensation Fig.2.14-f. As a summary, both the nonlinear hysteresis effects and the linear creep effects have to be compensated for achieving

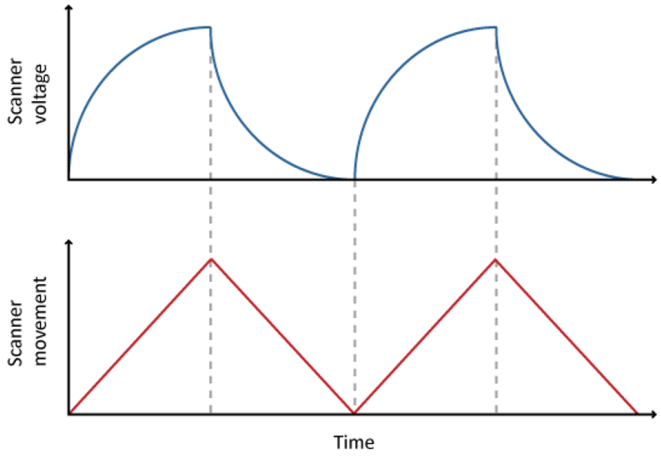

Figure 2.12: Varying the voltage input to correct for hysteresis. courtesy, DoITPoMS, University of Cambridge. [51]

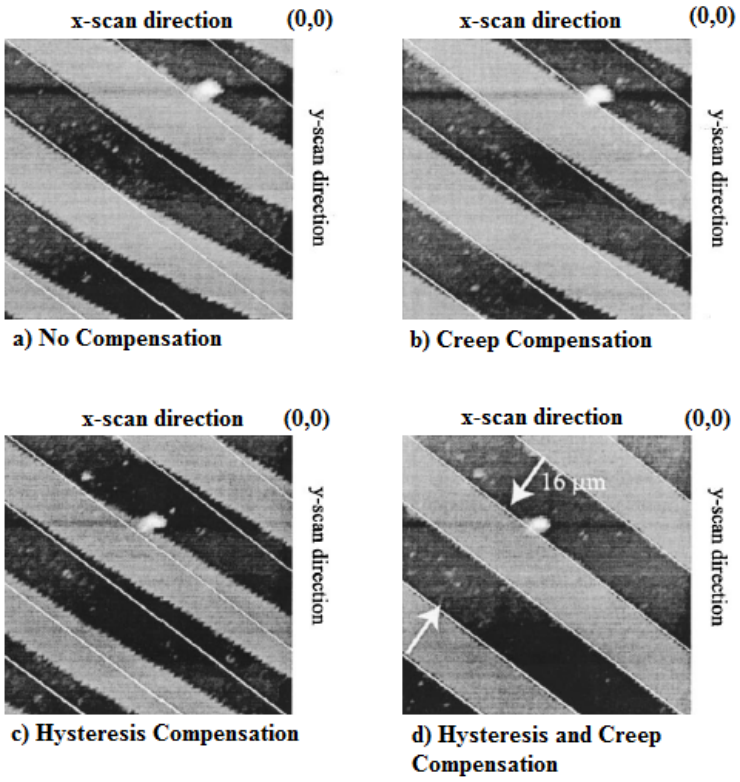

Figure 2.13: Compensation of creep and hysteresis effects at 1 Hz scanning. Parallel white lines are markers for comparison between plots [73].

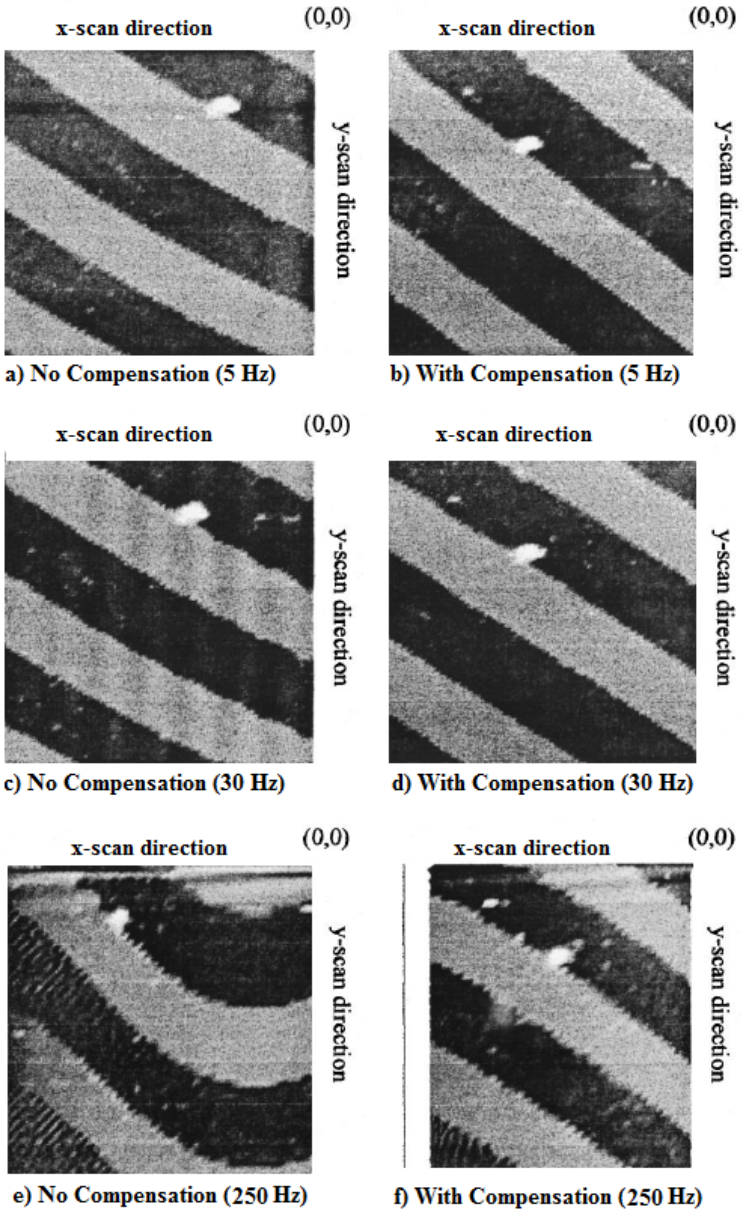

Figure 2.14: High speed compensation of plezoactuator dynamics [73].

precision scanning at low rates. Vibrations come to the picture at high scanning rate and needs to be reduced to maintain the same precision. Confronting those nonlinearities and badly damped vibrations calls for robust, efficient control schemes that do not impede the functions of the design or occupy more space than possible. Following, we compare the feedback and feedforward techniques for piezoelectric actuators.

2.5.3 Feedback and feedforward control in piezoelectric actuators

Feedback control schemes are generally effective in addressing extrinsic disturbances such external vibrations and are widely used to eliminate low frequency disturbances. In addition, they are also used to correct positioning errors from nonlinearities such as hysteresis and creep. Classic feedback control methods are widely used, such as $H_\infty$and LQG. Feedback is sufficient when the piezoelectric device is limited to a small in-bandwidth vibration modes. However, when the disturbances are out of this range, the control loops can be destabilized. Feedback controls are limited by reliance on the sensor technology. The resolution of the sensors embedded in the system limits the resolution of feedback controls to hundreds of nanometers or larger. In addition to increasing the complexity of package design, feedback controls suffer from sensor noise. Furthermore, the low bandwidth of sensors confines feedback controllers to eliminate low-frequency disturbances only. Lastly, using the sensors, which are added components to the system, increase the chances of resonance [52].

The trade-off in implementing feedback controls is that high performance sensors occupy a large space and thus cannot be easily embedded in the micro-positioning systems. The smaller feedback sensors are smaller in size and consume less energy but can hardly meet the standards for micro-positioning actuation. Alternative to dispense or reduce dependence on senor deployment were using feedforward controls or self-sensing technique, where the actuator acts a feedback sensor at the same time [53]. The biggest advantages from using the feedforward controls is covering a high bandwidth and the ability to suppress vibrations with high frequencies or disturbances amplitudes smaller than the what feedback control-loops can detect. In addition, feedforward can be used to linearize nonlinearities to facilitate the operation of feedback controls [54, 55]. Numerous open-controls are used to reduce the effects of creep and hysteresis, such as inverse control systems and Adaptive Robust Controllers (ARC) [56, 57]. Unfortunately, feedforward controllers address only displacement signals and neglect the force signals. So far, feedforward controllers have been intensively investigated with mono-axis actuators. The work in this thesis shows novel technique to use feedforward input shaping for multivariable control.

Chapter 3

Feedforward Control of Vibrations in Piezoelectric Actuators

This chapter discusses different feedforward control schemes commonly used for single-input single output (SISO) systems. The chapter attempts to categorize these different schemes based on the design approach being used to calculate the compensator, and the properness of their applications. It shows how inversion-based techniques perform very well when it comes to improving tracking errors. Zero phase and zero magnitude tracking errors, in particular, are demonstrated. It indicates also the effectiveness of different input shaping techniques in reducing or suppressing vibrations, in particular, to control vibrations in piezoelectric actuators.

Contents

3.1 Introduction

The underling principle of feedforward control is depicted in Fig.3.1. The oscillating system has a driving input u which the feedforward compensator generates by exploiting prior information about the system dynamics, and an output y which doesn't require any sensor to control. The objective is to lead y to be equal to the reference input y_{ref}, possibly just to track the input with some errors or even to deal with the vibrations suppression with or without particular specifications in the transient part. Unlike feedback controllers which react to the measured tracking error, the common thread which connects all the techniques presented in this chapter is related to the design of feedforward controllers that compensate or anticipate for deficit in performance. In this chapter we present a survey on the most commonly used feedforward techniques to minimize the residual vibrations of flexible systems with rigid-body modes. We classify these techniques into three different categories, inversion based, time delay based and input shaping control schemes as shown in Fig.3.2.

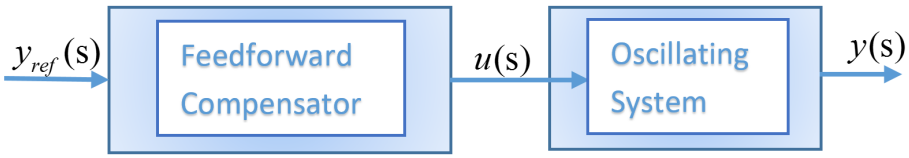

Figure 3.1: Feedforward control scheme.

3.2 Inversion based feedforward control

Research in the 1960s and 1970s showed that a system's dynamics can be inverted to find inputs that exactly track a desired output trajectory. Inversion-based feedforward control have been known to deliver accurate tracking performance in the absence of plant parameters uncertainties [78, 80]. In such controllers, prior information about the system under test is exploited to generate the inverse of its dynamics to use for compensation. In the case of piezoactuators, the dynamic effects include vibrations and the creep effect. The amount by which these dynamics affect the output response

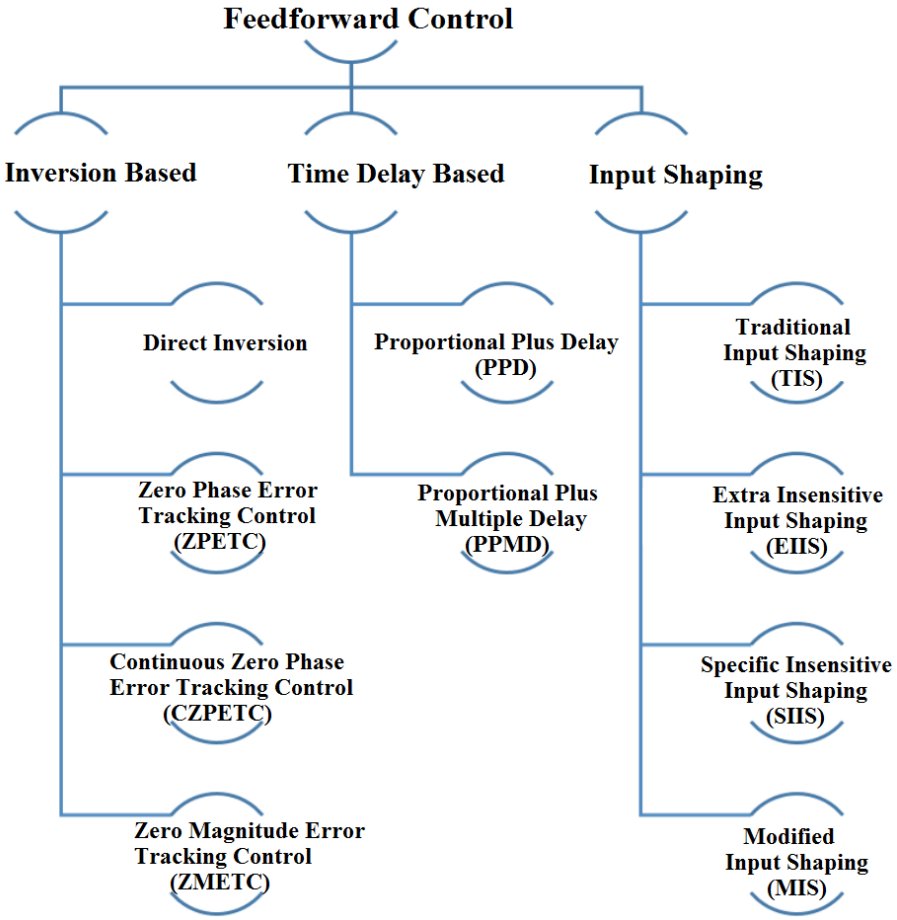

Figure 3.2: Classification of some feedforward control schemes.

depends on the inputs frequency. When this input frequency is close to the resonance frequencies, the vibrations in the piezoactuators output response becomes remarkably high [78]. Piezoactuators are also well known with their high stiffness and low structural damping which makes them highly resonant structures. This can be seen clearly in the sharp peaks appear in their frequency responses. One approach to avoid such vibrations is to operate the piezoactuator at a frequency which is considerably lower than the dominant resonant frequency [73]. This approach limits the use of the piezoactuators for high-speed applications like AFM. Also, at such slow operating speeds, creep becomes a main source of positioning error. Another approach is to higher the actuator resonance frequency by making it stiffer, however this reduces the actuator range of motion. Moreover, the precise control of piezoactuators is actually a more difficult task due to the fact that the hysteresis and dynamic effects of piezoactuators are coupled [73]. To model

and address the coupled effects of vibrational dynamics $G(s)$, creep C, and hysteresis H effects on the output of a piezoactuator, the cascade model depicted in Fig.3.3 is used extensively [78, 79]. In the figure C_c and H_c are compensators of the creep and of the hysteresis respectively, and G^{-1} is the inverse of the dynamics. Inversion-based feedforward controllers (which are model based) cannot correct for tracking errors caused by plant uncertainties, and their inputs can adversely affect the output tracking performance in the presence of large modeling errors [83,84]. Such errors can be corrected by reducing model uncertainties through feedback control, and then apply the inverse on the improved feedback system.
In the sequel and the rest of this thesis, we will not consider the creep and the hysteresis nonlinearities, as the focus of this thesis is on the multivariable input shaping control of vibrations. For the rest of this section, in Subsection.3.2.1 we discuss early works of inversion based techniques which are restricted to causal inverses of minimum phase systems [76,77]. In Subsection.3.2.2 we demonstrate how to extend the standard technique to nonminimum-phase systems by implementing non-causal inverses [81,82], as the standard or direct inversion based method leads to unbounded inputs in the nonminimum-phase situations. In Subsection.3.2.3 and Subsection.3.2.4 we discuss improved versions to the one discussed in Subsection.3.2.2.

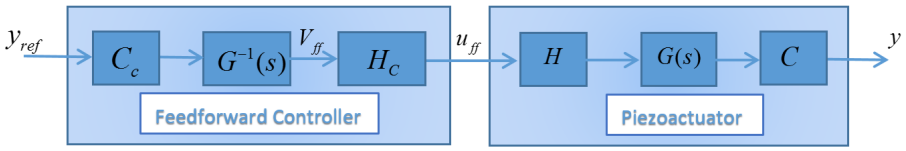

Figure 3.3: An inversion-based feedforward method to compensate for dynamics G, creep C and hysteresis H in piezoactuators.

3.2.1 Direct inversion technique

Direct inversion technique can be used with minimum phase systems. Minimum phase systems are the systems whose poles and zeroes are located on the left hand side of the S plane, thus they are by definition stable systems. If $G(s)$ represents a piezoactuator's dynamics transfer function, where the input is the applied voltage and the output is the displacement, then $G(s)$ can be expressed in the state space representation as given in Eq.3.1. In this context, the piezoactuator is assumed to be single-input single-output (SISO) system.

$$\begin{cases} \dot{x(t)} = Ax(t) + Bu(t) \\ y(t) = Cx(t) \end{cases} \tag{3.1}$$

where $x(t)$ is the state vector, $x_{ref}(t)$ is the desired state vector, $u(t)$ is the input, and $y(t)$ is the displacement output for one axis. Parameters

A, B and C are the state matrix, the input matrix and the output matrix respectively.
To find the feedforward input that exactly tracks the desired output of the system, we differentiate the output until the input appears explicitly in the expression [120]. This yields the necessary driving input $u(t)$ that satisfies the perfect tracking and ensures that $y(t) = y_{ref}(t)$:

$$u(t) = u_{ff}(t) = \left(CA^{r-1}B\right)^{-1}\left[y_{ref}^{(r)}(t) - CA^{r}x_{ref}(t)\right] \tag{3.2}$$

where $\left(CA^{r-1}B\right) \neq 0$, r is the relative degree of the system which is the difference between the number of poles and zeros of $G(s)$, and the superscript (r) denotes the r^{th} time derivative.
This equation shows clearly that a bounded solution is needed for the reference states $x_{ref}(t)$ to be able to find the inverse feedforward input $u_{ff}(t)$.

3.2.2 Zero phase error tracking control

Zero phase error tracking control (ZPETC) is a digital feedforward control algorithm for tracking desired time-varying signals. This technique is based on pole/zero cancellation. When the controlled system is nonminimum phase, the system possesses unstable zeros and this prevents the system from following arbitrary desired trajectories. ZPETC can be designed by a combination of pole/zero cancelation and phase cancelation. The latter is applied to the unstable zeros. In this approach the phase cancellation assures that the frequency response between the desired and actual outputs exhibits zero phase shift at all frequencies [85]. The rest of this subsection discusses the discrete time version of the ZPETC design, where its continuous time counterpart will be discussed in the next subsection.
Let us suppose that the controlled plant discrete time transfer function is expressed as:

$$G(z^{-1}) = \frac{z^{-d}B_c(z^{-1})}{A_c(z^{-1})} \tag{3.3}$$

where z^{-d} presents the delay caused by the plant, $B_c(z^{-1})$ and $A_c(z^{-1})$ are the system zeros and poles, respectively. We consider a feedforward controller that provides the reference control input u_r in the form of:

$$u_r(k) = \frac{A_c(z^{-1})}{B_c(z^{-1})}y_{ref}(k+d) \tag{3.4}$$

where $y_{ref}(k+d)$ is the d-step ahead desired output which the feedforward controller utilizes to compensate for the d-step delay caused by the plant. To achieve a perfect tracking, the feedforward controller should be able to cancel all poles and zeros of the system $G(z^{-1})$ such that the overall transfer function from $y_{ref}(k)$ to $y(k)$ is unity, Fig.3.4. The locations of zeros are

in particular crucial to the design of the feedforward controller. All system zeros must be inside the unit circle in the z-plane for the controller to be implementable. When $G(z^{-1})$ owns uncancellable zeros, e.g., unstable zeros, it cannot follow arbitrary desired trajectories. This problem arises in any design approach based on pole/zero cancellation [85]. To work around this

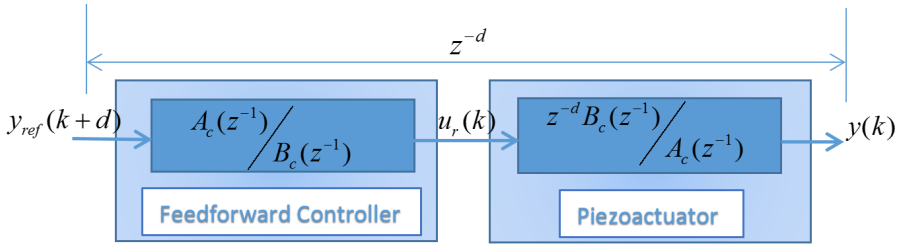

Figure 3.4: Feedforward controller for perfect tracking.

problem, we divide system zeros into two parts (B_c^a inside and B_c^u outside the unit circle) and write $B_c(z^{-1}) = B_c^a(z^{-1})B_c^u(z^{-1})$, then the proposed controller which replaces the one in Eq.3.4. becomes:

$$u_r(k) = \frac{A_c(z^{-1})}{B_c^a(z^{-1})B_c^u(1)} y_{ref}^*(k+d) \tag{3.5}$$

$B_c^u(1)$ in the denominator is to scale the DC gain of the controller to the reciprocal of that of the transfer function $G(z^{-1})$.
Using Eq.3.5, the system output can be expressed as:

$$y(k) = G(z^{-1})u_r(k) = \frac{z^{-d}B_c(z^{-1})}{A_c(z^{-1})} \cdot \frac{z^{-d}A_c(z^{-1})}{B_c^a(z^{-1})B_c^a(1)} y_{ref}^*(k+d) = \frac{z^{-d}B_c^u(z^{-1})}{B_c^u(1)} y_{ref}^*(k+d) \tag{3.6}$$

for zero initial state

$$y(k) = \frac{B_c^u(z^{-1})}{B_c^u(1)} y_{ref}^*(k) \tag{3.7}$$

If the desired trajectory can be expressed as:

$$y_{ref}(k) = [B_c^u(z^{-1})/B_c^u(1)] y_{ref}^*(k) \tag{3.8}$$

then we achieve perfect tracking $y(k) = y_{ref}(k)$.
$y_{ref}^*(k)$ represents the actual input trajectory versus $y_{ref}(k)$ which represents the desired input trajectory.
Eq.3.8 imposes the condition for perfect tracking. However, it is not always possible to generate the desired trajectory as per Eq.3.8. Additionally, even small phase error may greatly degrade the tracking performance. As shown in Fig.3.5, if y_{ref}^* can be generated from y_{ref} by:

$$y_{ref}^*(k) = [B_c^u(z)/B_c^u(1)] y_{ref}(k) \tag{3.9}$$

Then from Eq.3.5 and Eq.3.9 the feedforward controller output can be expressed as:

$$u_r(k) = \frac{A_c(z^{-1})B_c^{u*}(z^{-1})}{B_c^a(z^{-1})[B_c^u(1)]^2} y_{ref}(k+d+s) \tag{3.10}$$

where

$$B_c^u(z) = b_{c0}^u + b_{c1}^u z + ... + b_{cs}^u z^s$$
$$B_c^{u^*}(z^{-1}) = b_{cs}^u + b_{c(s-1)}^u z^{-1} + ... + b_{c0}^u z^{-s}$$
$$B_c(z^{-1}) = b_{c0} + b_{c1} z^{-1} + ... + b_{cm} z^{-m}$$
$$A_c(z^{-1}) = 1 + a_{c1} z^{-1} + ... + a_{cn} z^{-n}$$

This design is usually used in conjunction with feedback control loop for the piezoactuator. The dynamics shown in Fig.3.5 under the block which is labeled by piezoactuator includes such feedback control loop dynamics. The perfect tracking is not possible when the feedback loop possesses unstable zeros. ZPETC uses the $(d+s)$-step ahead of the desired output to assure zero phase error, where d is the number of delay steps in the close loop transfer function and s is the number of unstable closed loop system zeros. This can be seen clearly from the transfer function between $y_{ref}(k)$ and $y(k)$ that doesn't have imaginary part. The overall system has no phase shift for all frequencies, hence the resultant controller in Eq.3.10 is called the zero phase error tracking controller (ZPETC).

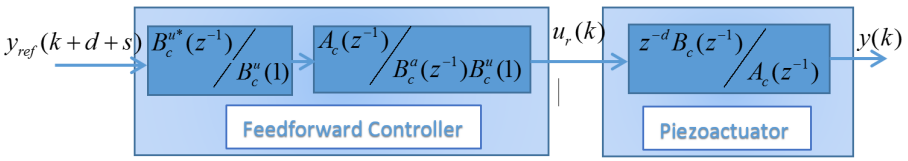

Figure 3.5: Feedforward controller for zero phase error tracking.

3.2.3 Continuous Zero phase error tracking control

In discrete time domain, fast sampling rate introduces additional unstable zeros for systems which have relative degree more than two [121]. These unstable zeros lead to tracking error which can be classified into phase error and gain error in frequency domain. Zero phase error tracking control (ZPETC) which was explained in the previous subsection is a well-known discrete-time feedforward control for tracking control of a nonminimum-phase systems. Its continuous-time counterpart version, Continous ZPETC (CZPETC), can be designed in a similar way [86]. If the plant transfer function is:

$$\frac{y(s)}{u(s)} G(s) = \frac{N(s)}{D(s)} \tag{3.11}$$

for a nonminimum-phase system, $N(s)$ can be divided into two parts for stable and unstable zeros respectively: $N(s) = N^a(s)N^u(s)$.
If the CZPETC was designed as per the following equation

$$\frac{u(s)}{y_{ref}(s)} = \frac{D(s)}{N^a(s)} \frac{N^u(-s)}{(N^u(0))^2} \tag{3.12}$$

Then the overall transfer function between the reference input $y_{ref}(s)$ and the output $y(s)$ is:

$$\frac{y(s)}{y_{ref}(s)} = \frac{N^u(-s)N^u(s)}{(N^u(0))^2} \tag{3.13}$$

Eq.3.13 shows that the overall transfer function between the desired trajectory and the output does not have an imaginary part, thus the phase shift is always zero for all frequencies. In Eq.3.12, the numerator has an order greater than the denominator, which implies that CZPETC functions as a differentiator and it is susceptible to noise.

3.2.4 Zero magnitude error tracking control

The problem with the ZPETC approach which we discussed in Subsection.3.2.2 is that it can't achieve unity gain at the same time with its zero phase, since this would require causal inversion of a nonminimum-phase transfer function. In contrast to ZPETC, ZMETC cancels the magnitude response caused by the nonminimum-phase zeros (but not the phase shift) by reflecting those zeros about the unit circle and coverting them to poles in the inverse system [122]. Starting with the nonminimum-phase zero polynomial:

$$B_c^u(z) = b_{c0}^u + b_{c1}^u z + ... + b_{cs}^u z^s \tag{3.14}$$

where s is the number of nonminimum-phase zeros. The zero magnitude error approximate inverse to B_c^u is

$$\overset{-1}{B_c}{}^u(z) = \frac{1}{b_{c0}^u + b_{c1}^u z + ... + b_{cs}^u z^s} \tag{3.15}$$

which yields the following transfer function from y_{ref} to y:

$$\frac{Y(z)}{Y_{ref}(z)} = \frac{B_c^u(z)\,\overset{-1}{B_c^u}(z)}{z^d} = \frac{B_c^u(z)}{z^d(b_{c0}^u + b_{c1}^u z + ... + b_{cs}^u z^s)} \tag{3.16}$$

Unlike ZPETC, the ZMETC only requires d samples of delay to maintain causality, which has settle time benefits. The performance of all of these aforementioned inversion based schemes depends on the location of the nonminimum-phase zeros. For systems with zeros near the unit circle, ZMETC is the only viable choice among all [123].

3.3 Time delay based feedforward control

This method of feedforward control was designed by Singh and Vadali in 1993 [87], where they showed that a single time-delay controller is equivalent to the two impulses shaped input controller, which will be presented in the input shaping techniques section later in this chapter. The basic time delay feedforward control is called proportional plus delay (PPD) controller. An extension of this is the proportional plus multiple delay (PPMD) controller. Both types will be briefly presented below.

3.3.1 Proportional plus delay (PPD)

This time-delay open loop controller for a simple harmonic system can be expressed as shown in Fig.3.6. A is the amplitude of the proportional gain

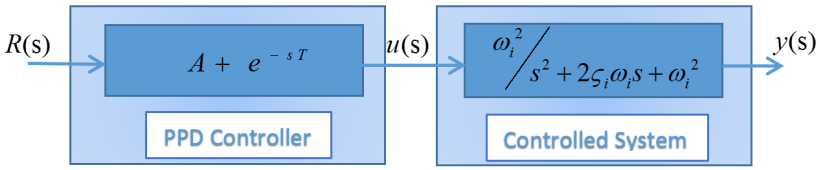

Figure 3.6: Time-Delay feedforward controller.

and T is the delay time of the time-delayed signal.
The zeros of the PPD controller should be able to cancel the poles of the controlled system. The zeros of the controller can be derived by substituting Laplace variable $s = \sigma + jw$ into the formulation of the controller and equating the real and imaginary parts to zeros. This yields the following two equations:

$$\begin{cases} A + e^{(-\sigma T)} \cos(wT) = 0 \\ e^{(-\sigma T)} \sin(wT) = 0 \end{cases} \tag{3.17}$$

This results in the following controller zeros:

$$s = \begin{cases} \frac{-\ln(A)+(2n+1)\pi j}{T} & \rightarrow \quad when\left(w = \frac{(2n+1)\pi}{T}\right) \\ \frac{-\ln(A)+2n\pi j}{T} & \rightarrow \quad when\left(w = \frac{2n\pi}{T}\right) \end{cases} \tag{3.18}$$

To cancel the system poles at $s = -\zeta_i w_i \pm j w_i \sqrt{1-\zeta_i^2}$ and by setting $n = 0$ we have:

$$\begin{cases} w = w_i \sqrt{1-\zeta_i^2} = \frac{\pi}{T} \quad \Rightarrow \quad T = \frac{\pi}{w_i \sqrt{1-\zeta_i^2}} \\ \sigma = -\zeta_i w_i \end{cases} \tag{3.19}$$

Substituting Eq.3.19 into Eq.3.17 leads to

$$A = e^{\left(\frac{-\zeta_i \pi}{\sqrt{1-\zeta_i^2}}\right)} \tag{3.20}$$

To ensure that the final value of the input (which we apply to the system after passing through the controller) to be the same as the original input command value, we divide the controller output over the final value of time-delayed controller output, so the time delayed controller becomes:

$$\frac{A + e^{-sT}}{A + 1} \tag{3.21}$$

Which corresponds exactly to the input shaping method which will be discussed in Section.3.4.

3.3.2 Proportional plus multiple delay (PPMD)

In the previous derivation of the single time-delay controller, the cancellation of the system vibrations is contingent on an exact estimation of the system poles. Adding another single time-delay controller in series to the first one (Fig.3.7) improves the time-delay controller performance against system parameters' uncertainties. Fig.3.8 shows the resultant PPMD from cascading two PPD in series, where A_1, A_2 and T can be calculated from the original single time-delay amplitude Eq.3.20 and time delay Eq.3.19. Adding one or

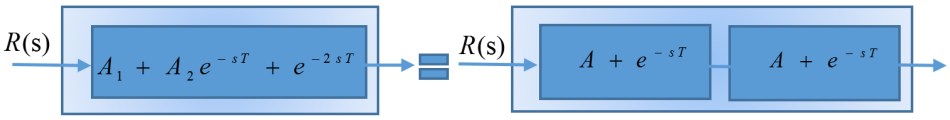

Figure 3.7: Multiple Time-Delay feedforward controller equivalent series.

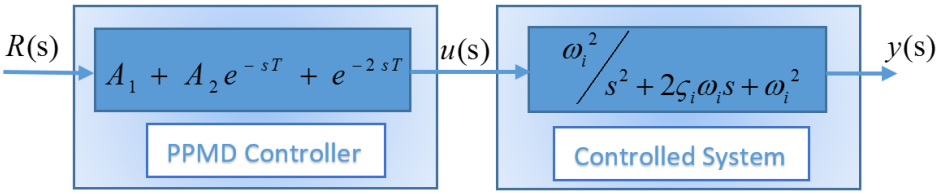

Figure 3.8: Multiple Time-Delay feedforward controller.

more time-delayed blocks in this type of controllers is equivalent to adding one or more impulse to a shaped-input controller.

3.4 Input shaping feedforward control

Input Shaping has been successfully applied for controlling flexible structures to reduce their residual vibrations since 1950's, when O.J.M. Smith developed the Posicast control which was the first self-canceling command

generation [88]. This method involved breaking a command of a certain magnitude into two smaller magnitude commands, one of which is delayed one-half period of vibration. Unfortunately, this technique was not robust to modeling uncertainties [90]. Singer and Seering developed reference commands that were robust enough to be effective on a wide range of systems [91]. This new robust technique was named as input shaping. Input shaping is implemented by convolving a sequence of impulses, with a desired system command to produce a shaped input [92]. Input shaper is designed by generating a set of constraint equations which limit the residual vibrations, maintain actuator limitations, and ensure some level of robustness to modeling errors.
Consider a second order system:

$$G(s) = \frac{y(s)}{u(s)} = \frac{G_o}{\frac{1}{(w_n)^2}s^2 + 2\frac{\zeta}{w_n}s + 1} \tag{3.22}$$

where y is the output, u is the driving input, w_n is the natural frequency, ζ is the damping ratio and G_o is the DC gain. To feedforward control this system, a compensator which is also called shaper in this case, based on an input shaping technique can be used (Fig.3.9). In the figure, y_{ref} is the reference input. The main idea of input shaping techniques revolves around

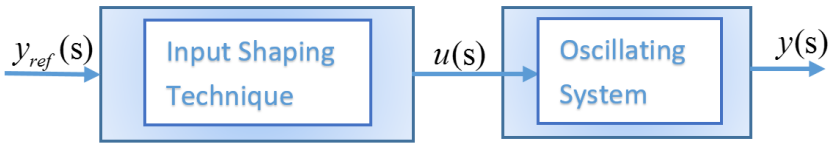

Figure 3.9: Block diagram of a feedforward control of oscillation by an input shaping technique.

applying a series of impulses as a command u to the system such that the different oscillating impulse responses suppress themselves, the response of the j^{th} impulse of amplitude and applied at time t_j being:

$$y_j(t) = G_o A_j \frac{w_n}{\sqrt{1-\zeta_i^2}} e^{-[(t-t_j)\zeta w_n]} \sin\left(w_n\sqrt{1-\zeta_i^2}(t-t_j)\right) \tag{3.23}$$

For n impulses, the impulse response can be expressed as:

$$y(t) = M\sin\left(w_d t + \phi\right) \tag{3.24}$$

where $M = \sqrt{\left(\sum_{j=1}^{n} B_j \cos(w_d t_j)\right)^2 + \left(\sum_{j=1}^{n} B_j \sin(w_d t_j)\right)^2}$, $B_j = \frac{A_j w_n}{\sqrt{1-\zeta_i^2}} e^{-\zeta w_n (t-t_j)}$, $\phi = \cos^{-1}(\zeta)$ and $w_d = w_n\sqrt{1-\zeta_i^2}$ is the damping frequency.

One important measure to characterize the damping efficiency is the residual vibrations, which is the vibrations amplitude occurs at the conclusion of a series of impulses, in particular at the final impulse time t_n. For a linear system with natural frequency ω_n and damping ratio ζ, residual vibrations are usually expressed as the nondimensional ratio of residual vibrations amplitude with shaping to that without shaping. This percentage vibrations is given by:

$$V_{(\zeta,w)} = e^{-\zeta w_n t_n} \sqrt{C_{(\zeta,w)}^2 + S_{(\zeta,w)}^2} \tag{3.25}$$

where

$$C_{(\zeta,w)} = \sum_{j=1}^{n} A_j e^{\zeta w_n t_n} \cos(w_d t_j) \tag{3.26}$$

and

$$S_{(\zeta,w)} = \sum_{j=1}^{n} A_j e^{\zeta w_n t_n} \sin(w_d t_j) \tag{3.27}$$

Each input shaping technique possesses its proper method to calculate the amplitude A_j and its application time t_j which are based on some constraints. By solving the set of constraints, the amplitudes and time locations of the impulses are determined [93]. If the constraints are minimum duration and zero residual vibrations, then the solution shaper is ZV (zero vibrations) shaper. However, ZV shaper is not well on most systems because it is sensitive to modeling errors. Robustness can be improved by adding more impulse to the shaper. The resulting shaper is a three step (TS) shaper [105]. Direct solution of amplitudes and their duration is not possible due to the inadequate number of constraint equations.

ZVD (zero vibrations derivative) shaper, as a special solution, can be obtained by setting the derivation of constraint equations with respect to the frequency of the residual vibrations equal to zero. This basically forces the residual vibrations to be minimal when the modeled frequency deviates from the actual system's natural frequency, which in turn means improved robustness as will be explained in Section.4.2.

ZVD scheme is less sensitive to timing error; however, it requires a time penalty. ZVD shaper has duration of one period of the unshaped vibration, while ZV has only a half period [94,96]. Shan in 2005 proposed a modified input shaping (MIS) method which gets a better performance, shorter length, and has the same ability of vibration suppression like other shapers [103].

3.4.1 Traditional input shaping (TIS)

Traditional input shaping requires constraints to produce a solution. Eq.3.26 and Eq. Eq.3.27 should be independently zero to achieve vibrations free response after the last impulse [104]. The sum of amplitudes of the impulses is required to be unity to ensure that the shaped command produces the same set point as unshaped motion, $\sum_{j=1}^{n} A_j = 1$.

The first impulse is applied at time zero, $t_1 = 0$. Impulse amplitudes are selected between 0 and 1 to obtain a positive shaper. If the system is solved for two impulse sequence, ZV shaper is obtained. Amplitudes and time locations of the ZV shaper is shown in Eq.3.28 as first and second rows respectively.

$$ZV = \begin{bmatrix} A_1 & A_2 \\ 0 & t_2 \end{bmatrix} \tag{3.28}$$

The solution of Eq.3.28 for a given system is:

$$ZV = \begin{bmatrix} \frac{1}{1+K} & \frac{K}{1+K} \\ 0 & \frac{\pi}{w_d} \end{bmatrix} \tag{3.29}$$

where $K = e^{\left(\frac{-\zeta_i \pi}{\sqrt{1-\zeta_i^2}}\right)}$.

To better understand the different parameters in Eq.3.28, Fig.3.10 shows the response of a system to two impulses, the second impulse cancels the vibrations induced by the first impulse [89].

3.4.2 Extra insensitive input shaping (EIIS)

The Extra Insensitive (EI) input shapers are designed by setting residual vibrations V to a nonzero value. Extra Insensitive input shapers have the same impulse times as the TIS ZVD shapers but have different amplitude values that lead to greater robustness [107]. For this type of shapers, residual vibrations remains below some tolerable level, V_{tol}, at the modeled frequency. For a system with viscous damping, the EI shaper is described by:

$$EI = \begin{bmatrix} A_1 & 1-(A_1+A_3) & A_3 \\ 0 & t_2 & T_d \end{bmatrix} \tag{3.30}$$

where

$$\begin{aligned} A_1 &= 0.24968 + 0.24962V_{tol} + 0.80008V_{tol}\zeta + 0.49599\zeta^2 + 3.17316V_{tol}\zeta^2 \\ A_3 &= 0.25149 + 0.2147V_{tol} - 0.83249\zeta + 1.41498V_{tol}\zeta + 0.85181\zeta^2 - 4.9009V_{tol}\zeta^2 \\ t_2 &= T_d\left(0.499900.46159V_{tol}\zeta + 1.75601V_{tol}\zeta^3 + 8.57843V_{tol}^2\zeta - 108.644V_{tol}\zeta^2 + 36.989V_{tol}^2\zeta^2\right) \end{aligned} \tag{3.31}$$

Section.4.3 will discuss shapers that extend this idea to have a progressively larger number of humps or the so called multi-hump EI shapers [108].

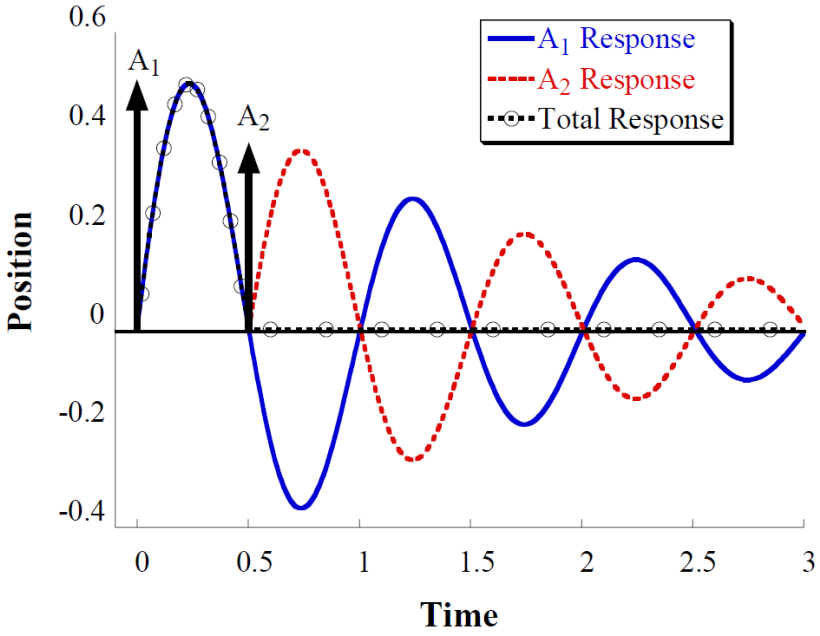

Figure 3.10: Two Impulse Response [89].

3.4.3 Specific insensitive input shaping (SIIS)

For Specified Insensitivity (SI) shapers, the constraint equations that must be satisfied do not remain fixed, rather they vary with the desired level of insensitivity. Two procedures for obtaining SI shapers will be presented in Section.4.4 when we discuss single input shapers robustness. The second procedure is more sophisticated than the first one, but yields exact solutions.

3.4.4 Modified input shaping (MIS)

The modified input-shaping (MIS) technique simplifies the shaper design by eliminating the need to use numerical optimization [103]. This technique was inspired form the component synthesis vibrations suppression (CSVS) technique proposed by Liu in [114]. The main difference between traditional input shaping (TIS), introduced earlier, and the so-called CSVS method is in the design methodology. CSVS, unlike TIS, uses analytic intuitive way to derive the input command without the need to solve nonlinear equations. Eq.3.11 (a) shows how to synthesize two commands, two impulses each, with $T/2$ time delay. Eq.3.11 (b) shows the same CSVS principle to synthesize two commands but with 3 impulses each. In the modified input shaping technique (MIS), the number of impulses can be any positive integer larger than 2. The length of the n-impulse MIS shaper is $\frac{(n-1)T_d}{n}$, which increases with the increase of n, and the minimal value is $\frac{T_d}{2}$ if $n = 2$. This technique

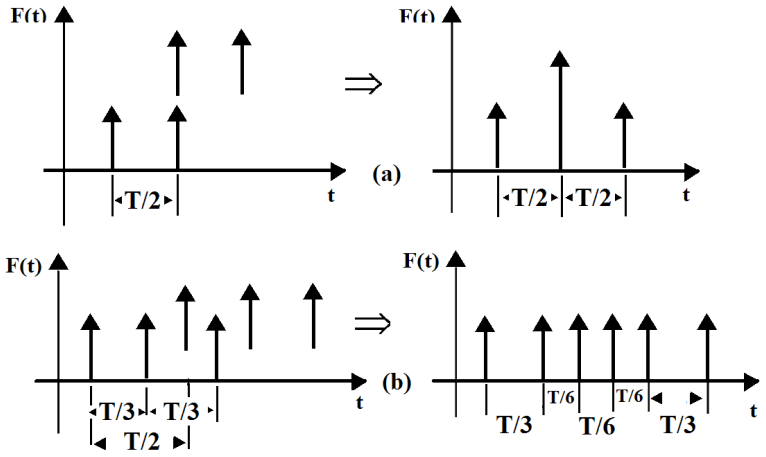

Figure 3.11: Scheme of constructing robust CSVS commands.

forms MISZV shapers that have zero vibrations at the modeled frequency, but have a larger number of impulses and longer shaper duration than the ZV shaper. An n-impulse MISZV shaper is described by:

$$MISZV_{n-impulses} = \begin{bmatrix} \frac{1}{1+M} & \frac{K}{1+M} & \cdots & \frac{K^{i-1}}{1+M} & \frac{K^{n-1}}{1+M} \\ 0 & \frac{T_d}{n} & \cdots & \frac{(i-1)T_d}{n} & (n-1)T_d \end{bmatrix} \tag{3.32}$$

where $M = K + \cdots K^{i-1} + K^{n-1}$ and $K = e^{\left(\frac{-2\zeta_i \pi}{\sqrt[n]{1-\zeta_i^2}}\right)}$.
MIS shapers are identified by impulse number and a distinguishable character MIS, i.e. 2-, 3-impulse MIS ZV shaper, etc. Here, the character MIS is added to distinguish the shapers obtained by using the MIS technique from those shapers developed by other methods.

3.5 Motivations in using input shaping approach

Vibrations are a concern of almost every mechanical system because mechanical systems vibrate when performance is pushed to the limit. The typical engineering solutions to vibrations are to design "stiffer" systems to higher the resonance frequency, add damping to flexible systems, or develop a good controller. This thesis focuses on vibrations control of piezoelectric actuators used in micro positioning systems. Piezoactuators are well known for their high stiffness and low structural damping which makes them highly resonant structures. Operating piezoactuators at low frequencies limits the use of the piezoactuators for high-speed applications like AFM. Making the piezoactuator stiffer reduces the actuator range of motion. Moreover, the precise control of piezoactuators is actually a difficult task due to the fact that piezoactuators possess nonlinearities and coupled dynamics. Confronting

those nonlinearities and badly damped vibrations calls for robust, efficient control schemes that do not impede the functions of the design or occupy more space than possible. Feedback control schemes are generally effective in addressing external vibrations and are widely used to eliminate low frequency disturbances. Feedback is sufficient when the piezoelectric device is limited to small in-bandwidth vibrations modes. Feedback control is limited by reliance on the sensor technology, high performance sensors occupy a large space and thus cannot be easily embedded in the micro-positioning systems. Feedforward control is an alternative solution that can cover a higher bandwidth and can suppress vibrations with high frequencies or disturbances amplitudes smaller than the what feedback control-loops can detect.
Previous sections of this chapter listed different feedforward techniques to use for piezoactuators, one of which is the input shaping which is the focus of this thesis. The next subsection answers the question of why input shaping is good solution for vibrations reduction.

3.5.1 Advantages of input shaping techniques

Input shaping technique has been shown to yield good performance in the control of flexible structures while being insensitive to modeling errors. The aim in input shaping is to determine the amplitudes and timing of the impulses to eliminate or reduce residual vibrations. Because only the timing and amplitudes need to be kept and only convolution needs to be performed in real-time, input shapers are a very practical method and enjoy distinct advantages in vibrations reduction.

Input shaping was originally designed to deal with single mode of vibrations. The impulse sequence completely cancels residual vibrations in a single mode system, as long as the natural frequency and damping ratio are perfectly known. To account for possible modelling inaccuracies, the shaper should exhibit some insensitivity to errors in natural frequency and damping ratio estimates. Input shaping technique can also be synthesized to take into consideration the distribution of the modeling errors and parameter variation of the system [124]. This strategy has the advantages of flexibility in choosing the range of parameter uncertainty and leads to lower levels of expected residual vibrations which can extend the lifetime of the system. Additionally, input shaping can also be used to cancel or reduce vibrations in multiple-modes systems.

Zero-placement in the discrete domain is a very common technique to be used for such systems. It provides great flexibility in shaper design that can be exploited to adjust shaper specifications to improve system performance. Intelligent placement of multiple zeros at or close to the system poles improve shaper robustness with reduced time-lag. Another powerful

tool which provides great flexibility in shaper design is the impulse amplitude plot which tells the range of acceptable shaper solutions, an intelligent choice can be made of the shaper which most effectively suits a particular system. Also, for shapers implemented on a digital computer, impulses can only be applied correctly if they fall exactly at a time-step of the digital system. Using the impulse 'amplitude plot, this requirement can be met simply by selecting a solution with an impulse spacing, T, equal to a multiple of the digital system period.

Input shaping with zero placement technique allows impulse sequences to be constructed easily for systems with any number of flexible modes. It provides a conceptually simple and highly effective approach for suppressing vibrations in flexible mechanical systems [98]. Finally, input shaping can be used to reduce the burden on the feedback controller. The feedback controller in such cases does not have to be worried about reducing vibrations induced by the reference command and its design can be primarily based on disturbance rejection and stability, which are its natural strengths.

3.5.2 Monovariable vs multivariable input shaping techniques

Many modern mechanical systems require high precision positioning control with no residual vibrations. Input shaping is one effective feedforward technique of reducing residual vibrations. Input shaping had been primarily developed for single-input single-output systems. All different types of input shaping techniques that have been introduced in this chapter fall under this category. The design of these SISO input shapers as per the impulses amplitude equations demonstrated in the previous sections is simple, straightforward and just required to know system parameters (ω_n, ζ). Improving the robustness of SISO input shapers to parameter uncertainty in the natural frequencies and the damping ratios (to guarantee a low level of residual vibrations) can be achieved by ensuring that the transfer function of the control input has zeros at the locations of the poles of the flexible system.

Many real flexible systems such as robots and space systems have multiple actuators which contribute to only single output. The design of input shapers for such multiple-input single-output systems (MISO) didn't receive enough attention from researchers and Pao was one of very few researchers to discuss input shaping design for MISO systems. In [97, 116] Pao showed that the design of MISO input shapers can be carried out in two ways, either to have all shapers for all inputs to be designed identical to each other, or to design all input shapers to coordinate with each other to fulfill the desired response. When input shapers are designed to be identical, it is only necessary to solve for one input sequence and apply it at all inputs. That is, it has been assumed in this approach that each input by itself must cancel

out any vibrations that it causes by the end of its input command. In the second approach, more information about the flexible system model is used in the design of the shapers to force them to help each other in canceling different modes of vibrations. The latter usually leads to shorter impulse sequences and thus faster output responses.

Many systems are multiple-input multiple-output (MIMO) by nature including piezoactuators which are the focus in this thesis. Designing input shapers for MIMO systems is not available in the literature. In the next chapter we introduce a new multivariable input shaping technique to reduce vibrations in MIMO systems, in particular piezoactuators, which is the main contribution of this thesis work.

3.6 Conclusions

Feedforward control exploits prior information about system dynamics to compensate for deficit in performance. Feedforward control schemes can be synthesized in many ways to achieve diverse design requirements. For example, inversion-based feedforward controllers are well-known for their effectiveness in trajectory tracking control. The compensator, in such schemes, is either formed directly by inversing the system dynamics if the system is minimum-phase, or by using ZPETC or ZMETC techniques (which are approximate inversions) if the system is nonminimum-phase. Another way to synthesize feedforward controllers is to use input shaping method where the input command is convolved with a sequence of impulses before the newly formed command is applied to the system input.

Input shaping technique has proven its effectiveness in vibrations reduction of flexible systems. The design procedure of input shapers has the advantage of being straightforward, simple to implement, and easily adjustable to various types of robustness constraints. Different types of input shapers can be selected and planned to satisfy a specific residual vibrations and robustness requirements. Adding a level of robustness adds delay to the input command. Input shaping like other feedforward techniques reduce the burden on the feedback controller when both are used together. Input shaping had been used with single-input single-output systems to cancel or reduce multiple-modes of vibrations. It was also successfully used for multiple-input (multiple actuators) systems with single-output. The focus of this thesis is to show the use of input shaping technique with multiple-input multiple-output systems with multiple-modes of vibrations, which is covered in details in the next chapter.

Chapter 4

Robust single input shaping design for vibrations reduction

This chapter discusses the main two approaches to improving robustness of input shaping techniques used for SISO systems. It clearly shows that robustness has an expense of adding delay to the shaped input commands. Input shaping for time optimal control is also being discussed in this chapter as a different form of command shaping. The chapter concludes with a detailed comparison of the different types of SISO input shaping techniques from the robustness point of view with a clear indication for the superiority of SI shapers in providing the smallest delay time.

Contents

4.1 Introduction

Input Shaping has been effectively applied to control flexible structures, and its different techniques have been shown to allow these structures to be manipulated with small residual vibrations [91–94]. However, since shaper design depends on system parameters (w and ζ), the presence of modeling uncertainties and structure nonlinearities doesn't guarantee the shaper to accomplish the expected vibrations reduction. To visualize how the shaper performs when the actual frequency or damping deviates from the modeling frequency or damping, a sensitivity curve that shows the amplitude of residual vibrations as a function of the normalized system parameters (w and/or ζ) can be plotted. Then the robustness can be measured quantitatively by measuring the width of the curve at some low level of vibrations (V_{tol}) which varies as per the design requirements. This non-dimensional robustness measure is called the shapers insensitivity. Early versions of input shaping like the ZV were limited to applications where the frequencies are well known and don't change significantly during operation. Many methods have been developed since 1980's in order to allow input shaping to be widely applicable. One way is to force the derivative of the residual vibrations, with respect to frequency, to be equal to zero. That is, additional higher-order derivatives to be formed, and set equal to zero, results in making the shapers more and more robust. The cost of each additional degree of robustness is more delay added to the shaped command. What actually happens when we add an extra derivative constraints to the shaper formulation is to place an additional zero over the flexible poles of the flexible system.

Robustness in input shaping can be categorized as: 1) Built-in robustness, or 2) Adaptive robustness. Built-in robustness aims at inherently improving the shaper robustness. More details about built-in robustness are to be discussed in the next sections of this chapter. In contrast, adaptive robust input shapers try to use feedback measurements of the system states to continually change the input shaper to improve its effectiveness. For example, the ZV shaper explained in the previous chapter can be continually changed during operation by updating the frequency, ω, which is used to calculate the shaper impulses amplitudes and impulses locations. The need to add sensors to the control system is a significant cost of adaptive input shaping. Key challenges in adaptive shaping are updating the shaper impulses promptly to achieve stable performance.

Many researchers have developed ways to use non-robust shaper and adjust its impulse amplitudes and time locations to the changing dynamic properties of the system, rather than to construct an input shaper that has inherent robustness properties. This approach can provide a faster rise time because the non-robust shaper is shorter in duration than a comparable

robust shaper. One of the earliest adaptive input-shaping methods used a frequency-domain identification structure to estimate the vibrations frequencies and then update the spacing between the shaper impulses [135,136]. The challenge with this approach is to perform the identification in real-time without placing too large of a computational burden on the control computer [137]. This approach can be modified to use other types of frequency identification methods, such as the Experimental Transfer Function Estimate approach [138]. In addition to the real-time computational burden, another significant challenge for some applications is the effect of noise which might indicate that the dynamic properties are changing mistakenly. This issue has been studied and a method to optimize solutions for systems with noise has been developed [142].

In the indirect adaptive approaches discussed above, the system parameters are identified first and then the appropriate input shaper is designed. Another approach is to create a direct adaptation algorithm that never explicitly utilizes the system parameters. Instead, direct methods adapt the input shaper directly from the system output [139–141]. In many cases, this approach can have better convergence characteristics than indirect approaches.

For the rest of this chapter, the main focus will be to discuss the derivative constraints, which is the only possible way to improve the inherent robustness of input shapers. In Section.4.2, the derivation of zero derivative robustness constraints (which is the original way of adding robustness to input shapers) will be demonstrated. Section.4.3 discusses the robustness of another approach in which the constraint of zero vibrations is altered by a constraint that limits the vibrations to a small value. Another robustness method which suppresses a specific range of frequencies is discussed in Section.4.4. The robustness of modified input shaping (MIS) is discussed in Section.4.5. Finally, The optimal time control of input shaping is being discussed in Section.4.6.

4.2 Robustification of the traditional input shaping (TIS)

Sensitivity curves are used to visualize and measure the extent to which shapers are insensitive. The sensitivity curve for a TIS ZV shaper is shown by the solid blue line in Fig.4.1. Note that the amplitude of residual vibrations is equal to zero when the normalized frequency is equal to 1. However, as the actual frequency deviates from the modeling frequency, the amount of vibrations increases rapidly. Adding additional impulse to the ZV shapers increases their robustness against parameters uncertainties. This impulse

addition actually forms a Three-Step (TS) shaper. Direct solution to determine these three-step shaper parameters is impossible owing to the insufficient constraint equations. Although we have only three equations, however three-impulse amplitudes and their time locations require solving five unknown parameters, A_1, A_2, A_3, t_2 and t_3. A specific analytical solution can be obtained by taking the derivative of the constraints in Eq.3.26 and Eq.3.27 with respect to natural frequency of the system to be equal to zero, $\frac{dC}{dw_n} = 0$ and $\frac{dS}{dw_n} = 0$, then the two derivatives can be expressed as the following:

$$\begin{cases} \frac{dC}{dw_n} = \sum_{j=1}^{n} -A_j t_j e^{\zeta w_n t_n} \sin(w_d t_j) = 0 \\ \frac{dS}{dw_n} = \sum_{j=1}^{n} A_j t_j e^{\zeta w_n t_n} \cos(w_d t_j) = 0 \end{cases} \tag{4.1}$$

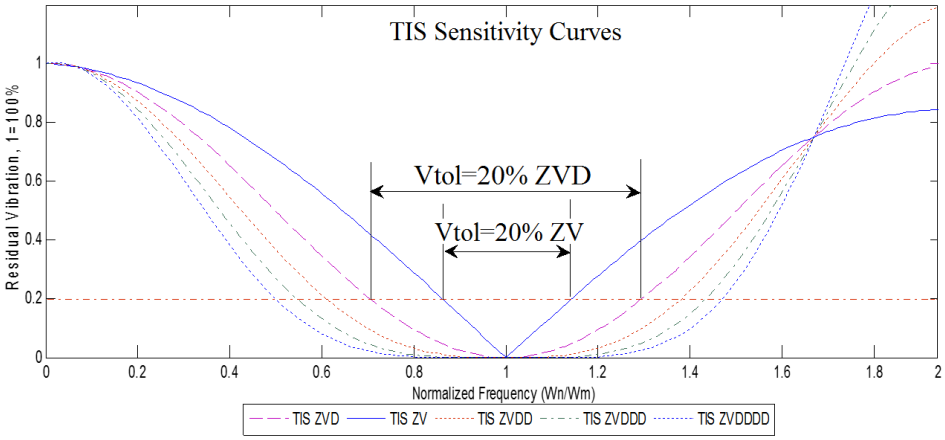

Figure 4.1: TIS Sensitivity Curves - Simulation.

The resulting shaper for such specific analytical solution is called Zero Vibrations and Derivative, ZVD. Amplitudes and time locations of the ZVD shaper is shown in Eq.4.2 as first and second rows respectively.

$$ZVD = \begin{bmatrix} \frac{1}{1+2K+K^2} & \frac{2K}{1+2K+K^2} & \frac{K^2}{1+2K+K^2} \\ 0 & \frac{\pi}{w_d} & \frac{2\pi}{w_d} \end{bmatrix} \tag{4.2}$$

The next two derivative-method shapers, the zero vibrations and double derivative (ZVDD) and zero vibrations and triple derivative (ZVDDD), are described by:

$$ZVDD = \begin{bmatrix} \frac{1}{1+3K+3K^2+K^3} & \frac{3K}{1+3K+3K^2+K^3} & \frac{3K^2}{1+3K+3K^2+K^3} & \frac{K^3}{1+3K+3K^2+K^3} \\ 0 & \frac{\pi}{w_d} & \frac{2\pi}{w_d} & \frac{3\pi}{w_d} \end{bmatrix} \tag{4.3}$$

and

$$ZVDDD = \begin{bmatrix} \frac{1}{D} & \frac{4K}{D} & \frac{6K^2}{D} & \frac{4K^3}{D} & \frac{K^4}{D} \\ 0 & \frac{\pi}{w_d} & \frac{2\pi}{w_d} & \frac{3\pi}{w_d} & \frac{4\pi}{w_d} \end{bmatrix} \tag{4.4}$$

where $D = 1 + 4K + 6K^2 + 4K^3 + K^4$.

It should be noticed that the higher the derivative-order of the shaper, the more robust the shaper becomes and the additional insensitivity the shaper gains. Fig.4.1 shows how adding additional derivative constraints flattens the sensitivity curve at the modeled frequency which in turn increases the insensitivity.
If we would like to avoid the derivation process in the design of the robust input shaper, then the three constraint equations for the five unknown parameters can be expressed in matrix form as [105]

$$\begin{bmatrix} 1 & e^{\zeta w_n t_2}\cos(w_d t_2) & e^{\zeta w_n t_3}\cos(w_d t_3) \\ 0 & e^{\zeta w_n t_2}\sin(w_d t_2) & e^{\zeta w_n t_3}\sin(w_d t_3) \\ 1 & 1 & 1 \end{bmatrix} \begin{bmatrix} A_1 \\ A_2 \\ A_3 \end{bmatrix} = \begin{bmatrix} 0 \\ 0 \\ 1 \end{bmatrix} \tag{4.5}$$

This matrix form can be rewritten for impulse amplitudes that each depends on t_2 and t_3 [105].

$$\begin{bmatrix} A_1 \\ A_2 \\ A_3 \end{bmatrix} = \begin{bmatrix} \frac{e^{\zeta w_n (t_2+t_3)}(\cos(w_d t_2)\sin(w_d t_3) - \sin(w_d t_2)\cos(w_d t_3))}{\left[e^{\zeta w_n t_2}\sin(w_d t_2)\left(1-e^{\zeta w_n t_3}\cos(w_d t_3)\right)\right] - \left[e^{\zeta w_n t_3}\sin(w_d t_3)\left(1-e^{\zeta w_n t_2}\cos(w_d t_2)\right)\right]} \\ \frac{-e^{\zeta w_n t_3}\sin(w_d t_3)}{\left[e^{\zeta w_n t_2}\sin(w_d t_2)\left(1-e^{\zeta w_n t_3}\cos(w_d t_3)\right)\right] - \left[e^{\zeta w_n t_3}\sin(w_d t_3)\left(1-e^{\zeta w_n t_2}\cos(w_d t_2)\right)\right]} \\ \frac{e^{\zeta w_n t_2}\sin(w_d t_2)}{\left[e^{\zeta w_n t_2}\sin(w_d t_2)\left(1-e^{\zeta w_n t_3}\cos(w_d t_3)\right)\right] - \left[e^{\zeta w_n t_3}\sin(w_d t_3)\left(1-e^{\zeta w_n t_2}\cos(w_d t_2)\right)\right]} \end{bmatrix} \tag{4.6}$$

This unsophisticated method for tuning the amplitudes and time locations of the three-impulse sequence input shapers helps to solve the insufficient constraint equations directly. A wide range of shapers can be obtained using this method, including Zero Vibrations (ZV), Zero Vibrations Derivative (ZVD) and Extra Insensitive (EI) or Specified Insensitive (SI) shapers. The impulse amplitudes can be produced without additional derivative constraints or an initial penalty of residual vibrations. Fig.4.2 shows the regions in terms of t_2 and t_3 where all impulse amplitudes A_1, A_2 and A_3 are positive. ZV and ZVD are referred to in the figure as special locations. All shapers in region I for example have less duration than ZVD. However, shapers in region II of the plot can give more robust shapers in reducing vibrations though its duration longer than ZVD shaper.

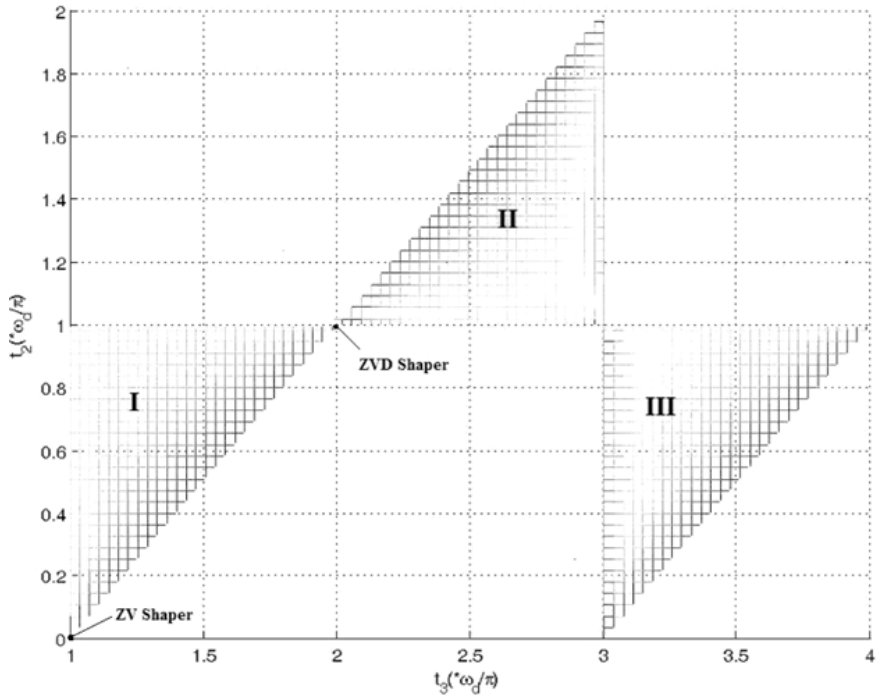

Figure 4.2: Positive TS shaper region [106].

4.3 Robustification of the extra insensitive input shaping (EIIS)

Extra Insensitive (EI) shapers have sensitivity curves similar to the ones pictured in Fig.4.3. These shapers have the same impulse times as the ZVD shapers but have different amplitude values that lead to greater robustness. As V_{tol} (the dashed red line in the figure below) increases the robustness of the shaper increases as well.
This type of shapers can be extended to have more number of humps forming the so called multi-hump EI. The sensitivity curves for two-hump EI and three-hump EI shapers are shown in Fig.4.4. Note that the three-hump EI suppresses vibrations over the entire range shown. Similar to the derivative-method shapers, this increased robustness will be on the expense of a corresponding increase in shaper duration.

Singhose et al. in [108] explain well the two-hump EI shaper derivation and shows that the impulse amplitudes and times for this shaper can be expressed as the following:

$$two-hump-EI = \begin{bmatrix} A_i \\ t_i \end{bmatrix} = \begin{bmatrix} A_{12H} & \frac{1}{2}-A_1 & A_2 & A_1 \\ 0 & 0.5\tau & \tau & 1.5\tau \end{bmatrix} \tag{4.7}$$

where τ is the vibration period which is twice of the impulse spacing T, and

$$A_1 \equiv A_{12H} = \frac{3X^2 + 2X + 3V_{tol}^2}{16X} \tag{4.8}$$

and

$$X = \sqrt[3]{V_{tol}^2 \left(\sqrt{1 - V_{tol}^2} + 1 \right)} \tag{4.9}$$

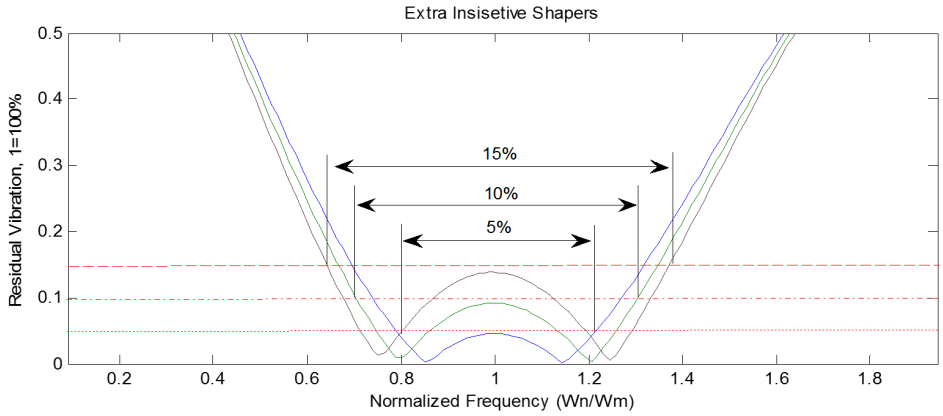

Figure 4.3: EI shapers sensitivity curves - Simulation.

For the three hump EI shapers the shaper parameters become as follows:

$$three{-}hump{-}EI = \begin{bmatrix} A_i \\ t_i \end{bmatrix} = \begin{bmatrix} A_{13H} & \frac{(1-V_{tol})}{4} & 1-2(A_1+A_2) & A_2 & A_1 \\ 0 & 0.5\tau & \tau & 1.5\tau & 2\tau \end{bmatrix} \tag{4.10}$$

where

$$A_1 \equiv A_{13H} = \frac{1 + 3V_{tol} + 2\sqrt{2V_{tol}\left(V_{tol}+1\right)}}{16} \tag{4.11}$$

Fig.4.5(a) compares the two-hump EI shaper to the traditional ZVD shaper. Although both have the same shaper length, however, the two-hump EI shaper insensitivity taken at residual vibrations level of 5% is much higher than the ZVD one. This considerable increase in insensitivity is also clear when we compare the three-hump EI with ZVDDD shaper as show in Fig.4.5(b).

When we look at the multi-hump shapers design in the S-plane, we find that the two-hump EI shapers place three zeros near the system pole. All of these zeros lie on a line of constant damping, because constraint equations force the vibrations to zero at different frequencies, but at the same damping ratio. Similarly, the three-hump EI shapers place four zeros near the modeling frequency, two on either side along a line of constant damping.

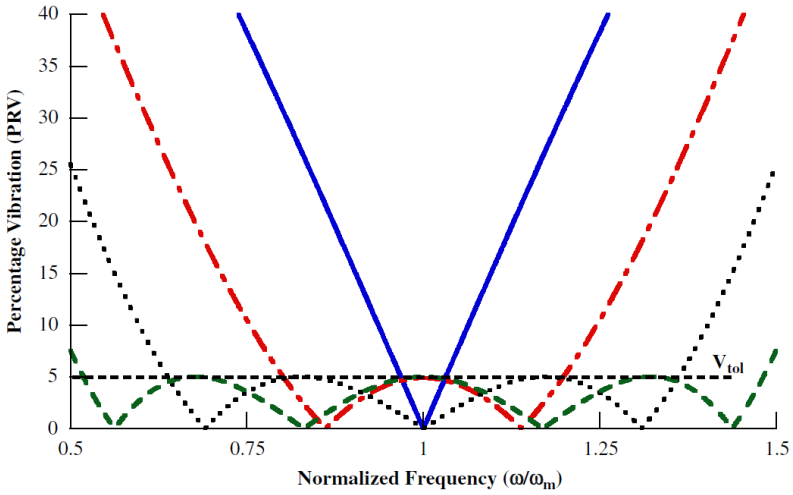

Figure 4.4: Sensitivity curves for extra insensitive method shapers, ____ zero vibrations, −.−.− extra insensitive, ... two-hump extra insensitive, − − − − three-hump extra insensitive [58].

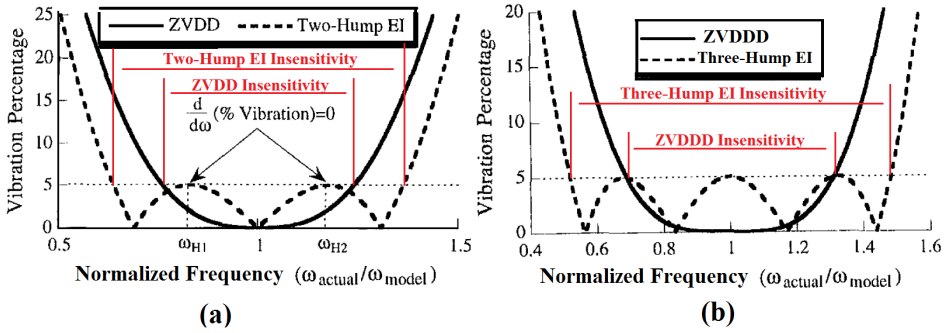

Figure 4.5: (a) Sensitivity curves of the ZVDD and two-hump EI shapers (b) Sensitivity curves of the ZVDDD and three-hump EI shapers [108] .

4.4 Robustification of the specific insensitive input shaping (SIIS)

Robustness rations for some systems may require the insensitivity of input shapers to be specified. For Specified Insensitivity (SI) shapers, the constraint equations that must be satisfied do not stay fixed, rather they vary with the desired level of insensitivity. Two ways for obtaining SI shapers will be presented in this section. The first procedure is a brute force method that yields approximate solutions with a level of approximation degree that can be easily adjusted. The second way is more sophisticated, but yields exact solutions [144].

4.4.1 Approximate SI shapers

Frequency sampling technique is the most straightforward way to obtain approximate SI shapers [143]. It requires repeated use of the residual vibrations Eq.3.25 with a tolerable level of vibrations V_{tol} to be used as the percentage vibration for each frequency sample.

$$V_{tol} \geq V_{(\zeta,w_s)} = e^{-\zeta w_s t_n} \sqrt{C^2_{(\zeta,w_s)} + S^2_{(\zeta,w_s)}} \tag{4.12}$$

where, ω_s represents the M unique frequencies at which the vibrations should be limited, and the subscript s in ω_s varies from 1 to M. For example, if an insensitivity of $I = 0.4$ is required ($\pm 20\%$), then the constraint equations should limit the vibrations to below V_{tol} at the specified frequencies between $0.8\omega_m$ and $1.2\omega_m$. Fig.4.6(a) illustrates this procedure, where the amplitude of residual vibrations is constrained at a regular sampling period over the frequency interval of interest for $V_{tol} = 5\%$.

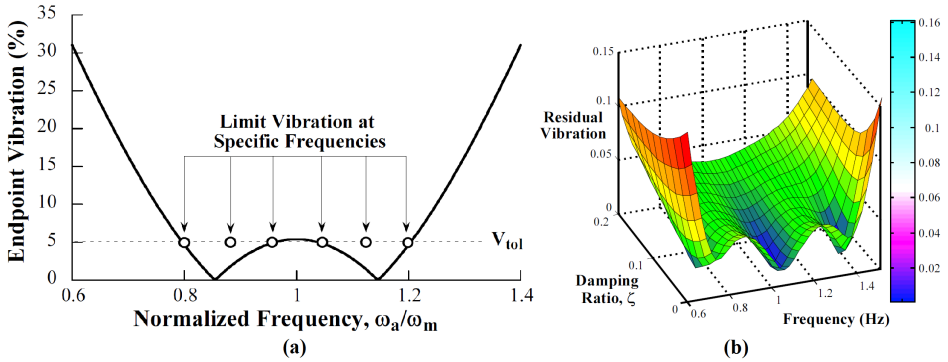

Figure 4.6: (a) Frequency sampling to suppress a range of frequencies (b) Three-dimensional sensitivity curve of an SI shaper designed to suppress a range of Frequencies and damping ratios [143].

In most of the cases, the shapers designed using this procedure will have sensitivity curves that exceed V_{tol} at some frequencies within the range of frequencies for which the vibrations are being suppressed. Increasing the frequency points, which in turn means increasing the constraint equations, forces the accuracy of the solution to approach the exact solution. This design procedure can easily be extended to obtain robustness to modeling errors in the damping ratio. Constraints are simply added to the formulation to limit the residual vibrations over a range of damping ratios. For example, Fig.4.6(b) shows the sensitivity curve for an SI shaper that was designed to suppress vibrations over a range of frequencies from 0.7 Hz to 1.3 Hz, and also over a range of damping ratios from 0 to 0.2. By using such three-dimensional plot, we can generate 2D sensitivity curve by fixing one of the ζ or ω_n parameters . If we chose to fix the frequency, then the

2D sensitivity curve will show the residual vibrations with respect to the damping ζ variations.

4.4.2 Exact SI Shapers

The previous approximate SI method is useful to limit vibrations amplitude to $V_{tol}\%$ over most of the frequency range of interest. However, limiting vibrations to less than $V_{tol}\%$ over the entire range would require solving an infinite number of frequency sampling constraint equations. Exact SI method obtains the exact robustness solutions with very few constraint equations. The method consists of five steps:

1) Determine the minimum number of sensitivity curve humps, H, required to achieve the desired insensitivity I.
2) Limit the residual vibrations amplitude to below $V_{tol}\%$ at the frequencies at the edges of the insensitivity range$(1 \pm 0.5I)\omega_m$.
3) Set the residual vibrations to $V_{tol}\%$ and the slope of the sensitivity curve to zero at the H unknown hump frequencies.
4) Limit the residual vibrations amplitude to zero at $H + 1$ unknown frequencies.
5) Solve the constraint equations generated by steps 1 to 4, in addition to the unity and positive impulse amplitudes constraint equations.

The process of generating constraint equations for the exact SI shaper with $H = 2$ and $V_{tol} = 5\%$ is shown graphically in Fig.4.7.

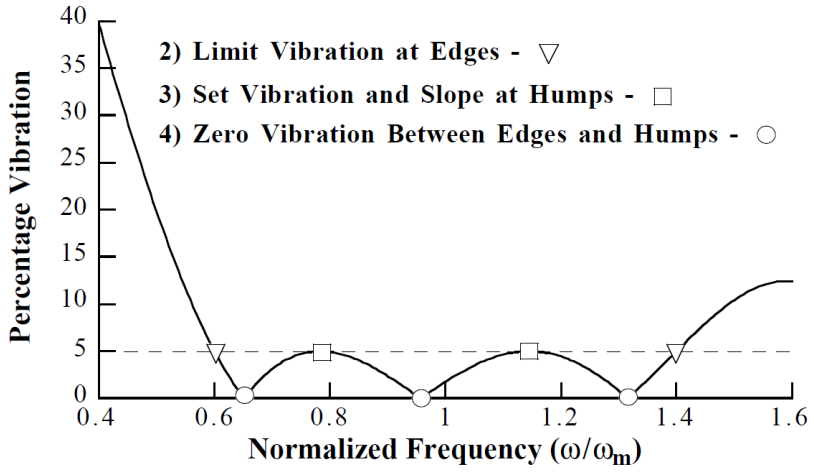

Figure 4.7: Constraint generation for exact SI shaper when H=2 and $V_{tol} = 5\%$ [144].

4.5 Robustification of the modified input shaping (MIS)

When it comes to the MIS shapers, the improvement in robustness to system parameter variations can be realized by convolving two MISZV shapers designed for the same frequency. These MISZV shapers could be (as an example) two arbitrary 2-impulse shapers as shown in Fig.4.8 (a), or two identical 2-impulse MISZV shapers that results in the MISZVD shaper shown in Fig.4.8 (b) or even two different length MISZV shapers as shown in Fig.4.8 (c). The resulting MISZVD shaper is indicated by the number of impulses of each of the MISZV shapers used to create it. An $N \times M$-impulse MISZVD is formed by convolving an MISZV shaper containing N impulses with an MISZV shaper with M impulses. Convolving MISZV shapers of higher number of impulses results in more robust MISZVD shapers, at the cost of increased shaper duration. It should be noted that the 2×2-impulse MISZVD shaper shown in Fig.4.8 (b) is the traditional ZVD shaper. A 2×3-impulse MISZVD has the following expression [103]:

$$MISZVD_{2\times 3} = \begin{bmatrix} \frac{1}{1+M} & \frac{K^2}{1+M} & \frac{K^3}{1+M} & \frac{K^4}{1+M} & \frac{K^5}{1+M} & \frac{K^7}{1+M} \\ 0 & \frac{T_d}{3} & \frac{T_d}{2} & \frac{2T_d}{3} & \frac{5T_d}{6} & \frac{7T_d}{6} \end{bmatrix} \tag{4.13}$$

where $M = K^2 + K^3 + K^4 + K^5 + K^7$ and $K = e^{\frac{-\zeta\pi}{3\sqrt{1-\zeta^2}}}$.

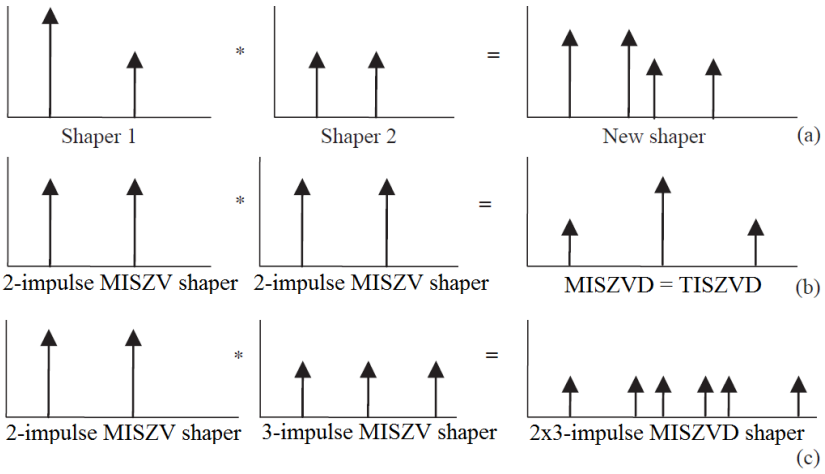

Figure 4.8: Convolution process of two shapers: (a) arbitrary two shapers, (b) two identical MIS ZV shapers, (c) two different MIS ZV shapers [103].

The sensitivity plots for 2-impulse through 6 impulse MIS ZV input shapers are shown in Fig.4.9. One can see that the additional impulses only provide a minimal increase in shaper insensitivity about the modeled frequency. However, if we zoom out a bit to see the MIS ZV sensitivity curves over a

wider range of frequencies, it can be seen from Fig.4.10 that MIS ZV shapers can suppress not only one mode of vibration with frequency ratio 1 but also infinite vibrations modes with specified frequencies which vary depending on the number of impulses.

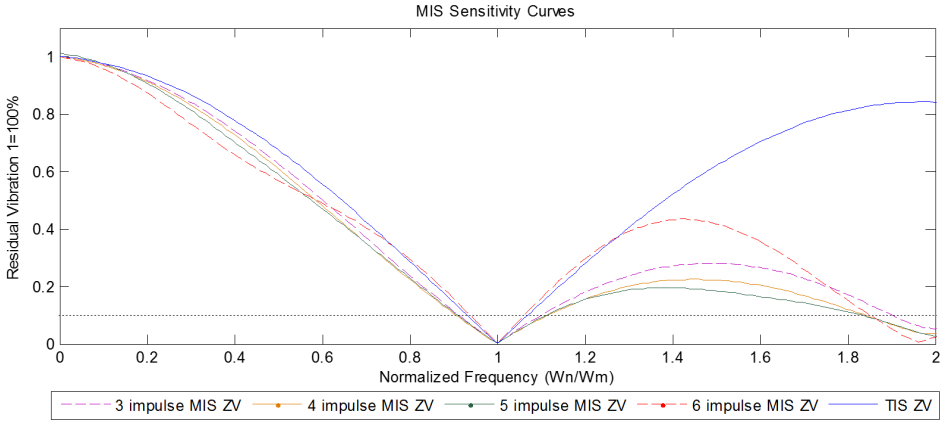

Figure 4.9: MIS ZV shapers sensitivity curves - Simulation.

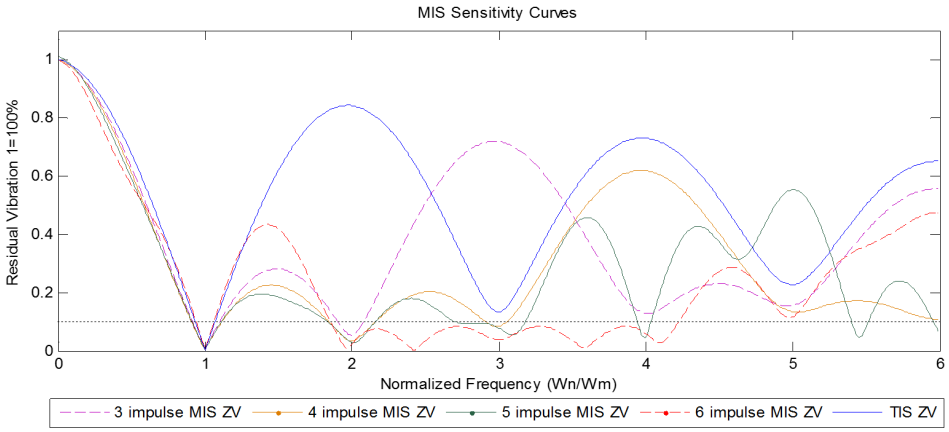

Figure 4.10: MIS ZV shapers sensitivity curves with wider range - Simulation.

Similar to traditional input shapers, increasing the degree of robustness in modified shapers flattens the sensitivity curves about the modeled frequency, however increasing the number of impulses for the MIS ZVD shapers only provides a minimal increase in shaper insensitivity like MIS ZV shapers. Shapers with higher robustness can be obtained by convolving multiple shapers with lower robustness; and an arbitrary number of shapers can be convolved to form a new shaper with expected robustness and characteristics.

For example, the convolution of a 2-impulse MIS ZV shaper with a 2×3-impulse MIS ZVD shaper can result in a $2 \times 2 \times 3$-impulse MIS ZVDD shaper; the convolution of a 2×2-impulse MIS ZVD shaper with a 2×3-impulse MIS ZVD shaper can result in a more robust $2 \times 2 \times 2 \times 3$-impulse MIS ZVDDD shaper, etc [103].

4.6 Input shaping for time optimal control

Input shaping for time-optimal control of flexible systems is a special type of command shaping that seeks to create commands that will use the maximum actuator efforts to move a system as fast as possible from one state to another. This approach, like other input shaping techniques, requires a good model of the system dynamics and a good knowledge of actuator limits. The constraint equations used to design an input shaper usually require positive values for the impulse amplitudes. However, delay time can be considerably reduced by permitting the shaper to have negative impulses [99]. In such shapers, the positive amplitude constraint is abandoned and altered by constraining the partial sums of the amplitudes of the impulses to be less than one to guarantee that actuator limits are not exceeded. When solving with this constraint, the impulse amplitudes vector becomes in the form of [95]

$$a = \begin{bmatrix} 1 & -2 & 2 & -2 & .... & -2 & 2 \end{bmatrix} \tag{4.14}$$

This sequence when convolved with step input works very well as shown in Fig.4.11 (a). However, most real input commands contain step changes which if convolved with the same sequence will result with short periods of overcurrenting as shown in Fig.4.11 (c). Although this overcurrenting is tolerable in some cases, however, eliminating it is desirable in most of the cases. One way to prevent this overcurrenting is to alternate the impulses amplitudes to have unity magnitude as shown in Fig.4.11 (a). The amplitudes vector becomes of the following form:

$$a = \begin{bmatrix} 1 & -1 & 1 & -1 & .... & -1 & 1 \end{bmatrix} \tag{4.15}$$

Then the problem of designing the time-optimal command is simplified to just finding the impulse time locations. The equivalence of time-optimal control and input shaping using special negative input shapers has been demonstrated in [100]. There have been numerous computational approaches presented to deal with the effect of flexibility. Most of these deal with single input rest-to-rest problems under two classes: near minimum-time control and exact minimum-time control. The first category is based on smooth approximations to the time-optimal control for an equivalent rigid body. This is applicable where the applied input can be smoothly varied and are not restricted to an on-off set. The second category studies the exact time-optimal control problem. Singh and Vadali [114] proposed a frequency domain method for the design of exact time-optimal (on/off) controllers for

flexible structures. The inspiration behind their work was the fact that a bang-bang input can be regarded as a summation of time-delayed step commands. They posed the problem as a design of time-delay filter that cancels all the poles of the system and satisfies the rigid body boundary conditions. That is, they made use of the idea that locating multiple zeros of the time-delay filter at the estimated location of the system poles, results in robustness to modeling uncertainties. This fact is utilized to develop constraint equations to design time-delay filters with multiple zeros at specified locations. The output of these time-delay filters subject to a step input are the optimal switching control profiles as shown in Fig.4.11 (a).

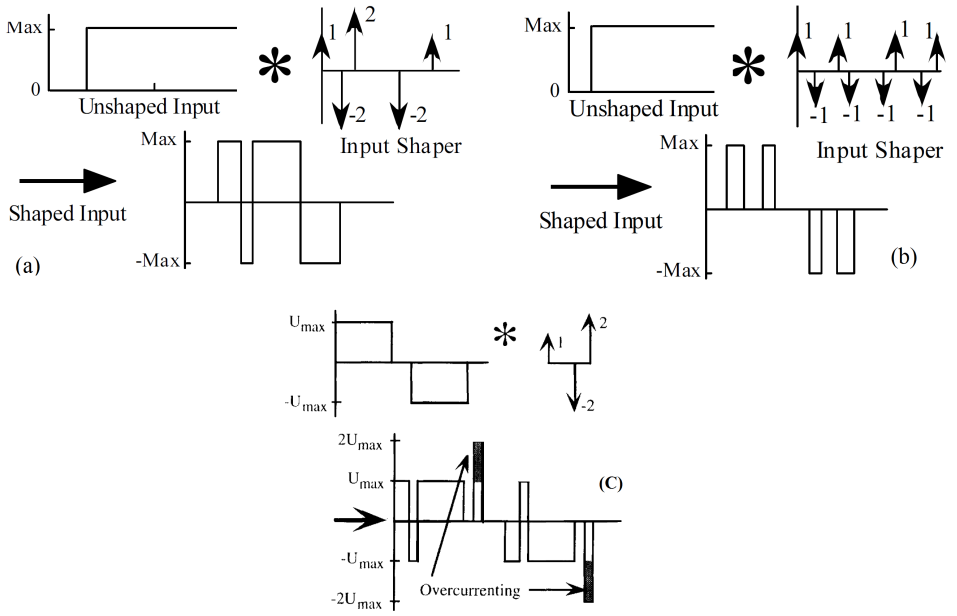

Figure 4.11: (a) Input-Shaping Process to Generate Time-Optimal Commands, (b) Input Shaping Process to Generate Fuel-Efficient On/Off Commands. [129]

The generic transfer function of a time-delay filter is:

$$G(s) = \sum_{i=0}^{N} A_i \exp(-sT_i) \tag{4.16}$$

where N is the filter stages, $T_0 = 0$ and A_i belongs to the set $A_i = \begin{bmatrix} -2 & -1 & 1 & 2 \end{bmatrix}$ to guarantee that the output of the time-delay filter is either bang-bang or bang-off-bang. For rest to rest maneuver of flexible structures, the constraint which guarantees zero residual vibrations is derived by forcing the real and imaginary parts of the transfer function of the time-delay filter to zero at $s = \sigma \pm j\omega$. For a system with a set of

under-damped poles at $s = \sigma \pm j\omega$, the constraint equations are:

$$\sum_{i=0}^{N} A_i \exp(-\sigma T_i) \cos(\omega T_i) = 0 \tag{4.17}$$

$$\sum_{i=0}^{N} A_i \exp(-\sigma T_i) \sin(\omega T_i) = 0 \tag{4.18}$$

Note that this is equivalent to the conditions given in Eq.3.26 and Eq.3.27. To satisfy the boundary conditions for the rigid body, the transfer function of the time-delay filter should have two zeros at the origin of the complex plane to cancel the rigid body poles, resulting in the constraint equations:

$$\sum_{i=0}^{N} A_i = 0 \tag{4.19}$$

$$\sum_{i=0}^{N} A_i T_i = 0 \tag{4.20}$$

Finally, to desensitize the control profile to uncertainties in the location of the under-damped poles of the system, constraints are derived which place multiple zeros of the time-delay filter at the estimated location of the poles of the system. These constraints are:

$$\sum_{i=0}^{N} A_i T_i \exp(-\sigma T_i) \cos(\omega T_i) = 0 \tag{4.21}$$

$$\sum_{i=0}^{N} A_i T_i \exp(-\sigma T_i) \sin(\omega T_i) = 0 \tag{4.22}$$

which are equivalent to the zero derivative constraint given in Eq.4.1. Since the constraints are nonlinear, there are potentially numerous parameter sets which satisfy all of the constraints. The sufficient conditions for the optimality of the control profile are dependent on the cost function to be optimized.

Unfortunately, the time-optimal on/off controllers are not efficient as they use a lot of actuator effort (fuel). This fact interested several research groups to look for ways to make these controllers more fuel efficient. Some of the methods start essentially with a fuel-efficient command profile and solve for the times at which it should switch on and off [130]. Other methods use a weighting function between move speed and fuel usage [131, 132] or simply allow the command designer to specify the amount of fuel that is to be used for any particular move [133]. All of these methods can be formulated by simply changing the impulses magnitudes in the input shaper. For example,

Fig.4.11 (b) shows how an input shaper with amplitudes of 1 can generate a periods that leads to a much more fuel-efficient command profile. Although this fuel efficient method moves systems in a fuel-efficient manner; however, the system could be damaged during the motion by large internal deflection forces because its transient deflection is not directly controlled. Therefore, researchers have modified the command-shaping process by adding additional constraints to limit transient deflection during the motion [134].

The methods discussed so far in this section require a numerical optimization to solve and this can lead to large computational burdens that hinder real-time implementation. To mitigate this problem, researchers have developed methods which can produce on/off commands that are known in closed form. The designer only has to enter the desired information into given equations and the switch times are immediately known. [125–127] show other techniques to generate time-optimal profiles, where work in [128] demonstrates a general technique of the necessary and sufficient conditions of optimality of the fuel/time optimal control profile generation.

4.7 Conclusions

This chapter discussed the robustification of different SISO input shapers. In summary, the zero derivative constraint flattens the sensitivity curve at the modeled frequency and increases the insensitivity. To further increase insensitivity, this process can be repeated by taking additional higher-order derivatives. However, the price of each additional derivative is an increase in the shaper duration. Note that the duration of TIS ZVD shaper is twice that of the TIS ZV shaper. The EI shaper has the same impulse times as the TIS ZVD shaper but has different amplitude values that lead to greater robustness. The two-hump EI shaper has the same duration as the TIS ZVDD, and the three-hump EI and TIS ZVDDD have the same durations [103,108].

Fig.4.12 shows a sensitivity comparison of different shapers. EI shapers are the most efficient when it comes to robustness against modeling errors and parameter uncertainty as it leads to greater frequency insensitivity levels. However, if the natural frequency of the system is close to the modeling frequency or the actual modal frequency of the system is Gaussian distributed about the modeling frequency, TIS ZVD achieves close to 0% residual vibrations while the EI stays at close to 5% residual vibrations levels. This level although acceptable but it shortens the life time of the system.

SI shapers prove advantageous over the ZVD and EI, because it can be designed to suppress any desired range of frequencies. This flexibility in the design of the robust SI shapers is shown in Fig.4.13(a), where the sensitivity

curves for $I_\omega = 0.5$ and $I_\omega = 0.7$ are compared to that of the ZVD shaper.

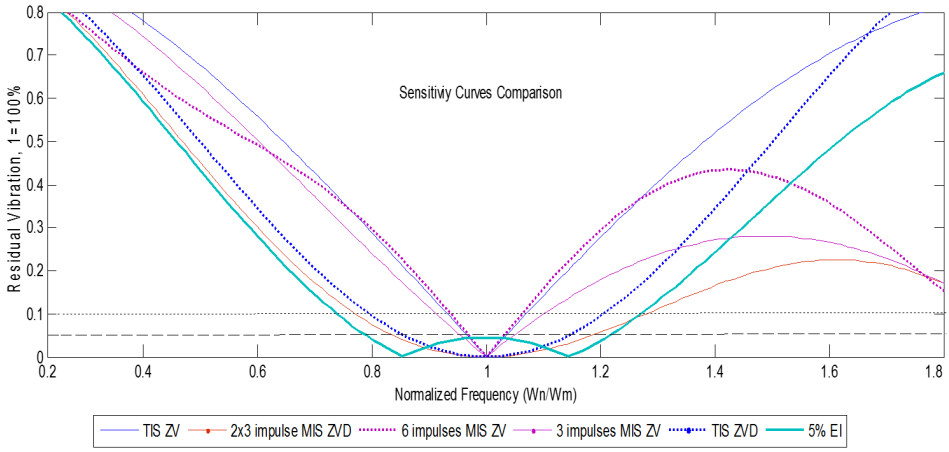

Figure 4.12: TIS, MIS, EI sensitivity curves comparison - Simulation.

MIS shaper has a shorter length than that of a corresponding TIS shaper. However, both shapers have the same ability of vibrations suppression. Also MIS scheme is easier than the traditional scheme because the numerical optimization is unnecessary in the design of the MIS shaper.
Given the different options of input shapers which we discussed in this chapter to choose from, a good approach is to analyze the properties of the different shapers and then choose the shaper that best fits the application in question. These properties are the duration, robustness, ease of implementation, etc.

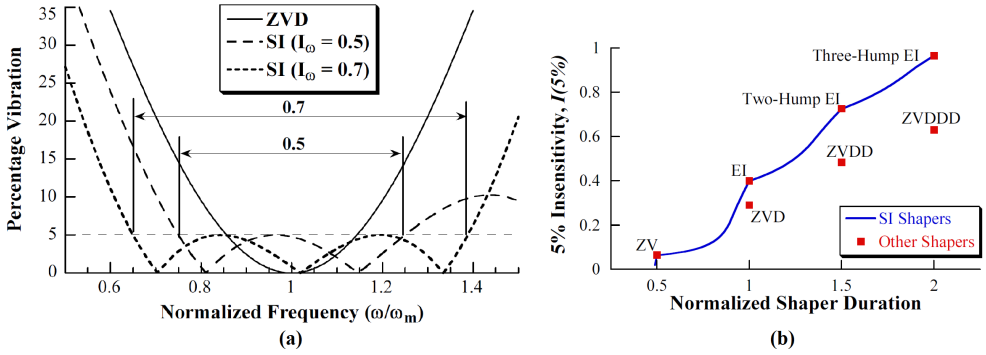

Figure 4.13: (a) Specified insensitivity shapers flexibility (b) Input shaper robustness vs. shaper duration.

Fig.4.13(b) shows the relationship between robustness and duration for several input shapers. The SI shaper is plotted as a line because it can have any desired level of Insensitivity. The SI shaper has the minimum duration

for any given Insensitivity. Therefore, SI shapers will provide the fastest rise time. One point of interest is that the EI shapers correspond to nodes on the SI shaper curve. This indicates that they offer the optimal insensitivity for their duration. It is also of interest to note that the zero-derivative method produces input shapers that provide substantially less Insensitivity than SI shapers. At the end, it is worth mentioning that understanding the robustness of SISO input shapers contributes greatly to understanding their counterparts for MIMO systems.

Chapter 5

Towards multivariable control of vibrations by extending the input shaping approach

In this chapter, we demonstrate the development of a new feedforward control scheme for multiple-input multiple-output systems with multiple-modes of vibrations based on the well-known zero-placement input shaping technique. For that, we review at the beginning of the chapter the work that had been done for multiple-input single-output (MISO) systems. Then we discuss more robust versions of this MISO input shaping technique. Finally, we show our approach in extending this existing input shaping technique to multiple-input multiple-output (MIMO) systems. The newly suggested technique streamlines the design process, minimize shaped command delay and damp all modes of vibrations for all system outputs in direct and cross couplings.

Contents

5.1 Introduction

Input shaping has been given a great deal of consideration for single input systems with multiple-mode of vibrations in time and frequency domains [91, 98, 111–114]. The newly formed (shaped) commands in such schemes are typically made by connecting single-mode impulse sequences in series. Singer [113] demonstrated that shorter-length sequences normally would minimize distortion in the original command while removing all unwanted vibrations. Hyde [112] extended Singers approach by using nonlinear, numerical search algorithms to build time-optimal impulse sequences. As an alternative way, Smith showed that Posicast inputs for multiple-mode systems could be built by placing zeros over all unwanted system poles in the z-plane. Smith in [88] suggested that the discrete transfer function resulting from the specified zeros could then be used to build a Posicast command to remove multiple-mode vibrations.

Tuttle and Seering [98] moved forward with what Smith suggestion and proposed practical zero-placement technique to design optimal input shapers for systems with arbitrary number of modes in the z-plane. In their technique, Tuttle and Seering made all guidelines for effective strategy and simple shaper design to suppress vibrations to become apparent. While most of real systems are multiple-input systems, all previously mentioned efforts had been focusing on the development of shapers for single-input systems. One approach to deal with multiple-input systems is to design all shapers to be identical such that each shaper cancels all system modes of vibrations. However, for large complex flexible structures, there are many flexible modes that need to be suppressed, which may lead to long delay in shaping sequences. For such systems with multiple-input and multiple-mode of vibrations, Pao [116] developed input shaping design technique using pole placement in s-plane which leads to a fewer number of impulses and therefore shorter shaping delay and faster maneuvering. In her approach, more information about the system model is taken into account and input shaping sequences for all system inputs are solved for simultaneously, than solving them for each input independently of each other. However, the technique was only valuable for systems with single-output, though the input was multiple (Fig.5.1(a)).

In this chapter we extend and generalize Pao's technique so it can be applied to damp the vibrations on multiple-input multiple-output systems (Fig.5.1(b)). We do this by segregating the system into different subsystems each with single output only [117]. For the rest of this chapter, in

Section.5.2 we remind and discuss input shaping design for systems with multiple-input single-output (MISO). Then we present improved versions of this design technique in Section.5.3 and Section.5.4. Extending the orginal approach so it can be applied on MIMO systems is explained in Section.5.5. Finally, we discuss how to improve the robustness of this newly developed MIMO scheme in Section.5.6.

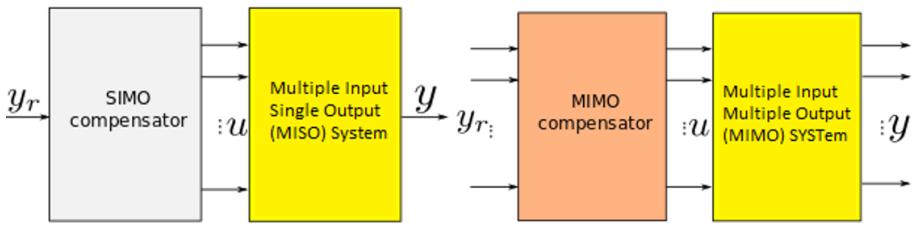

Figure 5.1: Feedforward control of badly damped vibrations. (a) control of MISO (multiple-input single-output) systems [116]. (b) generalized control for MIMO (multiple-input multiple-output) systems.

5.2 Preliminaries on multiple-input shaping design for vibration reduction

Flexible systems are often required to perform fast and precise motion. However, it is well known that fast maneuvers tend to excite the flexible dynamics in those systems, and this can result in residual vibrations that negatively affect the overall performance. Induced vibrations can be suppressed using an input shaping technique that modifies the input commands to reduce the extent to which the system dynamics are excited. All input shaping techniques that have been presented in the previous chapter have been primarily limited to single-input single-output systems. However, many real flexible systems, such as robots and space systems, have multiple actuators that contribute to only one output, Fig.5.2.

In this section we shed the light on input shaper's design approach for flexible structures with multiple-input and single-output. Input shapers for multiple-input systems with multiple-mode of vibrations can be designed to be identical to each other by solving shaper constraint equations for only one sequence of impulses and apply it to all inputs. For large complex flexible structures, there are usually many flexible modes that need to be modeled, which may lead to relatively long time lags in the shaping sequence we apply to each of the inputs! That is, it has been assumed in this approach that each input by itself must cancel out any vibrations that it causes by the end

of its input command.

What was overlooked in this approach is the fact that the different inputs can work together to cancel out vibrations caused by any input command. Thus including more information about the flexible system model into the problem formulation and solving for the impulse sequences simultaneously generally lead to shorter sequences (fewer impulses per input) and yields faster output responses [116]. Inspired by the work in [98] by Tuttle and

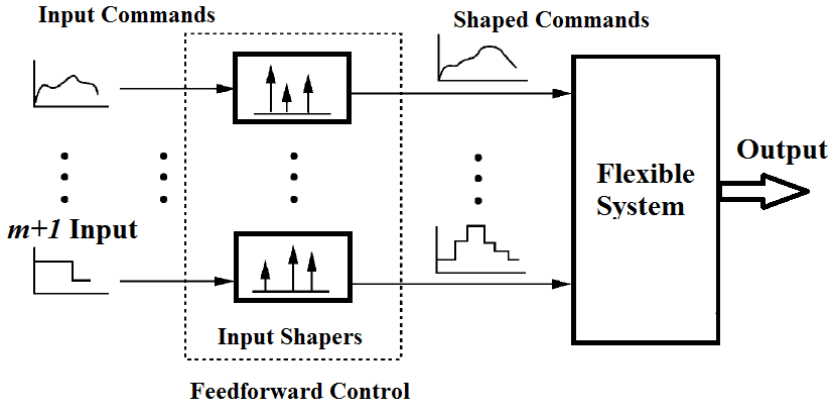

Figure 5.2: Multiple actuators flexible system [116].

Seering, Pao in [116] extended their zero placement technique so it can be applied for multiple-input systems. Let us assume a flexible structure with ***m+1*** input, single output, and ***n*** structural frequencies $w\mathbf{1}...w\mathbf{n}$.

$$\begin{cases} \dot{X}(t) = AX(t) + Bu(t) \\ y(t) = Cx(t) \end{cases} \tag{5.1}$$

where $A = blockdiag[A_i] = blockdiag[\begin{matrix} 0 & 1 \\ -w_i^2 & -2\zeta w_i \end{matrix}]$ and

$$B = blockcol[B_i] = blockcol[\begin{matrix} 0 & 0\ldots & 0 \\ b_0^i & b_1^i\ldots & b_m^i \end{matrix}] \tag{5.2}$$

$\zeta_0 = w_0 = 0$ for the rigid body, and $i = 0, 1, 2, \ldots, n$

The control vector is $u = [u_0 \quad u_1 \ldots \quad u_m]^T$, and the state vector is $X = [x_1 \quad x_2 \quad x_3^1 \quad x_4^1 \ldots x_3^n \quad x_4^n]^T$ where x_1 and x_2 are the rigid body position and velocity, and x_3^i and x_4^i are the modal positions and velocities.

For rest-to-rest control of the flexible structure of Eq.5.1, the objective is to determine the control functions $u(t)$ that satisfies actuator limits, so that

the motion of the system is transferred from an initial rest state $X(0) = [x_{10} \quad 0 \quad 0 \quad 0 \ldots \quad 0 \quad 0]^T$ to a final rest state $X(t_f) = [x_{1f} \quad 0 \quad 0 \ldots \quad 0 \quad 0]^T$ with zero vibrations.

The problem of coupling among inputs is addressed by including information from the B matrix of the system model in Eq.5.1 into the derivation of the designed shapers.

The transfer matrix from the unshaped inputs to the system states is: $(sI - A)^{-1}BQ(s)$, where the multiple-input shaper transfer functions are: $Q_r(s)$,$r = 0, 1, 2, \ldots, m$ and $Q(s)$ is a vector containing them $Q(s) = [Q_1(s) \quad Q_2(s) \quad Q_3(s) \quad \ldots Q_m(s)]^T$.
Applying a set of inputs $U(s)$ to $(sI - A)^{-1}BQ(s)$ yields:

$$(sI - A)^{-1}BQ(s)U(s) = \begin{bmatrix} \frac{b_0^0 Q_0(s)U_0(s)+b_1^0 Q_1(s)U_1(s)+\ldots+b_m^0 Q_m(s)U_m(s)}{s^2} \\ \frac{b_0^0 sQ_0(s)U_0(s)+b_1^0 sQ_1(s)U_1(s)+\ldots+b_m^0 sQ_m(s)U_m(s)}{s^2} \\ \frac{b_0^1 Q_0(s)U_0(s)+b_1^1 Q_1(s)U_1(s)+\ldots+b_m^1 Q_m(s)U_m(s)}{s^2+2\zeta_1\omega_1+\omega_1^2} \\ \frac{b_0^1 sQ_0(s)U_0(s)+b_1^1 sQ_1(s)U_1(s)+\ldots+b_m^1 sQ_m(s)U_m(s)}{s^2+2\zeta_1\omega_1+\omega_1^2} \\ \vdots \\ \frac{b_0^n Q_0(s)U_0(s)+b_1^n Q_1(s)U_1(s)+\ldots+b_m^n Q_m(s)U_m(s)}{s^2+2\zeta_n\omega_n+\omega_n^2} \\ \frac{b_0^n sQ_0(s)U_0(s)+b_1^n sQ_1(s)U_1(s)+\ldots+b_m^n sQ_m(s)U_m(s)}{s^2+2\zeta_n\omega_n+\omega_n^2} \end{bmatrix} \tag{5.3}$$

If all the inputs are the same, then we can factor them out to obtain:

$$(sI - A)^{-1}BQ(s)U(s) = \begin{bmatrix} \frac{(b_0^0 Q_0(s)+b_1^0 Q_1(s)+\ldots+b_m^0 Q_m(s))U(s)}{s^2} \\ \frac{(b_0^0 sQ_0(s)+b_1^0 sQ_1(s)+\ldots+b_m^0 sQ_m(s))U(s)}{s^2} \\ \frac{(b_0^1 Q_0(s)+b_1^1 Q_1(s)+\ldots+b_m^1 Q_m(s))U(s)}{s^2+2\zeta_1\omega_1+\omega_1^2} \\ \frac{(b_0^1 sQ_0(s)+b_1^1 sQ_1(s)+\ldots+b_m^1 sQ_m(s))U(s)}{s^2+2\zeta_1\omega_1+\omega_1^2} \\ \vdots \\ \frac{(b_0^n Q_0(s)+b_1^n Q_1(s)+\ldots+b_m^n Q_m(s)U)(s)}{s^2+2\zeta_n\omega_n+\omega_n^2} \\ \frac{(b_0^n sQ_0(s)+b_1^n sQ_1(s)+\ldots+b_m^n sQ_m(s))U(s)}{s^2+2\zeta_n\omega_n+\omega_n^2} \end{bmatrix} \tag{5.4}$$

To filter out any vibrations due to the flexible mode, we choose $Q_r(s)$ such that:

$$b_0^i Q_0(s) + b_1^i Q_1(s) + \ldots + b_m^i Q_m(s)|_{s=-\zeta_i\omega_i \mp j\omega_{d,i}} = 0 \tag{5.5}$$

If we would like not to take the information in the input matrix B into account and would like to design shapers independently of each other, the each $Q_r(s)$ would need zeros at all the poles of the flexible system. However, using the information in the B matrix gives us the constraints in Eq.5.5, and simpler input shapers can be developed than those having zeros at all flexible

system poles. The desired impulse sequences (shapers) can then be solved for by taking the inverse Laplace transforms of $Q_r(s)$. If we assume that all designed shapers have the same impulse spacing time T, then $Q_r(s)$ (the r^{th} input shaper) can be written in the following form:

$$Q_r(s) = a_{0r} + a_{1r}e^{-sT} + \ldots + a_{lr}e^{-slT} \tag{5.6}$$

where $l = [\frac{2n}{m+1}]$ is the number of zeros that each of the shapers has, and a_{lr} is the l^{th} impulse amplitude of the r^{th} input shaper. By substituting Eq.5.6 in Eq.5.5, the constraint equation can be re-written in the following form:

$$\begin{aligned} b_0^i(a_{00} + a_{10}e^{-sT} + \ldots + a_{l0}e^{-slT}) + b_1^i(a_{01} + a_{11}e^{-sT} + \ldots + a_{l1}e^{-slT}) + \ldots \\ + b_m^i(a_{0m} + a_{1m}e^{-sT} + \ldots + a_{lm}e^{-slT})|_{s=-\zeta_i w_i \mp j w_{d,i}} = 0 \end{aligned} \tag{5.7}$$

and all constraint equations can be grouped in the following matrix form:

$$Pa = W \tag{5.8}$$

where a is the vector that contains all shapers' impulse amplitudes:

$$a = [a_{00} \quad a_{10} \ldots \quad a_{l0} \quad a_{01} \quad a_{11} \ldots \quad a_{l1} \ldots \quad a_{0m} \quad a_{1m} \ldots \quad a_{lm}]^T \tag{5.9}$$

$W = [\begin{smallmatrix} 0_{2n\times 1} \\ 1_{(m+1)\times 1} \end{smallmatrix}]$, there are $2n + (m + 1)$ equations and $(l + 1)(m + 1)$ unknowns, and the P matrix is:

$$P = \begin{bmatrix} b_0^1 & b_0^1 e^{-s_1 T} \ldots & b_0^1 e^{-s_1 lT} & b_1^1 & b_1^1 e^{-s_1 T} \ldots & b_1^1 e^{-s_1 lT} & \ldots \\ b_0^1 & b_0^1 e^{-s_1^* T} \ldots & b_0^1 e^{-s_1^* lT} & b_1^1 & b_1^1 e^{-s_1^* T} \ldots & b_1^1 e^{-s_1^* lT} & \ldots \\ \ldots & \ldots & \ldots & \ldots & \ldots & \ldots & \\ b_0^n & b_0^n e^{-s_n T} \ldots & b_0^n e^{-s_n lT} & b_1^n & b_1^n e^{-s_n T} \ldots & b_1^n e^{-s_n lT} & \ldots \\ b_0^n & b_0^n e^{-s_n^* T} \ldots & b_0^n e^{-s_n^* lT} & b_1^n & b_1^n e^{-s_n^* T} \ldots & b_1^n e^{-s_n^* lT} & \ldots \\ 1 & 1 \ldots & 1 & 0 & 0 \ldots & 0 & \ldots \\ \ldots & \ldots & \ldots & \ldots & \ldots & \ldots & \\ 0 & 0 \ldots & 0 & 0 & 0 \ldots & 0 & \ldots \end{bmatrix}$$

$$\begin{bmatrix} \ldots & b_m^1 & b_m^1 e^{-s_1 T} \ldots & b_m^1 e^{-s_1 lT} \\ \ldots & b_m^1 & b_m^1 e^{-s_1^* T} \ldots & b_m^1 e^{-s_1^* lT} \\ & \ldots & \ldots & \\ \ldots & b_m^n & b_m^n e^{-s_n T} \ldots & b_m^n e^{-s_n lT} \\ \ldots & b_m^n & b_m^n e^{-s_n^* T} \ldots & b_m^n e^{-s_n^* lT} \\ \ldots & 0 & 0 \ldots & 0 \\ & \ldots & \ldots & \\ \ldots & 1 & 1 \ldots & 1 \end{bmatrix} \tag{5.10}$$

For $l = \frac{2n}{m+1}$ there will be an equal number of equations and unknowns and a can be solved using a generalized inverse:

$$a = P^{\intercal}W \tag{5.11}$$

This solution yields shapers at each of the inputs with the same number of impulses l. Zeros "0" in the P matrix correspond to the constraint equations shown in Eq.5.5, where Ones "1" correspond to the unity constraint which ensures that the final value of the shaped command will be similar to the unshaped one. It is also possible to design these shapers to have different numbers of impulses. The solution of Eq.5.11 gives the values of the impulses amplitudes of each shaper, which can be plotted as a funtion of T in order to select a range of shaper solutions that satisfy a specific design requirements. Fig.5.3 shows an example of impulses amplitudes versus T plot for three inputs system and when the input shapers are designed to have four impulses each. In this plot, selecting the smallest T that satisfies that all impulses are positive for all shapers corresponds to the shortest command delay and the fastest responses possible.

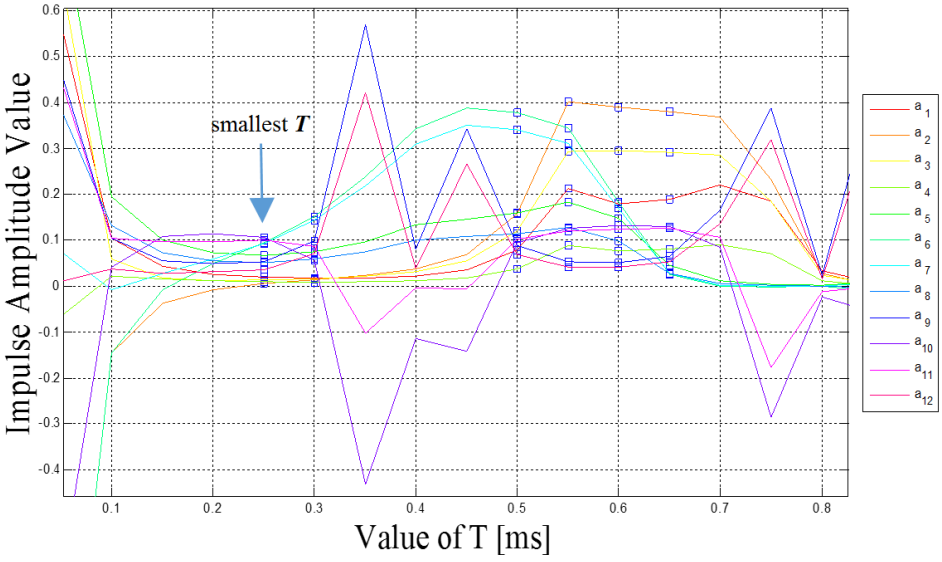

Figure 5.3: Shapers impulse amplitudes versus T for a system with three inputs and four impulses per shaper.

As shown in this section, input shapers for multiple-input single-out systems and with multiple-mode of vibrations can be designed to have fewer impulses per input, by incorporating more system model information into the solution formulation. This leads to shorter shaper lengths, thus faster output responses, compared to the traditional way where all shapers are identical to each other for all inputs [116]. It should be noted though that

this approach assumes that the impulses are spaced evenly in time for each shaper and that impulses across shapers are synchronous. It focuses also primarily on equal numbers of impulses per shaper.

Extending this procedure such that these assumptions are detached will likely lead to an even further increase in the time savings of the multiple-input shaping approach over single-input shaping designs. The following two sections, Section.5.3 and Section.5.4, discuss relaxing some of the constraints to shorten the MISO shaper length.

5.3 The modified multiple-input shaping design for vibrations reduction

This section discusses a modified version of the MISO technique discussed in Section.5.2. The new modified technique aims at shortening the shaper length to provide faster responses. The original MISO technique derived in Section.5.2 requires to meet zero placement constraints and amplitude constraints at the same time. This allows to find the particular solution in the all-positive orthant that meets the summation constraints on the impulse amplitudes. Removing this summation constraint allows to find the shortest shaper that is in the all-positive orthant, hence leading to faster maneuvers. However doing so changes two properties:
(1) the final setpoint of the shaped response is no longer the same as the final setpoint of the unshaped response, and
(2) it is no longer true that the shaped input causes saturation if and only if the unshaped input causes saturation.

The first item can be fixed by scaling all the shapers by the same amount so that the final setpoint is indeed the same and that our shapers remain a solution of Eq.5.13. Further by knowing the sum of the amplitudes of a shaper, new bounds can be determined for the unshaped input to prevent actuator saturation [119]. If we drop the constraints that the summation of the impulse amplitudes for each input shaper to be one, we end up with a new set of equations and a new modified P matrix which is denoted here as P_{mod} :

$$P_{\text{mod}}\, a = 0_{2n\times 1} \tag{5.12}$$

where

$$a = [a_{00} \quad a_{10}\ldots \quad a_{l0} \quad a_{01} \quad a_{11}\ldots \quad a_{l1}\ldots \quad a_{0m} \quad a_{1m}\ldots \quad a_{lm}]^T$$

and

$$P_{\text{mod}} = \begin{bmatrix} b_0^1 & b_0^1 e^{-s_1 T} \dots b_0^1 e^{-s_1 lT} & b_1^1 & b_1^1 e^{-s_1 T} \dots \\ b_0^1 & b_0^1 e^{-s_1^* T} \dots b_0^1 e^{-s_1^* lT} & b_1^1 & b_1^1 e^{-s_1^* T} \dots \\ \dots & \dots \quad \dots \quad \dots & \dots & \dots \\ \dots & \dots \quad \dots \quad \dots & \dots & \dots \\ b_0^n & b_0^n e^{-s_n T} \dots b_0^n e^{-s_n lT} & b_1^n & b_1^n e^{-s_n T} \dots \\ b_0^n & b_0^n e^{-s_n^* T} \dots b_0^n e^{-s_n^* lT} & b_1^n & b_1^n e^{-s_n^* T} \dots \end{bmatrix}$$

$$\begin{bmatrix} \dots b_1^1 e^{-s_1 lT} \dots b_m^1 & b_m^1 e^{-s_1 T} \dots b_m^1 e^{-s_1 lT} \\ \dots b_1^1 e^{-s_1^* lT} \dots b_m^1 & b_m^1 e^{-s_1^* T} \dots b_m^1 e^{-s_1^* lT} \\ \dots \quad \dots & \dots \quad \dots \\ \dots \quad \dots & \dots \quad \dots \\ \dots b_1^n e^{-s_n lT} \dots b_m^n & b_m^n e^{-s_n T} \dots b_m^n e^{-s_n lT} \\ \dots b_1^n e^{-s_n^* lT} \dots b_m^n & b_m^n e^{-s_n^* T} \dots b_m^n e^{-s_n^* lT} \end{bmatrix} \tag{5.13}$$

As mentioned previously, n is the number of flexible modes, $m+1$ is the number of inputs, and l is the number of zeros of each shaper.

The system flexible-mode positions and velocities become zeros after the system settles to its final value. The only difference between the final and the initial states will be in the rigid body mode. Therefore, we will use the rigid body mode to determine the scaling factor K, which is the scalar that we can use to scale all new input shapers.

$$K = \frac{x_{rigid}}{x_{rigid_{NEW}}} \tag{5.14}$$

The way in which k can be derived is explained in details in [119]. The rigid body position x_{rigid} is a double integrator of the inputs:

$$x_{rigid} = \int_{t_0}^{t_f} \int_{0}^{T} B_0 U(\tau) d\tau dT \tag{5.15}$$

where t_f is some time after which the input has returned to zero, and B_0 is the input matrix for the rigid body which can be expressed as per Eq.5.2 as the following [119]: $B_0 = \begin{bmatrix} 0 & 0 & \dots & 0 \\ b_0^0 & b_1^0 & \dots & b_m^0 \end{bmatrix}$

By applying linearity, we obtain:

$$x_{rigid} = \sum_{i=0}^{m} \left(b_i^0 \int_{t_0}^{t_f} \int_{0}^{T} u_i(\tau) d\tau dT \right) \tag{5.16}$$

If all inputs are equal, then the final response is:

$$x_{rigid} = \left(\sum_{i=0}^{m} b_i^0 \right) \int_{t_0}^{t_f} \int_{0}^{T} u(\tau) d\tau dT \tag{5.17}$$

Similarly, the scaled position $x_{rigid_{NEW}}$ can be as the following:

$$x_{rigid_{NEW}} = \left(\sum_{i=0}^{m} b_i^0 n_i \right) \int_{t_0}^{t_f} \int_{0}^{T} u(\tau) d\tau dT \tag{5.18}$$

where n_i is the scaling factor for each input. By taking the ratio of x_{rigid} to $x_{rigid_{NEW}}$ for equal inputs we obtain the K factor which ensures that the final setpoint of the shaped response is the same as the final setpoint of the unshaped response. In other words scaling the shaped response by K factor sets the ratio of shaped to unshaped setpoints to one:

$$K = \frac{\sum_{i=0}^{m} b_i^0}{\sum_{i=0}^{m} \left(b_i^0 \sum_{k=0}^{l} a_{ki} \right)} \tag{5.19}$$

where a_{ki} is the kth impulse of the shaper at the ith input. If the sum of the impulse amplitudes of each shaper is one, as is the case in Section.5.2, the K will equal to one.

The investigation and development of this method [119] has shown that it always leads to shorter shaper length than the original method presented in Section.5.2, thus significant time saving over the original method and hence faster maneuvers. Moreover, the P_{mod} matrix is smaller in size than the original P matrix, and this leads to faster numerical solutions as well. Nevertheless, both techniques are limited by the requirement of having the unshaped inputs known and scaled version of one another. Section.5.4 discuses an extension of this section's design approach for MISO systems to overcome these limitations and to improve the shaper robustness with respect to either the system parameters (ω_n and ζ_n) or even with respect to one of the input matrix B parameters.

5.4 Cooperative robust multiple-input shaping design for vibrations reduction

In the previous sections of this chapter, inputs were assumed to be a scaled version of one another for analytic or computational simplicity. This section details a modification to the original technique presented in Section.5.2 to overcome this limitation so it can be used with arbitrary inputs (but known), or when inputs are unknown but can only come from some small set. When inputs are unknown and arbitrary, only single input shaping guarantees zero vibration. The section also discusses ways to improve robustness with respect to the input matrix B and flexible pole positions.
To filter out any vibrations due to flexible modes in this scenario, we choose the Q_r such that $\sum_{r=0}^{m} b_r^i Q_r(s) U_r(s)$ has zeros at $s^2+2\zeta_i\omega_i s+{\omega_i}^2$. Accordingly, the constraints to be satisfied by the shapers are:

$$b_0^i U_0(s_i)(a_{00} + a_{10}e^{-s_iT} + \ldots + a_{l0}e^{-s_ilT}) + b_1^i U_1(s_i)(a_{01} + a_{11}e^{-s_iT} + \ldots + a_{l1}e^{-s_ilT}) + \ldots + b_m^i U_m(s_i)(a_{0m} + a_{1m}e^{-s_iT} + \ldots + a_{lm}e^{-s_ilT}) = 0 \tag{5.20}$$

These constraints along with the unity constraints can be put in the following matrix form $Pa = W$, where

$$P = \begin{bmatrix} b_0^1U_0(s_1) & b_0^1U_0(s_1)e^{-s_1^1T} & \ldots & b_0^1U_0(s_1)e^{-s_1lT} & \ldots \\ b_0^1U_0(s_1^*) & b_0^1U_0(s_1^*)e^{-s_1^*T} & \ldots & b_0^1U_0(s_1^*)e^{-s_1^*lT} & \ldots \\ \vdots & \vdots & \ldots & \vdots & \ldots \\ b_0^nU_0(s_n) & b_0^nU_0(s_n)e^{-s_1T} & \ldots & b_0^nU_0(s_n)e^{-s_nlT} & \ldots \\ b_0^nU_0(s_n^*) & b_0^nU_0(s_n^*)e^{-s_1T} & \ldots & b_0^nU_0(s_n^*)e^{-s_nlT} & \ldots \\ 1 & 1 & 1 & 1 & \ldots \\ \vdots & \vdots & \vdots & \vdots & \ldots \\ 0 & 0 & 0 & 0 & \ldots \end{bmatrix}$$

$$\begin{bmatrix} \ldots & b_m^1U_m(s_1) & b_m^1U_m(s_1)e^{-s_1T} & \ldots & b_m^1U_m(s_1)e^{-s_1lT} \\ \ldots & b_m^1U_m(s_1^*) & b_m^1U_m(s_1^*)e^{-s_1^*T} & \ldots & b_m^1U_m(s_1^*)e^{-s_1^*lT} \\ \ldots & \vdots & \vdots & \ldots & \vdots \\ \ldots & b_m^nU_m(s_n) & b_m^nU_m(s_n)e^{-s_nT} & \ldots & b_m^nU_m(s_n)e^{-s_nlT} \\ \ldots & b_m^nU_m(s_n^*) & b_m^nU_m(s_n^*)e^{-s_n^*T} & \ldots & b_m^nU_m(s_n^*)e^{-s_n^*lT} \\ \ldots & 0 & 0 & 0 & 0 \\ \ldots & \vdots & \vdots & \vdots & \vdots \\ \ldots & 1 & 1 & 1 & 1 \end{bmatrix} \tag{5.21}$$

where $i = 1, 2, ..., n$ and s_i represents the system pole locations. The rest of this approach is exactly the same as the original one in solving for the vector a and selecting T to be the smallest to have all members of a positive. This cooperative method as we have seen relies on the system poles and the B matrix which are most of the time imperfect. Hence the need to have additional constraints to improve the robustness of the shapers. An easy way to do so is to take the derivative of residual vibrations with respect either a given pole or even with respect to one member of the matrix B [97]. If we apply it to an element b_r^i of B, then the resultant constraint equation is:

$$[\ 0\ \ 0 \ldots 0\ \ \ldots\ \ U_r(s_i)\ \ U_r(s_i)e^{-s_iT} \ldots U_r(s_i)e^{-s_ilT}\ \ \ldots\ \ 0\ \ 0 \ldots 0\ ]\ a\ =\ 0 \tag{5.22}$$

This new constraint equation forces the r-th input shaper to have a zero at the i-th mode. In other words, the vibration of the i-th mode (structural frequency) is independent of the uncertainty in the parameter b_r^i. This robustness for sure adds delay to the shaper, and each additional constraint equation adds one impulse to each shaper as per the following expression:

$$l = [\frac{2(n+R)}{m+1}] \tag{5.23}$$

where R is the number of parameters for which robustness constraints have been added. Similar procedure can be used to add one degree of robustness with respect to the uncertainties in pole locations. For such robustness, the derivative of residual vibrations with respect to a particular pole location is required to be zero:

$$\frac{d}{ds_i}(P_{2i}a) = \frac{dP_{2i}}{ds_i}a = 0 \tag{5.24}$$

where P_{2i} is the $2i$-th row of the matrix P. The vector $\frac{dP_{2i}}{ds_i}$ has the structure:

$$\frac{dP_{2i}}{ds_i} = \Big[\, b_0^i U_0^{'}(s_i)\ \ b_0^i(U_0^{'}(s_i) - TU_0(s_i))e^{-s_iT}\ \ \ldots\ \ b_0^i(U_0^{'}(s_i) - lTU_0(s_i))e^{-s_ilT}\ \ \ldots$$
$$\ldots\ \ b_m^i U_m^{'}(s_i)\ \ b_m^i(U_m^{'}(s_i) - TU_m(s_i))e^{-s_iT}\ \ \ldots\ \ b_m^i(U_m^{'}(s_i) - lTU_m(s_i))e^{-s_ilT}\,\Big] \tag{5.25}$$

This constraint implies that $\frac{dP_{2i}}{d\omega_{ni}}$ and $\frac{dP_{2i}}{d\zeta_{ni}}$ are also equal to zero.

For arbitrary and unknown inputs, only single-input shaping guarantees zero vibrations. One way to design shapers for such unknown inputs is to generate a discrete sample sequences out of them, observe the inputs at each sample, and then to design shapers using the cooperative technique which we just discussed.

Real-time calculation of new shaper at each period might be computationally very challenging. What make it more challenging is the difficulty to find solutions which satisfy that all impulse amplitudes are positive. One way to reduce the computational complexity is to assume that impulse spacing T has been chosen such that all inputs are just weighted versions of the unit-sample function. This approach is well explained in [97].

5.5 The new multiple-input multiple-output input-shaping design for multiple-mode vibrations reduction

Using multiple-axis actuators in miniaturized systems has many great advantages over using their counterparts mono-axis actuators. These advantages can be summarized in saving space by reducing the number of required actuators, saving energy consumption, providing modularity and freedom for designers to use them for different applications. Piezoelectric materials are used extensively in building such multiple-axis actuators due to their high accuracy and dynamics, high bandwidth and energy efficiency. Piezoelectric actuators have been used widely in several engineering applications. Most of the commercial microscopes use piezoelectric actuators, in particular piezoelectric tubes, to produce topographical images.

For example, in Atomic Force Microscopes (AFMs), samples to be scanned are placed on top of a piezoelectric tube which tracks a triangular waveform along the x-axis and slowly increasing ramp along the y-axis. This x-y motion causes a cantilever with sharp probe in contact with the sample surface to deflect due to variations in its topography. The cantilever deflection is captured by Photo Sensitive Diode (PSD) which captures a deflection of a laser beam focused on the probe end of the cantilever. These deflections vary the intensity of light captured by the PSD, which in turn, is used to produce the topographical image, as shown in Fig.5.4.

On the contrary, piezoelectric cantilevers are used broadly in micromanipulators to perform microhandling or microassembly operations. The microgripper shown in Fig.5.5 is one example of such systems. It is a two-fingered microgripper in which each finger is a 2-DOF piezocantilever that is able to move independently in the two orthogonal directions, thus yielding 4-DOF. Additionally, the vast developments and the need for more dexterity in some industrial applications like rapid manufacturing motivated the need to increase the number of actuator's degrees of freedom to achieve complex manipulations.

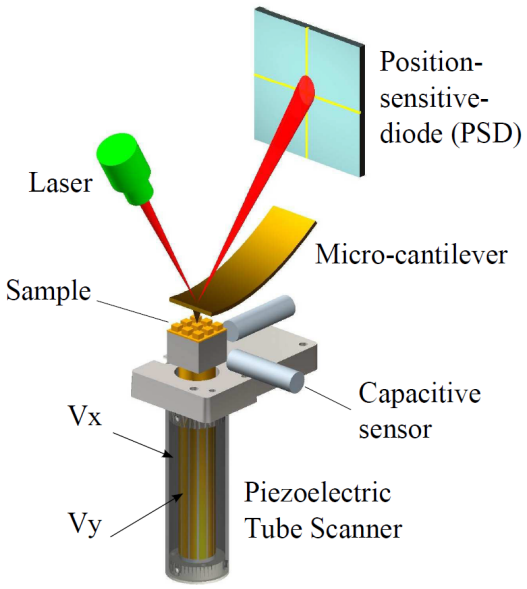

Figure 5.4: Schematic of an AFM [44].

The 5-DOF 3D monolithic structures shown in Fig.5.6-a is a good example of these systems that offer a new perspective to design innovative micro/nano positioners. It is equipped with six piezostack actuators and able to perform high resolution x-y-z linear motions and angular motions about x and about y axes as shown in Fig.5.6-b.

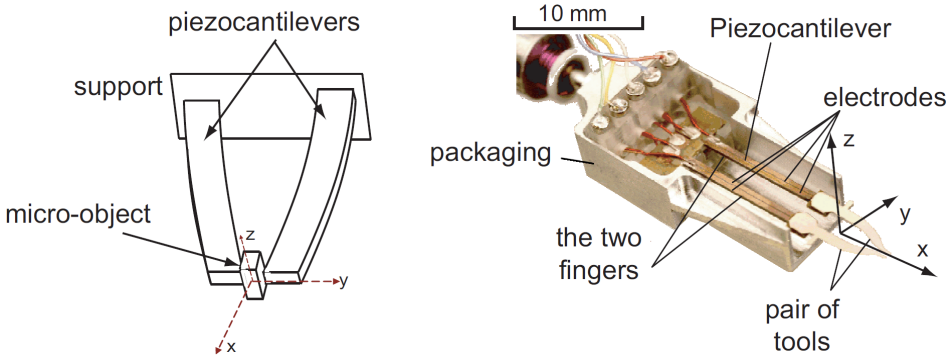

Figure 5.5: The 4-DOF Microgripper with 2-DOF piezocantilevers [150].

For all of the piezoelectric actuators like the aforementioned ones, structural induced vibrations as well as other hysteresis and creep nonlinearities compromise actuators performance and dexterity. Moreover, the coupling between different axes makes the control of such actuators a more difficult task to achieve. For instance, the high scanning rate of the piezoelectric tubes in Fig.5.4 excites the resonance and induces mechanical vibrations.

Also, the vibrations induced in the two cantilevers shown in Fig.5.5 dictate the micrograpper performance itself. This also applies to the piezostacks used in Fig.5.6.

A typical standard for controlling piezoelectric actuators has been to design a feedback controller that would suppress these vibrations. A more comprehensive way would be to design a multivariable controller that would suppress vibrations of all the transfer-functions involved, including the cross-coupling transfer functions which are ignored in many research works.

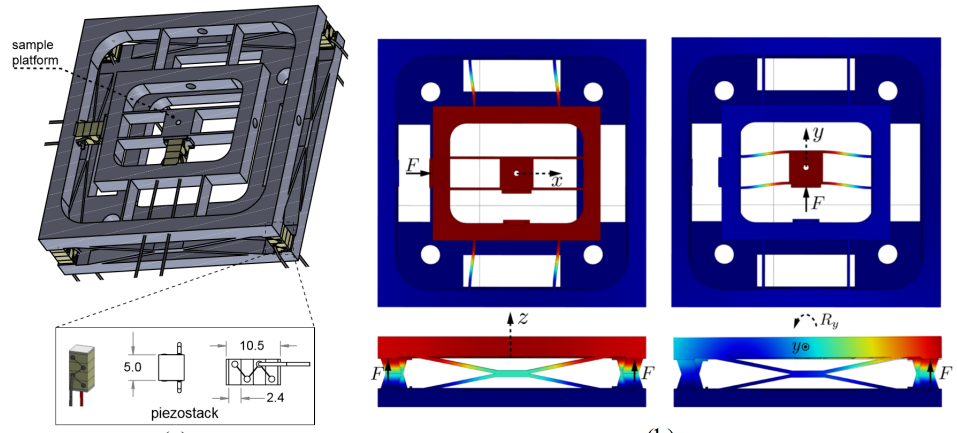

Figure 5.6: (a) 5-DOF piezoelectric positioner CAD model (b) Structure deformations [149].

This section presents a new way for designing a multivariable controller that can be used for the control of piezoelectric tubes. In this section, we explain how the approach we showed in Section.5.2 can be extended and applied to multiple-output systems with multi-mode of vibrations. To be able to do so, we need to look at this multiple-input multiple-output system (MIMO) with K outputs like the one in Fig.5.7(a), as a K number of multiple-input single-output (MISO) sub-systems, each has the same number of inputs as the original system and only one output as shown in Fig.5.7(b). The number of these resulting MISO sub-systems is K equal to the number of the original system's outputs and each has its own shaper solution $Q_j(s)$.
As an example, a system with 3-input 3-output and 3 modes of vibrations is not three SISO systems but rather it is in this approach three multiple-input single-output (MISO) systems, each of the outputs is coupled to all inputs through the B_j matrix. To be able to have one shaper solution for all outputs, we have to include B_j information of all outputs in the shaper design process. That is, the designed shapers should be able to cancel all modes of vibrations for all outputs. The multiple-mode in this context refers to the dominant resonance frequencies for each output of the MIMO system.

This can be achieved by creating a new state vector $X = [X_1\ X_2\ \ldots X_K]^T$ that includes all state vectors $X_j = \begin{bmatrix} x_{j1} & x_{j2} & x_{j3}^1 & x_{j4}^1 \ldots x_{j3}^n & x_{j4}^n \end{bmatrix}^T$, where X_j represents the jth output state vector Fig.5.7(c).

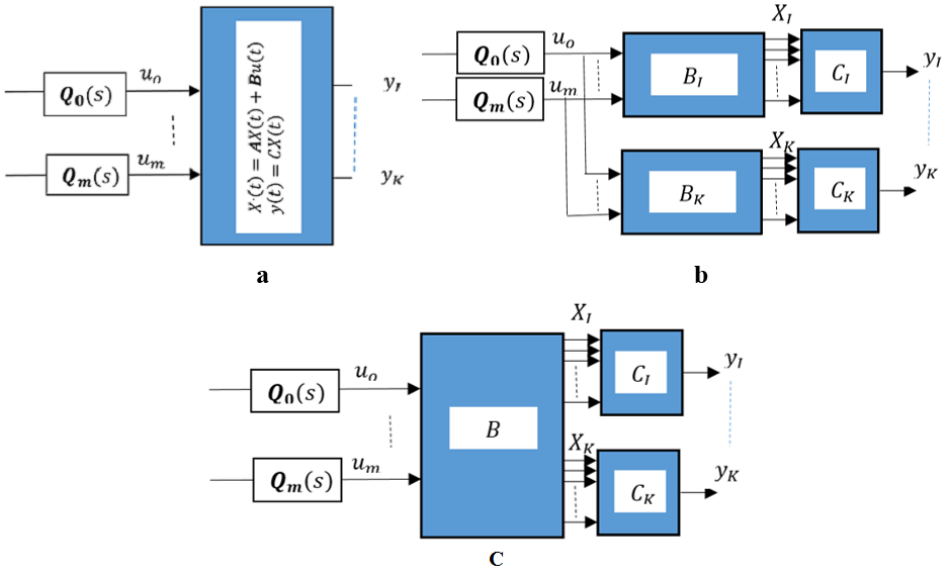

Figure 5.7: Simplifying system derivation

The new input matrix which relates all system inputs to all system states can be expressed as the following:

$$B = blockcol\,[B_j] = blockcol\left[blockcol\begin{bmatrix} 0 & 0 & \cdots & 0 & \cdots & 0 \\ b_{j0}^i & b_{j1}^i & \cdots & b_{jr}^i & \cdots & b_{jm}^i \end{bmatrix}\right] \tag{5.26}$$

$$B = \begin{bmatrix} 0 & b_{10}^0 & \cdots & 0 & b_{10}^n & \cdots & 0 & b_{j0}^0 & \cdots & 0 & b_{j0}^n & \cdots & 0 & b_{K0}^0 & \cdots & 0 & b_{K0}^n \\ 0 & b_{11}^0 & \cdots & 0 & b_{11}^n & \cdots & 0 & b_{j1}^0 & \cdots & 0 & b_{j1}^n & \cdots & 0 & b_{K1}^0 & \cdots & 0 & b_{K1}^n \\ \vdots & \vdots & \cdots & \vdots & \vdots & \cdots & \vdots & \vdots & \cdots & \vdots & \vdots & \cdots & \vdots & \vdots & \cdots & \vdots & \vdots \\ 0 & b_{1r}^0 & \cdots & 0 & b_{1r}^n & \cdots & 0 & b_{jr}^0 & \cdots & 0 & b_{jr}^n & \cdots & 0 & b_{Kr}^0 & \cdots & 0 & b_{Kr}^n \\ \vdots & \vdots & \cdots & \vdots & \vdots & \cdots & \vdots & \vdots & \cdots & \vdots & \vdots & \cdots & \vdots & \vdots & \cdots & \vdots & \vdots \\ 0 & b_{1m}^0 & \cdots & 0 & b_{1m}^n & \cdots & 0 & b_{jm}^0 & \cdots & 0 & b_{jm}^n & \cdots & 0 & b_{Km}^0 & \cdots & 0 & b_{Km}^n \end{bmatrix}^T \tag{5.27}$$

where the number of inputs is $r = 0,\ 1,\ 2, \ldots,\ m$, the number of structural frequencies in each direction (actuator axes) is $i = 0,\ 1,\ 2, \ldots,\ n$ and the number of outputs is $j = 1,\ 2,\ ,\ K$.

As an example, for a system with 2 inputs ($m = 1$) and two outputs ($K = 2$), each with 2 modes of vibrations ($n = 2$), the system input matrix for one of the outputs is:

$$B_j = \begin{bmatrix} 0 & b_{j0}^0 & 0 & b_{j0}^1 & 0 & b_{j0}^2 \\ 0 & b_{j1}^0 & 0 & b_{j1}^1 & 0 & b_{j1}^2 \end{bmatrix}^T \tag{5.28}$$

and the system input matrix for both outputs will be:

$$B = \begin{bmatrix} 0 & b_{10}^0 & 0 & b_{10}^1 & 0 & b_{10}^2 & 0 & b_{20}^0 & 0 & b_{20}^1 & 0 & b_{20}^2 \\ 0 & b_{11}^0 & 0 & b_{11}^1 & 0 & b_{11}^2 & 0 & b_{21}^0 & 0 & b_{21}^1 & 0 & b_{21}^2 \end{bmatrix}^T \tag{5.29}$$

For a system with 3 inputs ($m = 2$) and three outputs ($K = 3$), each with 3 modes of vibrations ($n = 3$), the system input matrix for all outputs is:

$$B = \begin{bmatrix} 0 & b_{10}^0 & 0 & b_{10}^1 & 0 & b_{10}^2 & 0 & b_{20}^0 & 0 & b_{20}^1 & 0 & b_{20}^2 & 0 & b_{30}^0 & 0 & b_{30}^1 & 0 & b_{30}^2 \\ 0 & b_{11}^0 & 0 & b_{11}^1 & 0 & b_{11}^2 & 0 & b_{21}^0 & 0 & b_{21}^1 & 0 & b_{21}^2 & 0 & b_{31}^0 & 0 & b_{31}^1 & 0 & b_{31}^2 \\ 0 & b_{12}^0 & 0 & b_{12}^1 & 0 & b_{12}^2 & 0 & b_{22}^0 & 0 & b_{22}^1 & 0 & b_{22}^2 & 0 & b_{32}^0 & 0 & b_{32}^1 & 0 & b_{32}^2 \end{bmatrix}^T \tag{5.30}$$

The new subsequent constraint matrix is $P = blockcol\,[P_j]$, where P_j is the same matrix shown in Eq.5.10 for each of the outputs, taking into consideration that zero placement and the unity constraints in each P_j should not be repeated more than once in P, since we assumed one shaper solution for all outputs. Including the newly formed input matrix B shown in Eq.5.27 in the problem solving would allow us to design a different shaper for each of the inputs.

The newly formed P matrix shown in Eq.5.31, which can be constructed from B and sub-system poles, would ensure that the designed shapers will suppress all modes of vibrations for all outputs. The shaper amplitudes vector a can be obtained from solving $a = P^{\intercal}W$.

As an example, for 2-input 2-output system similar to the one in Eq.5.29 with 2 modes of vibrations, the P matrix in Eq.5.32 becomes as shown in Eq.5.31. Where $[(w_1, \zeta_1),\ (w_2, \zeta_2)]$ and $[(w_3, \zeta_3),\ (w_4, \zeta_4)]$ to be the structural frequencies and damping ratios for the first and second output

respectively. $s_{1,2} = -\zeta_{1,2} w_{1,2} \mp j w_{d\ 1,2}$ are system poles for the first output and $s_{3,4} = -\zeta_{3,4} w_{3,4} \mp j w_{d\ 3,4}$ are system poles for the second output.

The generic P matrix in Eq.5.31 allows to design a compensator for any MIMO system with multiple-mode of vibrations, which is a major contribution in this thesis work. However, it is very important to mention at this stage that, as the number of inputs, outputs or modes of vibrations increase, the P matrix size becomes larger and solving for shaper impulses becomes more challenging.

The following steps summarize our new design approach for a system with (m) inputs and (K) outputs, each with (n) modes of vibrations:

1. Model the system under test:

   (a) Derive the transfer function that relates all inputs to each of the outputs. The number of these transfer functions is equal to the number of system outputs (K).

   (b) Identify the system poles for each transfer function, which in turn identifies the structural frequencies and damping ratios for each output. The number of poles for each output equals to the number of modes of vibrations (n).

   (c) Derive the input matrix B_j of each of these (K) transfer functions, as per Eq.5.2, after converting them to state space representation.

   (d) Form the whole system input matrix B as per Eq.5.27.

2. Form the whole system P matrix as per Eq.5.31.

3. Solve for the shapers' impulses amplitudes as per the following equation $a = P^{\intercal} W$.

4. Plot impulses amplitudes versus the shaper period T.

5. Select the smallest T that satisfies the positive impulse amplitude constraint.

   Following these steps is easy and straightforward and doesn't require much efforts on the modeling side as information needed to calculate the impulses amplitudes are minimal. In the next chapter we will be using this approach with different steps to verify its effectiveness in suppressing vibrations.

$$P=\begin{bmatrix}
b_{10}^1 & b_{10}^1 e^{-s_1 T} & \dots & b_{10}^1 e^{-s_1 lT} & b_{11}^1 & b_{11}^1 e^{-s_1 T} & \dots & b_{11}^1 e^{-s_1 lT} & \dots & b_{1m}^1 & b_{1m}^1 e^{-s_1 T} & \dots & b_{1m}^1 e^{-s_1 lT} \\
b_{10}^1 & b_{10}^1 e^{-s_1^* T} & \dots & b_{10}^1 e^{-s_1^* lT} & b_{11}^1 & b_{11}^1 e^{-s_1^* T} & \dots & b_{11}^1 e^{-s_1^* lT} & \dots & b_{1m}^1 & b_{1m}^1 e^{-s_1^* T} & \dots & b_{1m}^1 e^{-s_1^* lT} \\
\dots & \dots & \dots & \dots & \dots & \dots & \dots & \dots & \dots & \dots & \dots & \dots & \dots \\
b_{10}^n & b_{10}^n e^{-s_n T} & \dots & b_{10}^n e^{-s_n lT} & b_{11}^n & b_{11}^n e^{-s_n T} & \dots & b_{11}^n e^{-s_n lT} & \dots & b_{1m}^n & b_{1m}^n e^{-s_n T} & \dots & b_{1m}^n e^{-s_n lT} \\
b_{10}^n & b_{10}^n e^{-s_n^* T} & \dots & b_{10}^n e^{-s_n^* lT} & b_{11}^n & b_{11}^n e^{-s_n^* T} & \dots & b_{11}^n e^{-s_n^* lT} & \dots & b_{1m}^n & b_{1m}^n e^{-s_n^* T} & \dots & b_{1m}^n e^{-s_n^* lT} \\
b_{20}^1 & b_{20}^1 e^{-s_1 T} & \dots & b_{20}^1 e^{-s_1 lT} & b_{21}^1 & b_{21}^1 e^{-s_1 T} & \dots & b_{21}^1 e^{-s_1 lT} & \dots & b_{2m}^1 & b_{2m}^1 e^{-s_1 T} & \dots & b_{2m}^1 e^{-s_1 lT} \\
b_{20}^1 & b_{20}^1 e^{-s_1^* T} & \dots & b_{20}^1 e^{-s_1^* lT} & b_{21}^1 & b_{21}^1 e^{-s_1^* T} & \dots & b_{21}^1 e^{-s_1^* lT} & \dots & b_{2m}^1 & b_{2m}^1 e^{-s_1^* T} & \dots & b_{2m}^1 e^{-s_1^* lT} \\
\dots & \dots & \dots & \dots & \dots & \dots & \dots & \dots & \dots & \dots & \dots & \dots & \dots \\
b_{20}^n & b_{20}^n e^{-s_n T} & \dots & b_{20}^n e^{-s_n lT} & b_{21}^n & b_{21}^n e^{-s_n T} & \dots & b_{21}^n e^{-s_n lT} & \dots & b_{2m}^n & b_{2m}^n e^{-s_n T} & \dots & b_{2m}^n e^{-s_n lT} \\
b_{20}^n & b_{20}^n e^{-s_n^* T} & \dots & b_{20}^n e^{-s_n^* lT} & b_{21}^n & b_{21}^n e^{-s_n^* T} & \dots & b_{21}^n e^{-s_n^* lT} & \dots & b_{2m}^n & b_{2m}^n e^{-s_n^* T} & \dots & b_{2m}^n e^{-s_n^* lT} \\
 & & & & & \dots\ \dots\ \dots\ \dots\ \dots\ \dots & & & & & & & \\
 & & & & & \dots\ \dots\ \dots\ \dots\ \dots\ \dots & & & & & & & \\
b_{j0}^1 & b_{j0}^1 e^{-s_1 T} & \dots & b_{j0}^1 e^{-s_1 lT} & b_{j1}^1 & b_{j1}^1 e^{-s_1 T} & \dots & b_{j1}^1 e^{-s_1 lT} & \dots & b_{jm}^1 & b_{jm}^1 e^{-s_1 T} & \dots & b_{jm}^1 e^{-s_1 lT} \\
b_{j0}^1 & b_{j0}^1 e^{-s_1^* T} & \dots & b_{j0}^1 e^{-s_1^* lT} & b_{j1}^1 & b_{j1}^1 e^{-s_1^* T} & \dots & b_{j1}^1 e^{-s_1^* lT} & \dots & b_{jm}^1 & b_{jm}^1 e^{-s_1^* T} & \dots & b_{jm}^1 e^{-s_1^* lT} \\
\dots & \dots & \dots & \dots & \dots & \dots & \dots & \dots & \dots & \dots & \dots & \dots & \dots \\
b_{j0}^n & b_{j0}^n e^{-s_n T} & \dots & b_{j0}^n e^{-s_n lT} & b_{j1}^n & b_{j1}^n e^{-s_n T} & \dots & b_{j1}^n e^{-s_n lT} & \dots & b_{jm}^n & b_{jm}^n e^{-s_n T} & \dots & b_{jm}^n e^{-s_n lT} \\
b_{j0}^n & b_{j0}^n e^{-s_n^* T} & \dots & b_{j0}^n e^{-s_n^* lT} & b_{j1}^n & b_{j1}^n e^{-s_n^* T} & \dots & b_{j1}^n e^{-s_n^* lT} & \dots & b_{jm}^n & b_{jm}^n e^{-s_n^* T} & \dots & b_{jm}^n e^{-s_n^* lT} \\
 & & & & & \dots\ \dots\ \dots\ \dots\ \dots\ \dots & & & & & & & \\
 & & & & & \dots\ \dots\ \dots\ \dots\ \dots\ \dots & & & & & & & \\
b_{K0}^1 & b_{K0}^1 e^{-s_1 T} & \dots & b_{K0}^1 e^{-s_1 lT} & b_{K1}^1 & b_{K1}^1 e^{-s_1 T} & \dots & b_{K1}^1 e^{-s_1 lT} & \dots & b_{Km}^1 & b_{Km}^1 e^{-s_1 T} & \dots & b_{Km}^1 e^{-s_1 lT} \\
b_{K0}^1 & b_{K0}^1 e^{-s_1^* T} & \dots & b_{K0}^1 e^{-s_1^* lT} & b_{K1}^1 & b_{K1}^1 e^{-s_1^* T} & \dots & b_{K1}^1 e^{-s_1^* lT} & \dots & b_{Km}^1 & b_{Km}^1 e^{-s_1^* T} & \dots & b_{Km}^1 e^{-s_1^* lT} \\
\dots & \dots & \dots & \dots & \dots & \dots & \dots & \dots & \dots & \dots & \dots & \dots & \dots \\
b_{K0}^n & b_{K0}^n e^{-s_n T} & \dots & b_{K0}^n e^{-s_n lT} & b_{K1}^n & b_{K1}^n e^{-s_n T} & \dots & b_{K1}^n e^{-s_n lT} & \dots & b_{Km}^n & b_{Km}^n e^{-s_n T} & \dots & b_{Km}^n e^{-s_n lT} \\
b_{K0}^n & b_{K0}^n e^{-s_n^* T} & \dots & b_{K0}^n e^{-s_n^* lT} & b_{K1}^n & b_{K1}^n e^{-s_n^* T} & \dots & b_{K1}^n e^{-s_n^* lT} & \dots & b_{Km}^n & b_{Km}^n e^{-s_n^* T} & \dots & b_{Km}^n e^{-s_n^* lT} \\
1 & 1 & \dots & 1 & 0 & 0 & \dots & 0 & \dots & 0 & 0 & \dots & 0 \\
\dots & \dots & \dots & \dots & \dots & \dots & \dots & \dots & \dots & \dots & \dots & \dots & \dots \\
\dots & \dots & \dots & \dots & \dots & \dots & \dots & \dots & \dots & \dots & \dots & \dots & \dots \\
0 & 0 & \dots & 0 & 0 & 0 & \dots & 0 & \dots & 1 & 1 & \dots & 1
\end{bmatrix} \tag{5.31}$$

$$P=\begin{bmatrix}
b_{10}^1 & b_{10}^1 e^{-s_1 T} & b_{10}^1 e^{-s_1 2T} & b_{10}^1 e^{-s_1 3T} & b_{10}^1 e^{-s_1 4T} & b_{11}^1 & b_{11}^1 e^{-s_1 T} & b_{11}^1 e^{-s_1 2T} & b_{11}^1 e^{-s_1 3T} & b_{11}^1 e^{-s_1 4T} \\
b_{10}^1 & b_{10}^1 e^{-s_1^* T} & b_{10}^1 e^{-s_1^* 2T} & b_{10}^1 e^{-s_1^* 3T} & b_{10}^1 e^{-s_1^* 4T} & b_{11}^1 & b_{11}^1 e^{-s_1^* T} & b_{11}^1 e^{-s_1^* 2T} & b_{11}^1 e^{-s_1^* 3T} & b_{11}^1 e^{-s_1^* 4T} \\
b_{10}^2 & b_{10}^2 e^{-s_2 T} & b_{10}^2 e^{-s_2 2T} & b_{10}^2 e^{-s_2 3T} & b_{10}^2 e^{-s_2 4T} & b_{11}^2 & b_{11}^2 e^{-s_2 T} & b_{11}^2 e^{-s_2 2T} & b_{11}^2 e^{-s_2 3T} & b_{11}^2 e^{-s_2 4T} \\
b_{10}^2 & b_{10}^2 e^{-s_2^* T} & b_{10}^2 e^{-s_2^* 2T} & b_{10}^2 e^{-s_2^* 3T} & b_{10}^2 e^{-s_2^* 4T} & b_{11}^2 & b_{11}^2 e^{-s_2^* T} & b_{11}^2 e^{-s_2^* 2T} & b_{11}^2 e^{-s_2^* 3T} & b_{11}^2 e^{-s_2^* 4T} \\
b_{20}^1 & b_{20}^1 e^{-s_3 T} & b_{20}^1 e^{-s_3 2T} & b_{20}^1 e^{-s_3 3T} & b_{20}^1 e^{-s_3 4T} & b_{21}^1 & b_{21}^1 e^{-s_3 T} & b_{21}^1 e^{-s_3 2T} & b_{21}^1 e^{-s_3 3T} & b_{21}^1 e^{-s_3 4T} \\
b_{20}^1 & b_{20}^1 e^{-s_3^* T} & b_{20}^1 e^{-s_3^* 2T} & b_{20}^1 e^{-s_3^* 3T} & b_{20}^1 e^{-s_3^* 4T} & b_{21}^1 & b_{21}^1 e^{-s_3^* T} & b_{21}^1 e^{-s_3^* 2T} & b_{21}^1 e^{-s_3^* 3T} & b_{21}^1 e^{-s_3^* 4T} \\
b_{20}^2 & b_{20}^2 e^{-s_4 T} & b_{20}^2 e^{-s_4 2T} & b_{20}^2 e^{-s_4 3T} & b_{20}^2 e^{-s_4 4T} & b_{21}^2 & b_{21}^2 e^{-s_4 T} & b_{21}^2 e^{-s_4 2T} & b_{21}^2 e^{-s_4 3T} & b_{21}^2 e^{-s_4 4T} \\
b_{20}^2 & b_{20}^2 e^{-s_4^* T} & b_{20}^2 e^{-s_4^* 2T} & b_{20}^2 e^{-s_4^* 3T} & b_{20}^2 e^{-s_4^* 4T} & b_{21}^2 & b_{21}^2 e^{-s_4^* T} & b_{21}^2 e^{-s_4^* 2T} & b_{21}^2 e^{-s_4^* 3T} & b_{21}^2 e^{-s_4^* 4T} \\
1 & 1 & 1 & 1 & 1 & 0 & 0 & 0 & 0 & 0 \\
0 & 0 & 0 & 0 & 0 & 1 & 1 & 1 & 1 & 1
\end{bmatrix} \tag{5.32}$$

5.6 Robust multiple-input multiple-output input shaping design for multiple-mode vibrations reduction

Input shaping techniques, regardless of being used for single or multiple-input/output, work very well in suppressing vibrations when modeling parameters are very accurate. However, as the parameter uncertainty becomes larger, the amount of residual vibrations promptly increases beyond the acceptable level. This can be very obvious when we plot sensitivity curves relative to normalized frequency and normalized damping, as shown in the previous chapter. For first-order robust input shapers, although the residual vibrations is zero at the modeled parameter (frequency or damping), it increases exponentially when the actual parameter deviates from its modeled one. When shapers are designed for second-order robustness, the sensitivity curves, in addition to having zero vibrations at the modeled parameter, also have zero slope when there is no modeling error.
The amount of residual vibrations in second-order robustness shapers increases more gradually than for first-order shapers as the parameter uncertainty increases. The higher the robustness order the slower becomes the increase in residual vibrations when modeled parameter deviates from actual parameter. This higher order in robustness can be achieved either by adding derivative constraints or placing additional zeros close to flexible system poles.

In the case of MISO shaping technique discussed in Section.5.2, improving robustness to be of a second-order can be achieved by placing two zeros at each flexible pole. Hence, a total of $4n$ zeros would be required for a system with n flexible modes. Accordingly the number of impulses per shaper would be doubled to be $l = \frac{4n}{m+1}$. The additional $2n$ zeros also would add extra $2n$ more rows to the P matrix shown in Eq.5.10.
These additional rows are actually additional constraint equations that require the number of zeros in the W vector to be also doubled to become: $W = [\begin{smallmatrix} 0_{4n\times 1} \\ 1_{(m+1)\times 1} \end{smallmatrix}]$, for the amplitude vector a to be solved.

Similar changes can be made to achieve even higher-order robustness. While the second-order robustness shaper is longer, it keeps the amount of residual vibrations much smaller than the first-order robustness shaper in the presence of parameter uncertainty. However, this happens on the expense of adding more delay to the applied shaped input. The robustness method explained in Section.5.4 doesn't double the number of shaper impulses, but rather adds $2R$ number of impulses. This allows to customize the robustness of the designed shaper to fit the constraints requirements.

The robustness of MIMO shapers can be achieved using the exact same ways explained for MISO shapers. However, since the number of rows in the MIMO P matrix is scaled by K (the number of outputs) compared to the MISO one, then the dimensions of the large P matrix becomes $k(4n + m + 1) \times (m + 1)(l + 1))$ for a second-order robustness. This even makes the approach much more challenging to be used, since finding smallest T which satisfies that all impulse amplitudes positive might not be an option. While the results of using this approach demonstrate the feasibility and promise of multiple-input multiple-output shaping, a number of issues should be considered for further study. These issues include but not limited to, thinking of shapers with impulses which are unevenly spaced or investigating the use of unequal number of impulses for each input shaper. Removing these assumptions will likely lead to an even further increase in the time savings of the MIMO input shaping approach.

5.7 Conclusions

This chapter presented the design of input shapers for multiple-input systems with single-output (MISO) which we extended into a generalized form of a new multivariable shapers for multiple-input multiple-output systems (MIMO). The approach discussed initially for the multiple-input single-output systems shows its advantage over the traditional approach where all input shapers are designed to be identical for all inputs. Although the MISO approach generates shapers with larger impulse spacing T than the traditional one, however, the total shaper length is shorter due to the fewer number of impulses per input shaper. How much shorter the MISO shaper lengths are depends on the input matrix B and the flexible frequencies and damping ratios of the system. Modified versions of the MISO approach were discussed later in this chapter to reduce the computational complexity, made the design process easier to be implemented and improve shapers robustness with respect to systems parameters uncertainties. A generic feedforward vibrations suppression technique for multiple-input multiple-output systems with multiple-mode of vibrations was discussed last in this chapter. For that, we extended the multiple-input single-output zero placement input shaping technique into multiple-input multiple-output technique. The presented multivariable approach permits to reduce multiple-mode of vibrations in both the direct and cross-coupling transfers. It is very promising for systems where using sensors are difficult and impossible. This new approach only requires knowing system input matrix and system poles information for the design of the compensator, which make it a straightforward and easy to design approach. The results of applying this approach on different types of actuators are presented in the next chapter.

Chapter 6

Experimental applications

This chapter presents the results of applying the newly developed multivariable input shaping technique on different types of piezoelectric actuators. The new multivariable approach was tested on one cantilever structured and two different tube actuators. The experimental setup associated with each actuator was presented first, then each actuator was characterized and modeled to help calculating the shapers. The robustness of the new control scheme was also tested against temperature fluctuations. All results clearly showed the effectiveness and the robustness of the new approach in reducing vibrations.

Contents

6.1 Introduction

Most of positioning and gripping systems, which require high accuracy, are often based on active smart materials. Among these active materials, piezoelectric ones are widespread and their use continues to grow due to their fast response and high resolution capabilities. Piezoelectric materials are particularly respected and very common in tube scanners for AFM microscopes, in piezocantilevers and microgrippers for micromanipulation/microassembly and in actuators for step-by-step microrobots. Unfortunately, piezotubes and piezocantilevers performances are strongly affected by nonlinearities (hysteresis and creep) and suffer from poorly damped vibrations. This thesis work is only concerned about vibrations reduction in piezoactuators, tubes and cantilevers. Although feedback control techniques seem to be a good way to reach overall substantial performances (accuracy, repeatability, disturbances and vibration rejection, etc.). However, the use of closed loop control techniques in miniaturized systems in general is strongly limited by the difficulty to integrate sensors which are bulky when need to be precise and fast enough. Hence, open-loop control techniques are alternative ways to overcome this problem. Different feedforward control schemes, that can be possibly used in such miniaturized systems, were presented in chapter 2 of this thesis. The inversion-based feedforward schemes, out of those presented in chapter 2, are commonly used to precisely track a given actuator's trajectory. The essential idea in these inversion-based techniques is to achieve the required performance by inverting the actuator dynamics. For nonminimum-phase systems, this inversion can't be a direct-inversion due to the existence of unstable zeros, hence the need to use the so called approximate-inversions. Different versions of the approximate-inversion techniques were presented in Subsection.3.2.2, Subsection.3.2.3 and Subsection.3.2.4. Other feedforward methods, besides inversion-based feedforward, can be used to minimize excitation of actuators structural frequencies. Input shaping is one of these technique which was proven to be very effective in vibration reduction. Major varieties of these techniques, which are strictly being used for single-input single-output systems, were presented in Section.3.4. The literature is very rich with such SISO input shaping techniques associated with single degree of freedom actuators. However, the fast and recent evolvement in the field of nanopositioning was a major drive to motivate researchers to exploit the advantages of input shaping technique so it can be extended to be used for MIMO systems. This thesis work demonstrates a newly developed multivariable input shaping technique as an open loop control technique that can be an effective approach for vibrations reduction. This chapter discusses different setups that were used over the course of this study to validate the newly developed technique. The experimental setup and modeling of a 2DOF piezoelectric cantilever structured actuator is presented in Subsection.6.2.1, where Subsection.6.2.2 and Subsection.6.2.3 present the

same for two different types of piezotube actuators. The results of applying the multivariable technique on all of these actuators are presented in Subsection.6.3.1, Subsection.6.3.2 and Subsection.6.3.3 respectively.

6.2 Presentation of the experimental setup

6.2.1 The 2-DOF piezoelectric cantilever structured actuator

6.2.1.1 Presentation of the actuator

Piezoelectric cantilever structures are one of the most commonly used structures in piezoelectrically actuated systems. The principle of the 2-DOF piezoelectric micropositioner which we used in this thesis was patented in 2002 [145]. It is capable to perform microrobotic tasks such as micromanipulation with sub-micrometric resolution and along two axes [146,156]. Unlike the 2-DOF bi-layered piezocantilever developed in [13], the one used in this thesis is made up of 36 piezoelectric layers to permit using lower voltage to obtain the same output deflection. Fig.6.1 (b) shows this piezocantilever which deflects along y-axis ($y1$) and/or z-axis ($y2$) by applying input voltages on Uy ($u1$) and/or Uz ($u2$) respectively. The total dimensions of the active part are: $25mm \times 1mm \times 1mm$. To measure these deflections (displacements), two inductive sensors (ECL202 from IBS) are used. The sensors are tuned to have measurement resolution of tens of nanometers and a bandwidth in excess of 2kHz. The voltages and the measurement signals are generated and acquired by a computer with a dSPACE board embedding an ADC and DAC converters, shown in Fig.6.1 (a). The sampling time of the whole acquisition system is set to $50\mu s$ which is sufficient to consider all dynamics of the actuators and of the sensors.

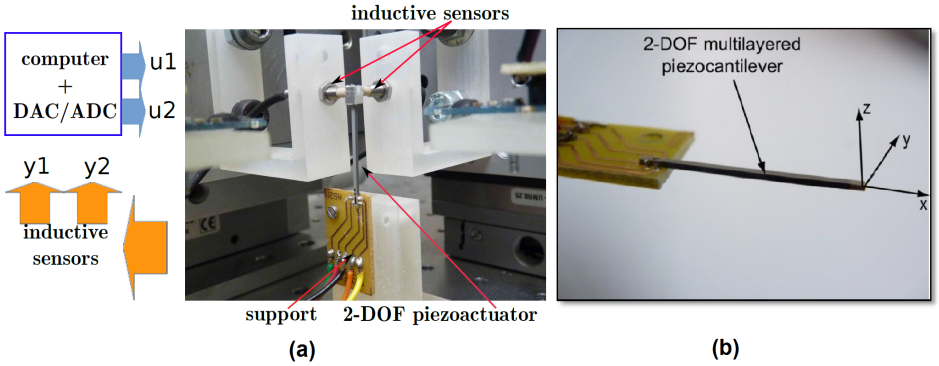

Figure 6.1: (a) The experimental setup diagram (b) The 2-DOF piezocantilever.

6.2.1.2 Characterization

For the purpose of our study on this actuator, static and dynamic characteristics were studied. The static characteristics were obtained by applying a sine input voltage $u1$ (resp. $u2$) to the piezoactuator with $u2$ (resp. $u1$) left equal to zero and by recording the output displacements $y1$ and $y2$. The amplitude is taken to be the maximal range of use ($10\,V$ in this case) and the frequency is taken to be sufficiently low in order to avoid the phase-lag due to high dynamics, but not too low in order to avoid the creep effect [11]. Different experiments have shown that a frequency of $0.1Hz$ is convenient for this actuator. Fig.6.2-a depicts the output $y1$ versus the input $u1$, i.e the ($u1$, $y1$)-plane, and Fig.6.2-d depicts the ($u2$,$y2$)-plane. These two planes give the direct transfers of the 2-DOF piezoactuator which are clearly hysteretic. On the other hand, Fig.6.2-b and Fig.6.2-c depicts ($u2$, $y1$)-plane and the ($u1$, $y2$)-plane respectively and which are the cross-couplings. The creep nonlinearity of the piezoactuator is evidenced when a step voltage is applied and the output $y1$ or $y2$ is observed during a long duration time. In this actuator, the creep is still evolving even several minutes after the step was applied. Fig.6.2-e and h depict the direct creep characteristics of the actuator observed during $5min$ and Fig.6.2-f and g depict the cross-couplings creep. Finally, to characterize the dynamics, a step input voltage is applied.

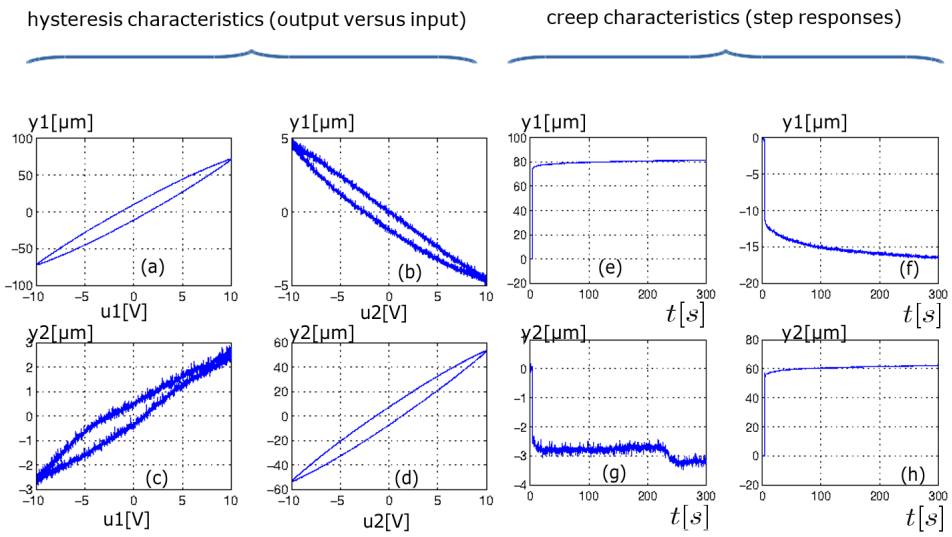

Figure 6.2: Low frequency and low-rate characteristics of the 2-DOF piezoactuator.

Then, the part of the step response before the creep starts is observed and can be used to identify these dynamics. Notice that both the creep and the transient part for the dynamics are observed from a step response.
However, the creep is very low rate phenomena and thus observed during a

long time duration whilst the dynamics is a very quick phenomena observed during tens or a hundred of millisecond. Fig.6.3-a and d depict the transient parts (direct transfers) of the step responses of the actuator and Fig.6.3-b and c correspond to the cross-couplings transient parts. As we can see, the actuators exhibit badly damped oscillations. As a consequence, the actuator possesses a very quick rise-time, however the settling time is very long relative to this.

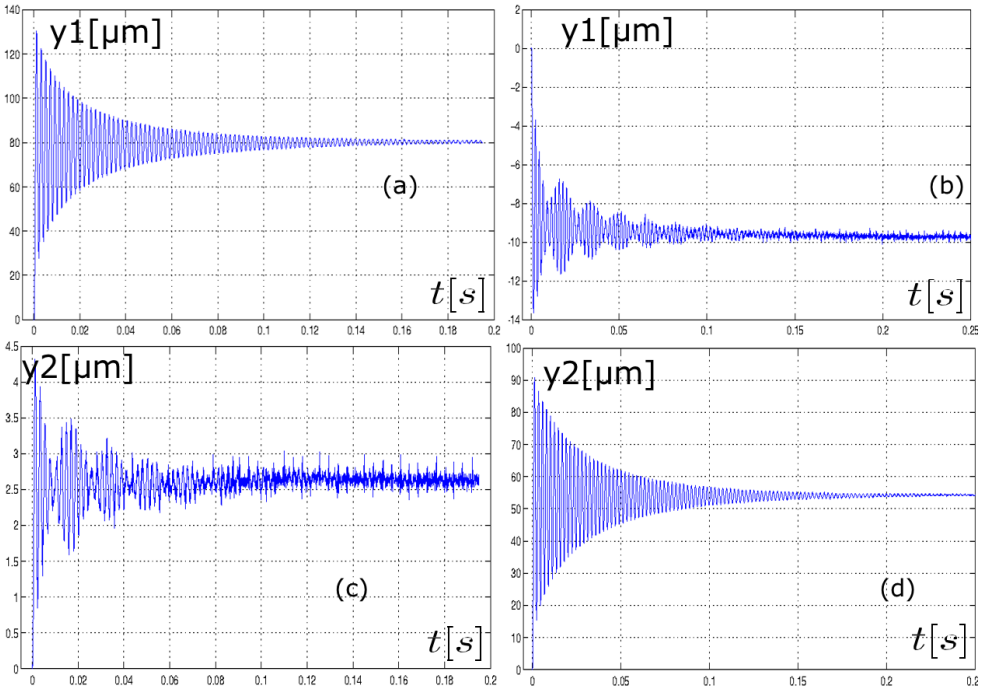

Figure 6.3: Step responses observed during a very short duration time.

6.2.1.3 Modeling and identification

In order to synthesis a feedforward and/or feedback controller, a model of the piezoelectric cantilever actuator is essential. It was shown that a 1-DOF piezoactuator can be modeled by an uncertain linear model with fictive disturbance where the hysteresis and the creep are included in the uncertainties and in the disturbance [10–12, 154]. That is:

$$y(s) = G(s)u(s) + d(s) \tag{6.1}$$

where $G(s)$ is an uncertain linear transfer function, $d(s)$ is the disturbance and s is the Laplace variable. By extending the 1-DOF model in Eq.6.1 into

2-DOF, we have:

$$y(s) = \begin{pmatrix} y1(s) \\ y2(s) \end{pmatrix} = \begin{cases} G_1(s)u_1(s) + G_{12}(s)u_2(s) + d_1(s) \\ G_2(s)u_2(s) + G_{21}(s)u_1(s) + d_2(s) \end{cases} \tag{6.2}$$

$$y(s) = G(s) \begin{pmatrix} u_1(s) \\ u_2(s) \end{pmatrix} + \begin{pmatrix} d_1(s) \\ d_2(s) \end{pmatrix} = G(s)u(s) + d(s) \tag{6.3}$$

where

$$G(s) = \begin{pmatrix} G_1(s) & G_{12}(s) \\ G_{21}(s) & G_2(s) \end{pmatrix} \tag{6.4}$$

By applying a Box-Jenkins parametric identification technique to the experimental data in Fig.6.3 and by limiting the order of each transfer by four, we obtain:

$$\begin{cases} G_1(s) = \frac{-7881(s-9808)(s^2+309s+1.2\times10^7)}{(s^2+67s+1\times107)(s2+933s+1.1\times10^7)} \\ G_{12}(s) = \frac{-777(s+21)(s^2+2319s+2\times10^7)}{(s+2181)(s+20)(s^2+84s+8\times10^6)} \\ G_{21}(s) = \frac{-88(s-3\times10^5)(s^2+7739s+3\times10^8)}{(s2+349s+7\times10^6)(s^2+154s+4\times10^9)} \\ G_2(s) = \frac{-3140(s-1.3\times10^4)(s^2+680s+1\times10^7)}{(s2+59s+8\times10^7)(s^2+1654s+1\times10^7)} \end{cases} \tag{6.5}$$

By transforming the 2-DOF model in Eq.6.2 into a state-space model, we obtain:

$$\begin{cases} \frac{dx(t)}{dt} = Ax(t) + Bu(t) \\ y(t) = Cx(t) + d(t) \end{cases} \tag{6.6}$$

which is shown in Fig.6.4, where the state matrix A, the input matrix B and the output matrix C, with appropriate dimensions, could be uncertain due to hysteresis and creep as mentioned above. The size of the state vector $x(t)$ is defined by the size of the matrix $G(s)$ which is itself defined during the identification procedure above. The different schemes that were applied to this system are demonstrated in Subsection.6.3.1.

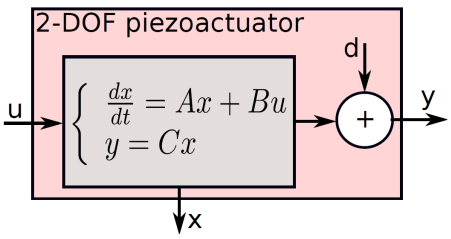

Figure 6.4: The cantilever system model.

6.2.2 The 3-DOF Piezoelectric Tube Actuator, PT230.94

6.2.2.1 Presentation of the actuator

Like Piezoelectric cantilevers, piezoelectric tube actuators are also used extensively in micro/nano positioning applications, in particular Scanning Tunneling Microscopes (STMs) and Atomic Force Microscopes (AFMs). In such microscopes a probe is usually placed a few nanometers from the material surface for which a topographical map is required. The sample is placed on top of the piezoelectric tube which is actuated in a raster pattern, as shown in Fig.5.4.

This subsection demonstrates the 3-DOF piezoelectric tube actuator, piezotube PT230 from PIceramic company, which was used in this thesis work to verify the newly developed multivariable input shaping technique. PT230.94 3-DOF positionner can provide deflections along X, Y and Z axis as shown in Fig.6.5. In fact, when a positive voltage +U is applied to +x electrode and a negative voltage -U to -x electrode, the first sector expands while the second one contracts. This expansion and contraction result in a deflection of the overall piezotube along the X direction (Fig.6.5 (c)). The same tube deflection is obtained along the Y direction if the voltages are applied to +y and -y electrodes (Fig.6.5 (d)). The tube extension along Z axis is obtained by applying the same voltage (+U or -U) simultaneously on the four electrodes +x, -x, +y and -y (Fig.6.5 (e)).

The experimental setup, depicted in Fig.6.6, is composed of: (1) The Piezotube PT230.94 actuator, which is 30 mm in length and has a 3.2 mm external diameter and can tolerate up to $\pm 200V$ voltages range. (2) Three inductive sensors (ECL202 from IBS company, Eindhoven, Netherlands) that are used to measure the displacements x, y and z. The sensors are tuned to have $40nm$ of resolution, $\pm 250\mu m$ of measurement range and $15kHz$ of bandwidth. Notice that the sensors are only used to characterize the oscillations of the actuator and to verify the performances of the control technique, they are not used to make a feedback control. (3) A computer equipped with a dSPACE data acquisition board to manage the different signals (voltages, reference input and measured output) and to implement the input shaping controller. The sampling time is set to $50\mu s$, which is largely sufficient to consider the dynamics of the actuator in our case. (4) Three high-voltage (HV) amplifiers used to amplify the control signals ux, uz and uz from the dSPACE board before supplying the piezoactuator. The amplifiers can provide up to $\pm 200V$.

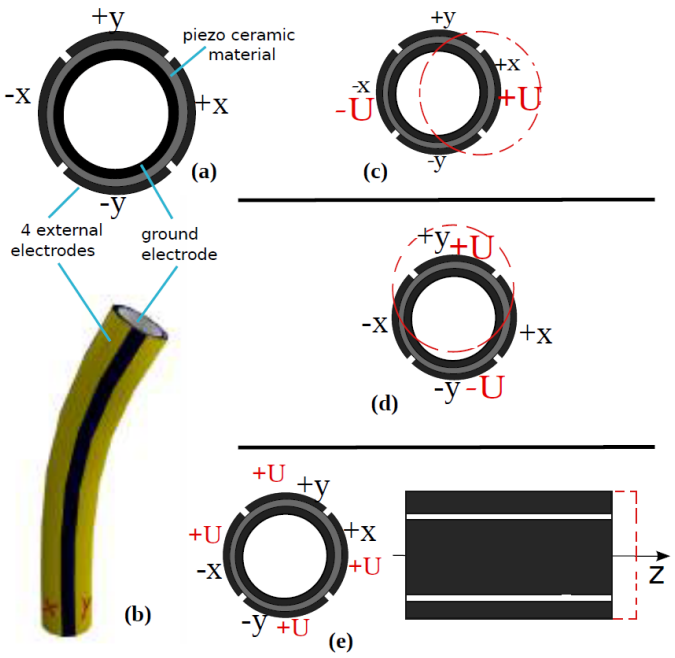

Figure 6.5: Piezoelectric tube structure and operation:(a) Top view, showing four external electrodes and an internal ground electrode, separated by piezoelectric material; (b) A perspective view of the piezoelectric tube; (c) deflection along X axis; (d) deflection along Y axis, and (e) elongation along Z axis.

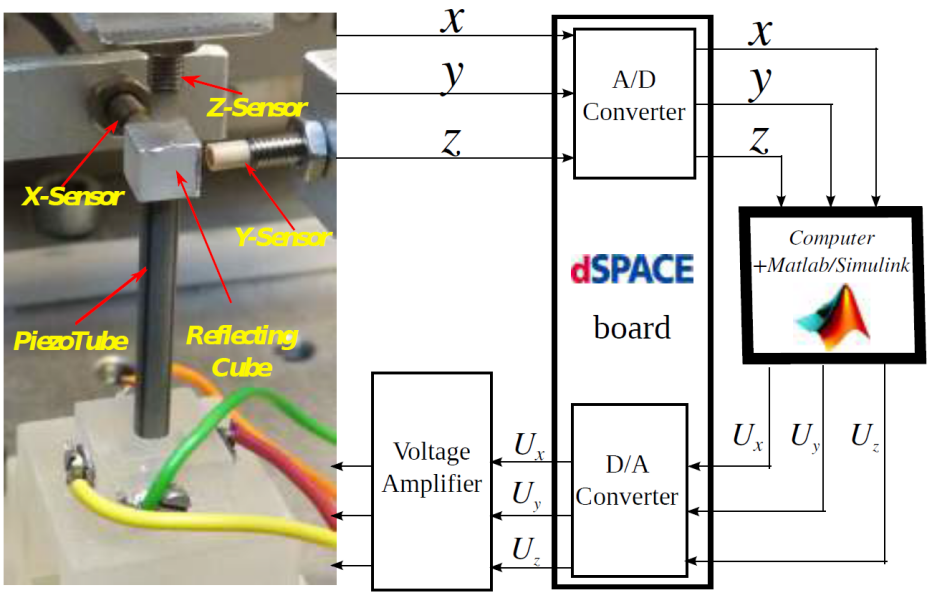

Figure 6.6: The PT230 experimental setup.

6.2.2.2 Characterization

This piezotube actuator was also characterized using the same procedure we used to characterize the 2-DOF piezocantilever. We apply first a sine input signal of $200V$ at one input and we leave all other input signals to be equal to zero. The frequency of the sine input signal was chosen to be $0.1Hz$ as a good compromise to isolate the rate independent hysteresis from the phase lag and creep effects. The curves in Fig.6.7-(a), (e) and (i) represent the direct hysteresis for X, Y and Z respectively. The remaining curves represent the cross-couplings hysteresis caused by the minor misalignment of the actuator electrodes which results in a diagonal bending instead of purely axial bending. The creep nonlinearity was characterized by applying a step inputs of amplitude equal to $200V$. Fig.6.8 shows the results observed for the creep over the course of $600s$. Fig.6.8-(a),(e) and (i) show the direct creep and Fig.6.8-(b),(c),(d),(f),(g) and (h) show the couplings creeps. As we can see, the creep can have positive or negative evolution.

The dynamics can be observed by applying step inputs of the same amplitude $200V$ over the course of a shorter time period which is in our case equal to $20ms$. Fig.6.9-(a),(e) and (i) show the direct step responses while Fig.6.9-(b),(c),(d),(f),(g) and (h), show the cross-couplings step responses. These figures demonstrate the poorly damped oscillations in the different responses.

6.2.2.3 Modeling and identification

The piezotube under test (shown in Fig.6.6) was identified by firstly recording step responses for all of its three outputs when exciting each of x, y and z inputs separately (shown in Fig.6.9) , then plugging these recorded input and output traces to the MATLAB ARMAX (Auto Regressive Moving Average with eXternal inputs) system identification toolkit to generate the best fit function that relates each output to each input [147]. As a result, nine different transfer functions for the direct and cross couplings were derived.

To be able to use the design approach explained in Section.5.5, all of these transfer functions need to be reduced to second order transfer functions by only retaining dominant pole approximation. The second order model of the piezoelectric tube can be expressed as a 3×3 matrix:

$$G(s) = \begin{pmatrix} G_{XU_x}(s) & G_{XU_y}(s) & G_{XU_z}(s) \\ G_{YU_x}(s) & G_{YU_y}(s) & G_{YU_z}(s) \\ G_{ZU_x}(s) & G_{ZU_y}(s) & G_{ZU_z}(s) \end{pmatrix} \tag{6.7}$$

The diagonal elements of this 3×3 matrix are the direct transfer function, where the rest of them are the cross coupling transfer functions. Eq.6.8,

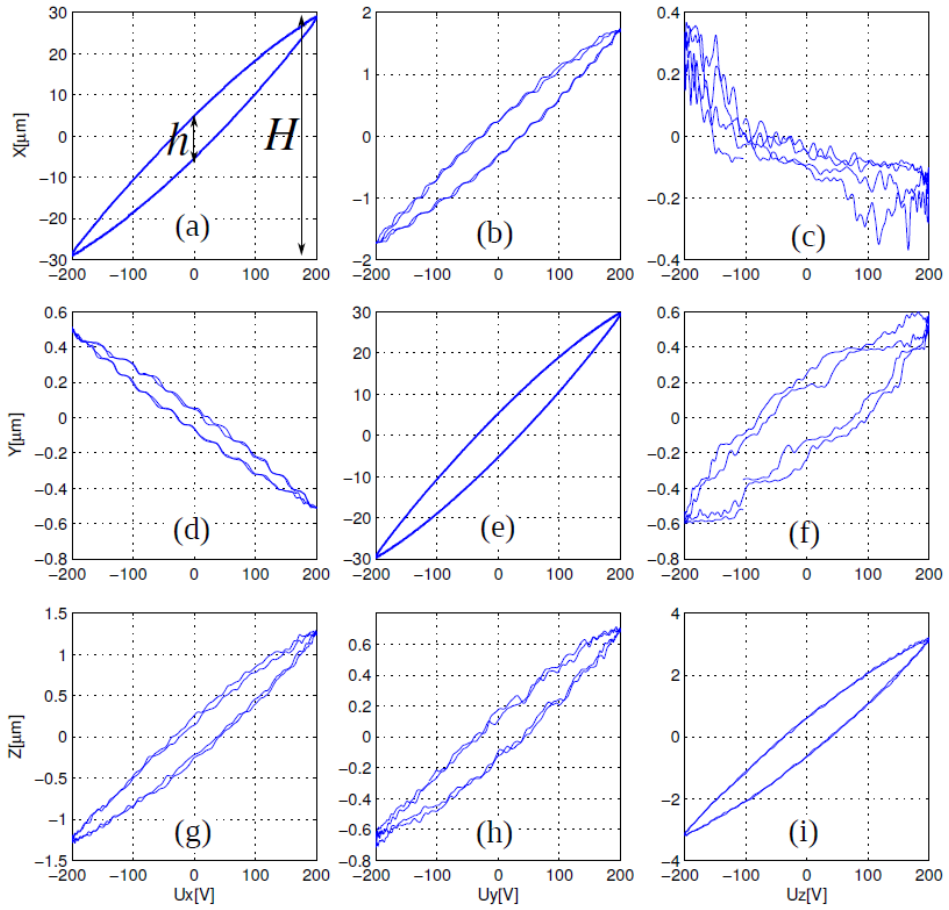

Figure 6.7: Hysteresis characterization with input sinusoidal signals of amplitude 200V and of frequency $0.1Hz$.

Eq.6.9 and Eq.6.10 show the first,second and third rows of the system model matrix which lists the transfer functions between each of the 3 inputs and the first, second and third output respectively. These rows also correspond different subplots in Fig.6.9. For example, Eq.6.9 lists the transfer functions which correspond to subplots Fig.6.9-d, Fig.6.9-e and Fig.6.9-f.

$$Input\rangle\,(U_x, U_y, U_z) \Rightarrow Output\rangle\,X \begin{cases} G_{XU_x} = \frac{2.651e08}{62.53s^2+4.087e04s+2.064e09} \\ G_{XU_y} = \frac{-1.145e06}{13.62s^2+8230s+4.6e08} \\ G_{XU_z} = \frac{-1.368e04}{13.15s^2+942.7s+1.967e07} \end{cases} \tag{6.8}$$

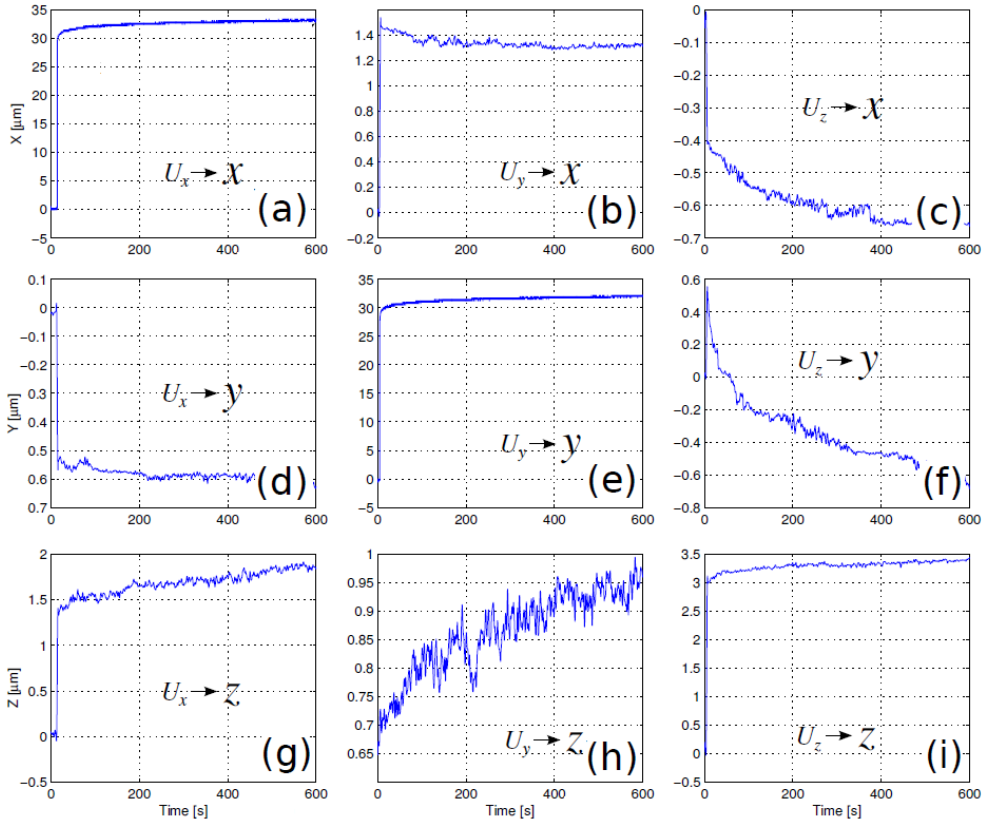

Figure 6.8: Creep characterization over a period of $600s$.

$$Input\rangle\,(U_x, U_y, U_z) \Rightarrow Output\rangle\,Y \begin{cases} G_{YU_x} = \frac{-2.966e08}{9499s^2+4.535e06s+3.167e11} \\ G_{YU_y} = \frac{3.004e12}{347810s^2+1.283e08s+1.938e13} \\ G_{YU_z} = \frac{38.16}{0.3513s^2+2.772s+7.309e04} \end{cases} \tag{6.9}$$

$$Input\rangle\,(U_x, U_y, U_z) \Rightarrow Output\rangle\,Z \begin{cases} G_{ZU_x} = \frac{9.786e07}{279.9s^2+3.539e05s+5.48e09} \\ G_{ZU_y} = \frac{6.638e06}{14.08s^2+2719s+7.969e08} \\ G_{ZU_z} = \frac{-2.084e08}{91.29s^2+7186s+2.327e10} \end{cases} \tag{6.10}$$

The resultant poles from these second order transfer functions are required for the formulation of the P matrix (shown in its generic form in Eq.5.31)

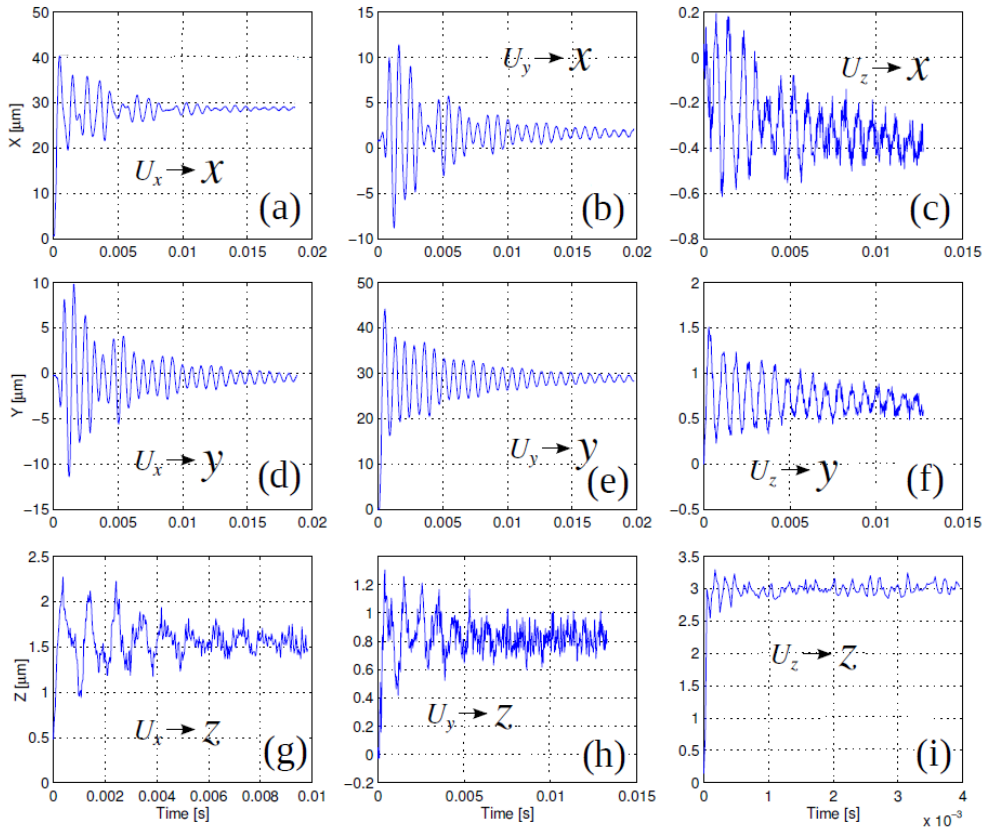

Figure 6.9: Dynamics characterization observed during $20ms$.

as will be explained in Subsection.6.3.2. Since our actuator is a 3DOF system, we have nine transfer functions and nine poles with their conjugates, as listed below:

S1x = −326.7763 + 5736.0199 i;	S1y = −238.7149 + 5769.0893 i;	S1z = −632.18957 + 4379.5395 i;
S1xc = −326.7763 − 5736.0199 i;	S1yc = −238.7149 − 5769.0893 i;	S1zc = −632.18957 − 4379.5395 i;
S2x = −302.1598 + 5803.7510 i;	S2y = −184.4922 + 7461.7891 i;	S2z = −96.572358 + 7522.7038 i;
S2xc = −302.1598 − 5803.7510 i;	S2yc = −184.4922 − 7461.7891 i;	S2zc = −96.572358 − 7522.7038 i;
S3x = −35.84556 + 1222.5863 i;	S3y = −3.945002 + 456.10520 i;	S3z = −39.356673 + 15967.113 i;
S3xc = −35.84556 − 1222.5863 i;	S3yc = −3.945002 − 456.10520 i;	S3zc = −39.356673 − 15967.113 i;

6.2.3 The 3-DOF Piezoelectric Tube Actuator, TB6309

6.2.3.1 Presentation of the actuator

Another 3-DOF Piezotube (TB6309 $80\mu m$ range) actuator was used over the course of this study to further verify the robustness of the newly developed multivariable input shaping technique against temperature fluctu-

ations. The tube was manufactured to have radially poled piezoelectric material with four external electrodes as show in Fig.6.10(b). The tube has a 63.5 mm length, 9.525 mm diameter and 0.66 mm thickness. To excite the tube, a Piezo drive power amplifier was used to apply voltage difference at the poles of the tube so it deflects in X or/and Y directions. The tube was glued to an acrylic sheet which in turn was bolted to a linear stage for position adjustment. Aluminum frame structure was used to attach two fiber optic displacement D20-Philtech sensors and an IR temperature sensor to the system. The fiber optic sensors were also mounted via linear stages to the aluminum structure for position adjustment. Aluminium cubical guide was added on top of the piezo tube to obtain consistent readings and to ease the displacement sensors' calibration. The natural frequency of the piezoelectric tube can be changed by adjusting the mass of this guide cube. This mass adjustment can be achieved by adding screws to pre-made holes in the guide cube. To adjust the temperature around the tube, a nichrome alloy heating element consists of a coil obtained from a commercial hair dryer was wound in using the support of simple wooden structure. The heating element was connected to a universal power module in order to supply the required heating current, Fig.6.10 (a).

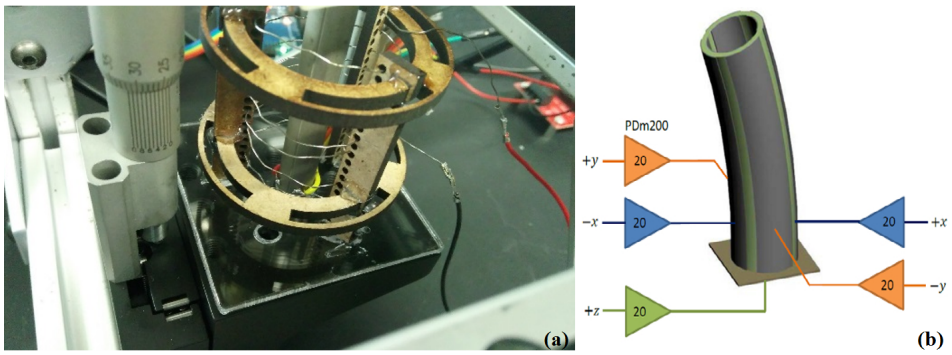

Figure 6.10: (a) Heating element around the piezotube (b) TB6309 piezo tube.

The CAD drawing and the actual model of the experimental setup, featuring the piezoelectric tube actuator, the linear stages, the heating elements and the fiber optic displacement sensors are shown in Fig.6.11. The tube temperature was measured using IR temperature sensor. The IR TEMP sensor was controlled via an Arduino board after being calibrated to read linearly a temperature range from 20 – 50 degrees Celsius. Fig.6.12 shows all the components used in the experimental setup. The piezoelectric tubes electrodes are connected to the PDm 200 PiezoDrive power amplifiers. The amplifiers require a steady voltage of +/- 16 V which is supplied by the NI virtual benchs programmable power supply. The input signal for actuating the piezoelectric tube through the PDm 200 amplifiers are provided by the

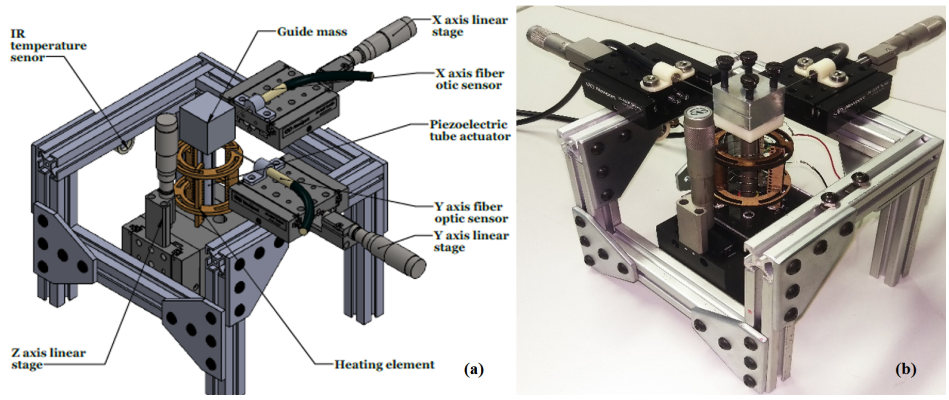

Figure 6.11: (a) The setup CAD drawing (b) The actual piezoelectric tube setup.

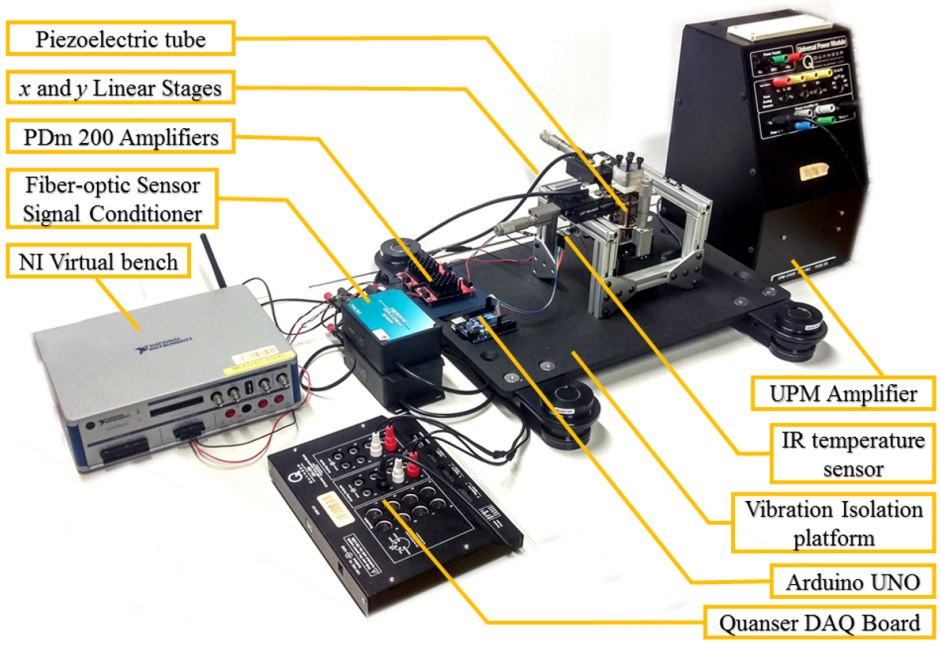

Figure 6.12: All the components used in the experimental setup.

Quanser DAQ boards analog output channels. The position measurement from the fiber-optic sensors fixed to the linear stage is processed by the fiber-optic signal conditioners. The conditioned signals are then relayed to the computer through the analog input channels of the Quanser DAQ board.

The heating element constructed around the piezoelectric tube is connected to the UPM power amplifier. The power to the heating element is modulated using the analog output channel from the Quanser DAQ Board. The

readings from the IR temperature sensor are acquired via an Arduino UNO board. Both the Arduino UNO and the Quanser DAQ boards are connected to the computer via USB cables (Not shown in the figure).

The complete schematic of the process is shown in Fig.6.13. The temperature of the piezoelectric tube was controlled by using the heating element and the IR temperature sensor. The piezoelectric tubes actuation and vibration measurement was done through the Quanser DAQ board.

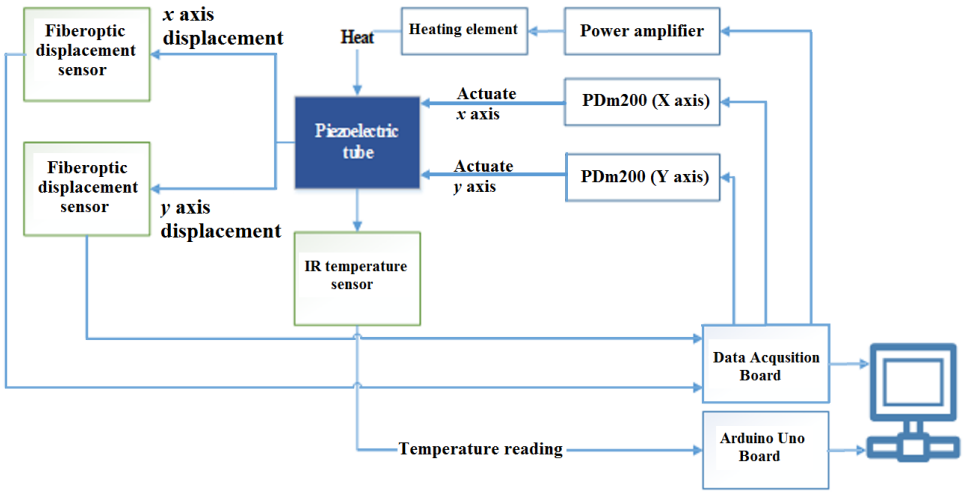

Figure 6.13: Schematic of the experimental setup working flow.

6.2.3.2 Modeling and identification

As in the previous actuators' modeling, the step responses for the TB6309 piezoelectric tube in direct and cross couplings at four different temperatures 25, 30, 35 and 40 were obtained. These recorded step responses (shown in Fig.6.14) along with their exciting inputs were plugged to MATLAB system identification tool kit (ident) to model the tube at each of the four aforementioned different temperatures. At each temperature we obtain four transfer functions G_{XU_x} and G_{YU_y} for the direct and G_{XU_y} and G_{YU_x} for cross couplings.

The matrix form for these transfer functions is:

$$G(s) = \begin{pmatrix} G_{XU_x}(s) & G_{XU_y}(s) \\ G_{YU_x}(s) & G_{YU_y}(s) \end{pmatrix} \tag{6.11}$$

Eq.6.12, Eq.6.13, Eq.6.14 and Eq.6.15 show the second order models of the tube at 25, 30, 35 and 40 C respectively.

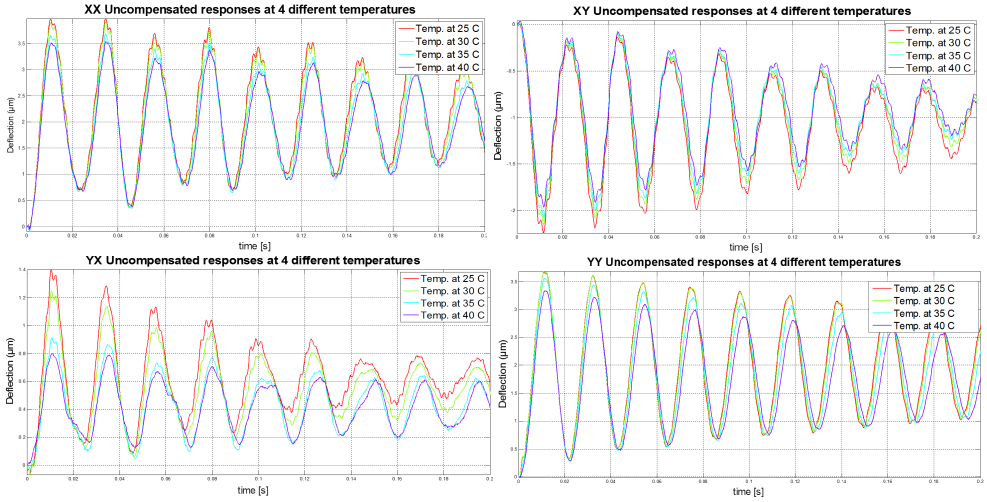

Figure 6.14: Uncompensated XX, XY, YX and YY responses at 4 different temperatures (Experimental).

$$G(s)|_{Temp25} = \begin{pmatrix} \frac{3.393s+1.017e04}{s^2+13.19s+7.752e04} & \frac{-9.012s+1340}{s^2+9.44s+7.979e04} \\ \frac{-3.081s+421}{s^2+7.204s+7.944e04} & \frac{-4.983s+5650}{s^2+7.753s+8.745e04} \end{pmatrix} \tag{6.12}$$

$$G(s)|_{Temp30} = \begin{pmatrix} \frac{2.517s+1.071e04}{s^2+12.44s+7.47e04} & \frac{-4.709s+1849}{s^2+13.43s+7.507e04} \\ \frac{-2.574s+544.2}{s^2+6.725s+7.857e04} & \frac{-2.674s+5698}{s^2+7.753s+8.745e04} \end{pmatrix} \tag{6.13}$$

$$G(s)|_{Temp35} = \begin{pmatrix} \frac{-3.953s+9690}{s^2+14.09s+7.35e04} & \frac{-6.423s+1906}{s^2+9.244s+7.441e04} \\ \frac{-1.672s+312.1}{s^2+8.197s+7.505e04} & \frac{-3.203s+4428}{s^2+10.09s+8.497e04} \end{pmatrix} \tag{6.14}$$

$$G(s)|_{Temp40} = \begin{pmatrix} \frac{-79.49s+7.309e04}{s^2+1510s+5.073e05} & \frac{4.315s+2.287}{s^2+123.3s+59.51} \\ \frac{1.542s+339.3}{s^2+9.792s+7.294e04} & \frac{-6.215s+5380}{s^2+24.81s+7.951e04} \end{pmatrix} \tag{6.15}$$

Fig.6.15 shows the obtained 2nd order models in blue color versus the collected data in red color. The system parameters (ω_n,ζ) and system poles derived from the second order models at the four temperatures are listed in Table.6.1. These variations in system parameters can be looked at as an uncertainties which need to compensated for to have a robust controller against temperature fluctuations, as will be explained later in this chapter.

w_n	25	30	35	40
XX	280.9777	280.4628	279.5476	278.4847
XY	280.8221	280.3053	279.4475	278.5837
YX	280.0686	279.6645	278.939	276.8787
YY	295.7951	295.2625	293.9908	292.043

ζ	25	30	35	40
XX	0.013779	0.01431	0.014718	0.015664
XY	0.015231	0.016593	0.018167	0.018169
YX	0.018307	0.014845	0.011676	0.014148
YY	0.013838	0.013615	0.014023	0.015659

Fitting	25	30	35	40
XX	88.47106	86.47285	87.04951	83.37762
XY	82.73375	78.28152	77.48631	74.84161
YX	71.29643	73.16047	74.42955	75.16451
YY	87.77531	89.4061	88.01628	88.76002

Poles	25	30	35	40
XX	-3.871 + 280.950i	-4.013 + 280.434i	-4.114 + 279.517i	-4.362 + 278.450i
	-3.871 - 280.950i	-4.013 - 280.434i	-4.114 + 279.517i	-4.362 - 278.450i
XY	-4.277 + 280.789i	-4.651 + 280.266i	-5.076 + 279.401i	-5.061 + 278.537i
	-4.277 - 280.789i	-4.651 - 280.266i	-5.076 - 279.401i	-5.061 - 278.537i
YX	-5.127 + 280.021i	-4.151 + 279.633i	-3.256 + 278.920i	-3.917 + 276.850i
	-5.127 - 280.021i	-4.151 - 279.633i	-3.256 - 278.920i	-3.917 - 276.850i
YY	-4.093 + 295.766i	-4.0199 + 295.235i	-4.122 + 293.961i	-4.573 + 292.007i
	-4.093 - 295.766i	-4.0199 - 295.235i	-4.122 - 293.961i	-4.573 - 292.007i

Table 6.1: ω_n, ζ and Poles at four temperatures.

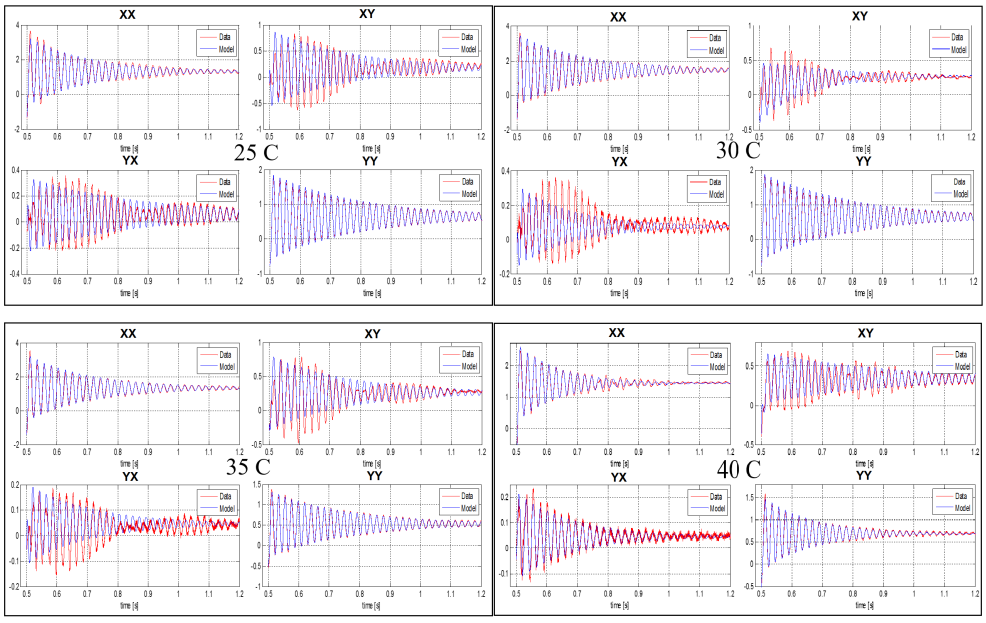

Figure 6.15: XX, XY, YX and YY modelled at 4 different temperatures.

6.3 Experimental results

6.3.1 Application of the multivariable technique on the 2-DOF piezoelectric cantilever structured actuator

This subsection shows the results obtained from applying our newly developed multivariable technique, presented in Section.5.5, on the 2-DOF piezoelectric cantilever which we discussed in Subsection.6.2.1. Applying this multivariable input shaping technique requires deriving the system poles which we can obtain from the derived system model expressed in Eq.6.5. The input matrix B was identified as per Eq.5.29, then the impulses amplitudes vector a was calculated as per Eq.5.32 by solving $a = P^{\intercal}W$. As discussed in the previous chapter, having the input matrix B information to be included in the formulation of the P matrix, ensures that the designed shaper for each input will compensate for the direct and cross couplings with each output, it also allows the designed shapers for both inputs to help each other in canceling the different modes of vibrations. The spacing between impulses is always assumed to be the same for both shapers, and its value T should be selected to have all impulse amplitudes for both shapers positive.

Fig.6.16 shows the simulation results of both, direct and cross-coupling output responses when exciting one of the inputs only.

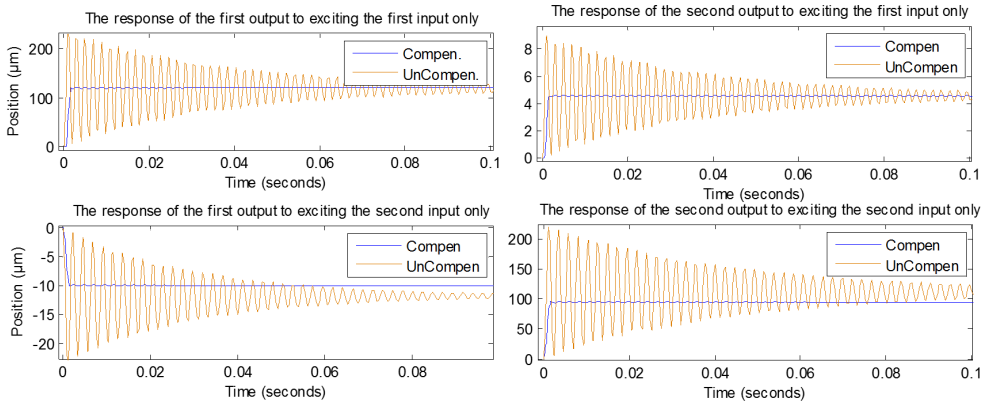

Figure 6.16: Exciting one input and showing the cross coupling effect simulation.

Fig.6.17 shows the experimental results after applying the designed compensator on the actual piezoactuator. The simulation and experimental results show that the controller was greatly successful in suppressing vibrations for both the direct and the cross-coupling outputs. The suppression in the experimental results is not as good as in the simulation results due to some modeling error.

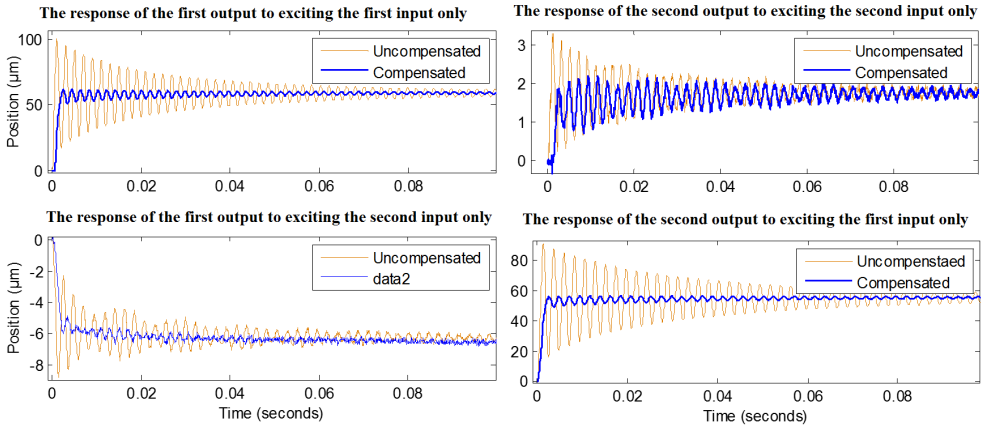

Figure 6.17: Exciting one input and showing the cross coupling effect experimental results.

To be more robust against modeling errors, the compensator performance towards having better vibrations suppression can be probably improved by increasing the number of impulses in each of the designed shapers, this will be on the expense of having more delay in the shaped inputs. Fig.6.18 and Fig.6.19 show the simulation and experimental results for the compensated and non-compensated outputs when we fully excite both inputs. Since the selected spacing time T is 1/4 of the system fundamental frequency and shapers are constituted from four impulses, the near-zero vibrations happen exactly after a complete cycle of the non-compensated response in both, the simulation and experimental results.

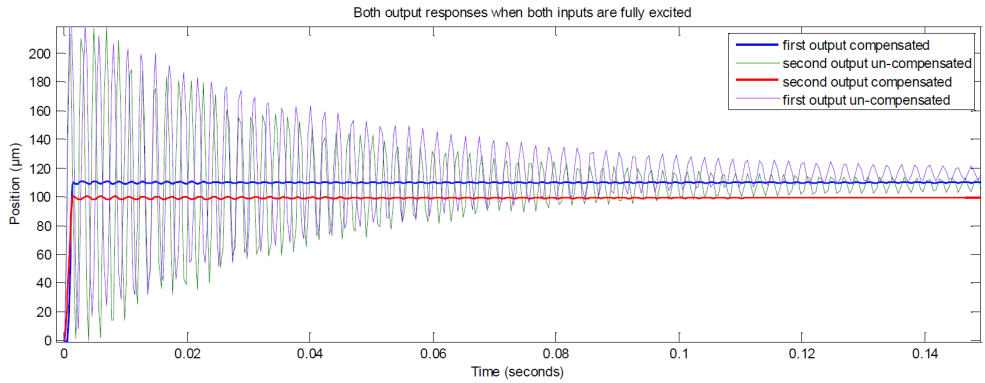

Figure 6.18: Exciting both inputs and showing both outputs, compensated and non-compensated - simulation.

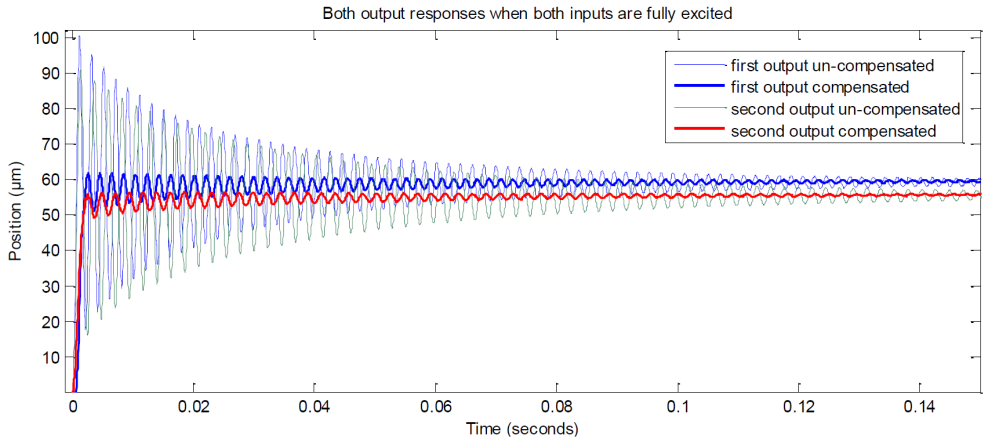

Figure 6.19: Exciting both inputs and showing both outputs, compensated and non-compensated experimental.

To examine the effectiveness of the designed controller the frequency responses of the compensated and non-compensated, direct (diagonal figures) and cross-coupling systems were plotted in Fig.6.20. These results evidence the reduction of the resonance peaks in the direct transfers and in the cross-couplings which therefore demonstrate the efficiency of our approach.

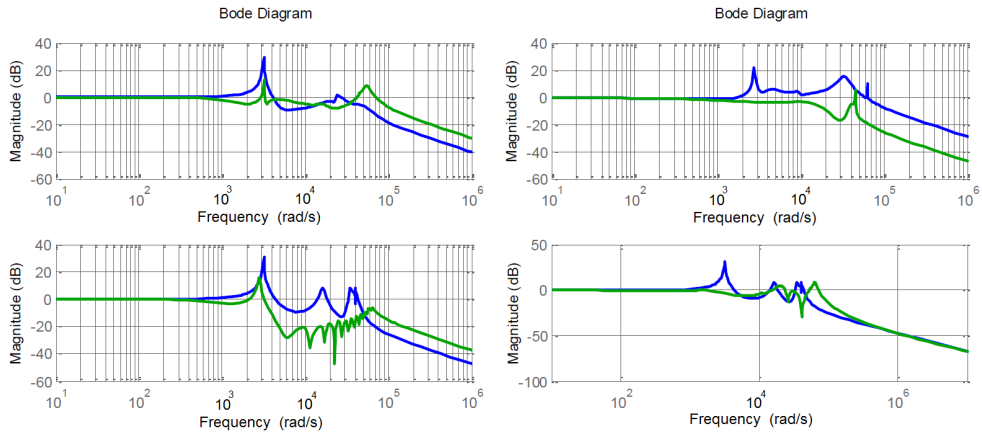

Figure 6.20: Compensated (green) and un-compensated (blue) system frequency responses.

6.3.2 Application of the multivariable technique on the 3-DOF piezotube PT230.94 actuator

The PT230.94 actuator was experimented as a 3-DOF system, hence the mandate to design 3 input shapers, one for each input. If we design all of the 3 input shapers with 4 impulses each, then impulses amplitudes vector a will be composed of 12 impulse amplitudes as per the following form:

$$a = [\ a_{00} \quad a_{10} \quad a_{20} \quad a_{30} \quad a_{01} \quad a_{11} \quad a_{21} \quad a_{31} \quad a_{02} \quad a_{12} \quad a_{22} \quad a_{32}\ ]^T \tag{6.16}$$

These amplitudes can be calculated using $a = P^{\intercal}W$ which assumes that all impulses are evenly spaced and the spacing T between them (which is the same for all shapers) has to be selected such that it is the minimum value T to make all impulse amplitudes for all shapers positive. As shown in Fig.6.21 which displays shaper impulse amplitudes versus T, if we design the shapers with 4 impulses each, then the first value to make all impulse amplitudes positive is $T = 0.00025$ second (Fig.6.21 (b)) and as a result the calculated amplitude vector is:

$$\boldsymbol{a} = [\ 0.0190 \quad 0.0055 \quad 0.0128 \quad 0.0091 \quad 0.0674 \quad 0.0938 \quad 0.0926 \quad 0.0521 \quad 0.0534 \quad 0.1060 \quad 0.0997 \quad 0.0355\ ]^T \tag{6.17}$$

Other values of T for these 4-impulse input shapers that satisfy the positive amplitudes condition are marked using square dots in Fig.6.21 (b): 0.300, 0.500, 0.550, 0.600 and 0.650 mSec. For comparison purposes that will be discussed later in this section, we also calculated vector a amplitudes when the shapers are designed with 3 impulses. As shown in Fig.6.21 (a), the first T to make all impulse amplitudes positive is $T = 0.0005$ second. For this T, the resultant impulse amplitudes vector is:

$$\boldsymbol{a} = [\ 0.0317 \quad 0.0480 \quad 0.0205 \quad 0.2298 \quad 0.3497 \quad 0.1917 \quad 0.1536 \quad 0.0387 \quad 0.1477\ ]^T \tag{6.18}$$

Other values of T to satisfy the positive amplitudes condition for the 3-impulse shapers are marked using square dots in Fig.6.21 (a): 0.500, 0.550 and 0.600 mSec. Once the vector a values are calculated, they can be plugged to the compensator design in SIMULINK to carry out the simulation. Fig.6.22 shows simulated uncompensated and compensated responses when shapers were designed with 3 and 4 impulses. Each column in the figure shows one direct transfer and two cross couplings when exciting only one of the inputs. This simulation results show that the proposed MIMO controller was greatly successful in reducing vibrations and bringing them close to zero in both the direct and the cross-couplings for all outputs. However it was not successful to get zero steady state error which is beyond the scope

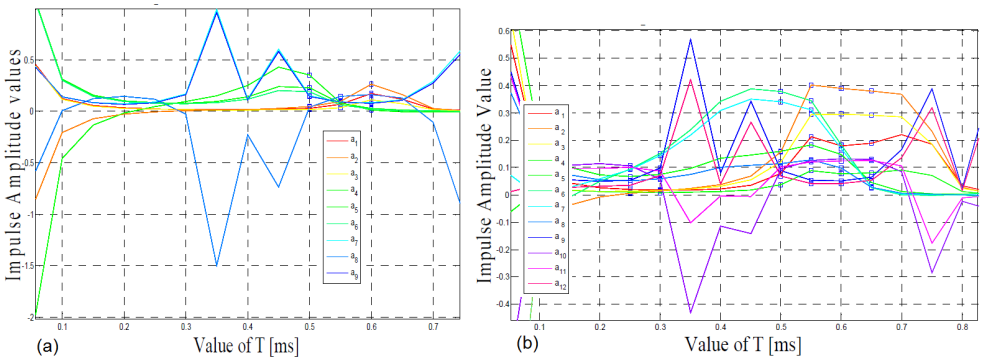

Figure 6.21: Shapers impulse amplitudes versus T for (a) 3-impulses and (b) 4-impulses.

	When Exciting X Only	When Exciting Y Only	When Exciting Z Only
Un-comp. / 3-imp. / 4-imp. (X)	12.68 / 09.25 / 04.45	35.00 / 21.53 / 18.85	11.20 / 04.39 / 02.75
Un-comp. / 3-imp. / 4-imp. (Y)	19.13 / 09.92 / 06.57	17.00 / 09.00 / 04.00	08.00 / 05.00 / 04.00
Un-comp. / 3-imp. / 4-imp. (Z)	10.00 / 02.00 / 07.00	30.00 / 24.00 / 13.00	30.00 / 02.50 / 08.00

Table 6.2: Settling time for all response.

of this study. It is also worth mentioning that having steady state error could be beneficial to reducing the level of cross couplings between inputs and outputs. Additionally, the 4 impulses shapers did a better job than the 3 impulses shapers in removing more modes of vibrations which can be attributed to the fact that the more the number of impulses is for a shaper, the more it becomes robust against model uncertainties and the more it is effective in suppressing multi modes of vibrations. Having T=0.25 mSec for the 4-impulses shapers which is half of T=0.5 mSec for the 3-impulses shapers contributed to a shorter delay in the responses of the 4-impulse shapers although they have more impulses. Additionally 4-impulses shapers showed improved settling time over 3-impulses shapers as shown in Table.6.2.

A closer look at the simulated 3 and 4 impulse shaper responses in Fig.6.22 show clearly that 4-impulses shaper responses have less delay and better vibrations suppression in both direct and cross couplings than the 3-impulse shaper. The vibrations suppression accomplished by the compensator can be also looked at in the frequency domain by plotting bode diagram for all couplings as shown in Fig.6.23. The figure shows clearly the difference in peaks (modes of vibration) between the blue trace which represents the original system before compensation and the red trace which represents the compensated system after augmenting the multivariable input shapers.

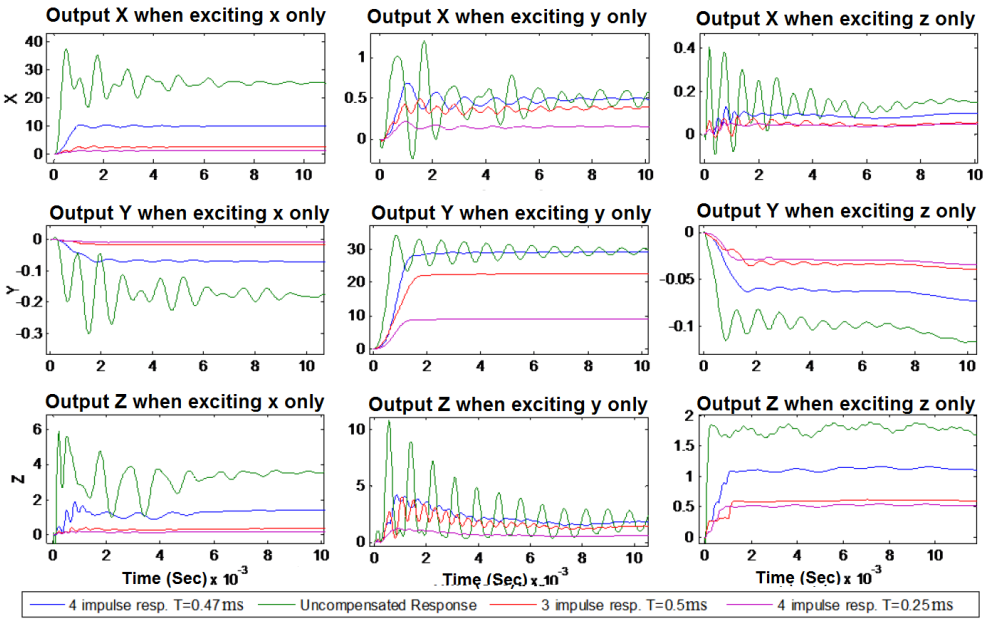

Figure 6.22: Shapers impulse amplitudes versus T for 3-impulses and 4-impulses.

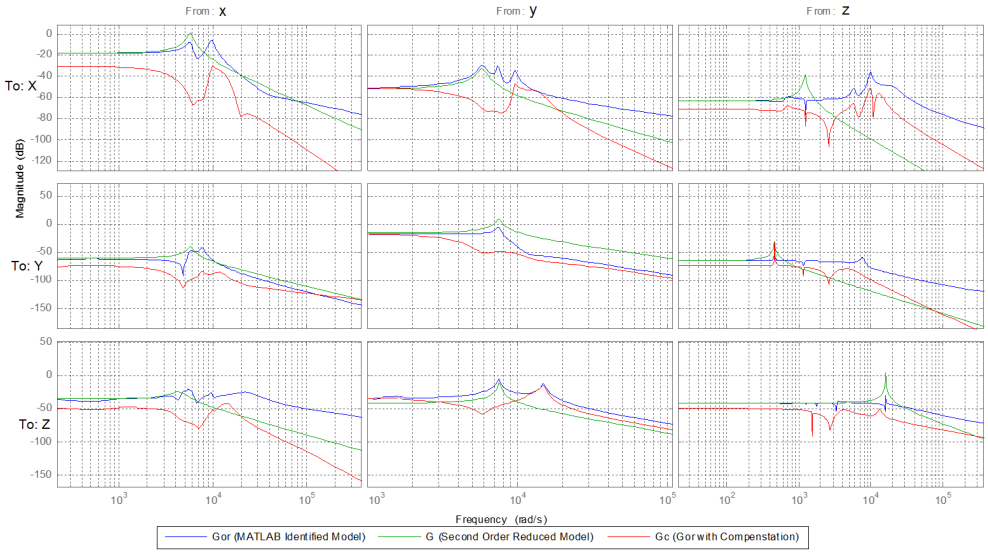

Figure 6.23: Bode plots for the identified, reduced and compensated models - simulation.

Fig.6.24 shows the results from applying the designed 4-impulses shapers on the 3-DOF piezoelectric actuator. First, a step input was applied to excite the x-axis while leaving the excitation of inputs along y and z axes to zero.

Fig.6.24 (a) shows the x-displacement response to a step input, which corresponds to the direct transfer along the x-axis. The displacements along the y and z axes when we excited only the x-axis are shown in Fig.6.24 (d) (for the y axis) and Fig.6.24 (g) (for the z axis). These two last responses correspond to the cross-couplings. The same procedure was applied for the y excitation (by letting the x and the z excitations zero) and for the z excitation (by letting the x and the y excitations zero). Fig.6.24 (e) and Fig.6.24 (i) represent the direct transfers along the y and the z axes respectively.

The remaining curves are the cross-couplings. The uncompensated responses are also pictured in the same figures. These figures clearly demonstrate that badly damped oscillations of the actuator are strongly reduced when applying the proposed compensator, both for the direct transfers and for the cross-couplings. As predicted by the simulation, the overshoots which reached 400% (see Fig.6.24 (h)) was completely removed.

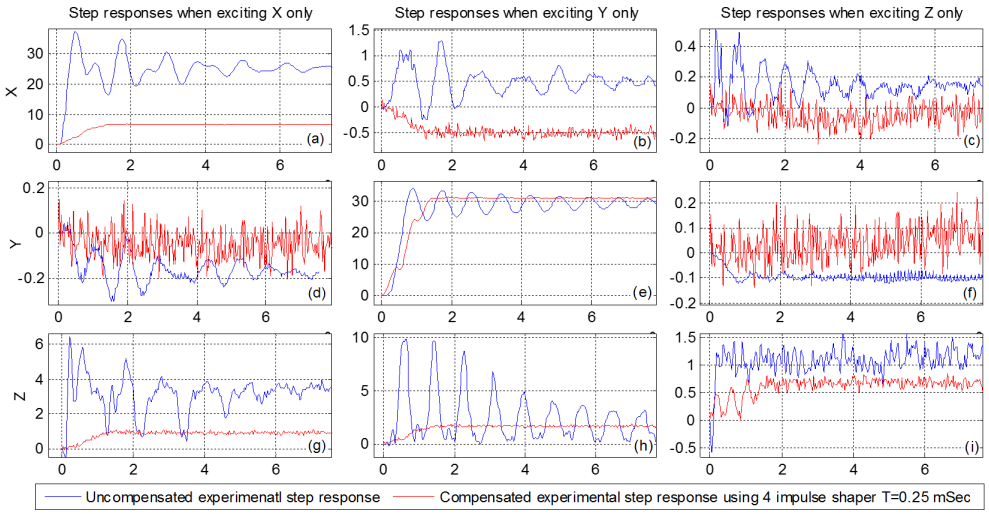

Figure 6.24: Step responses for the uncompensated and 4-impulse compensated responses experimental.

6.3.3 Application of the multivariable technique on the 3-DOF piezotube TB6309 actuator

For simplicity and since the focus in this experimental work is on studying robustness against temperature fluctuations, we deal with this piezoelectric tube as 2-input 2-output system with two modes of vibrations. The compensator $\boldsymbol{P}$ matrix can be formed using Eq.5.32, where $[(\omega_1, \zeta_1),\ (\omega_2, \zeta_2)]$ and $[(\omega_3, \zeta_3),\ (\omega_4, \zeta_4)]$ to be the structural frequencies and damping ratios for the first and second output respectively. $s_{1,2} = -\zeta_{1,2}\omega_{1,2} \mp j\omega_{d\ 1,2}$ are

system poles for the first output and $s_{3,4} = -\zeta_{3,4}\omega_{3,4} \mp j\omega_{d\ 3,4}$ are system poles for the second output. All of these parameters were derived from the system model at different four temperatures and are listed in Table.6.1. Impulse locations for each input shaper will be at $\begin{bmatrix} 0 & T & 2\times T \end{bmatrix}$, and Impulse amplitudes a can be solved using the following generalized inverse:
$a = P^{\intercal}W$
where $W = \begin{bmatrix} 0_{8\times1} \\ 1_{2\times1} \end{bmatrix}$ represents the zero and unity constraint equations, and $a = \begin{bmatrix} a_{00} & a_{10} & a_{20} & a_{01} & a_{11} & a_{21} \end{bmatrix}^T$ is composed of three impulses for each shaper. The impulse spacing T has been selected such that it is the minimum value to make all impulse amplitudes for all shapers positive.

Fig.6.25 displays shaper impulse amplitudes versus impulse spacing T at 25 C. For this designed two 3-impulses input shapers, the first value to make all impulse amplitudes positive is $T = 0.00625$ second and as a result the calculated amplitude vector is:
$a = \begin{bmatrix} 0.393 & 0.464 & 0.141 & 0.096 & 0.0169 & 0.019 \end{bmatrix}^T$

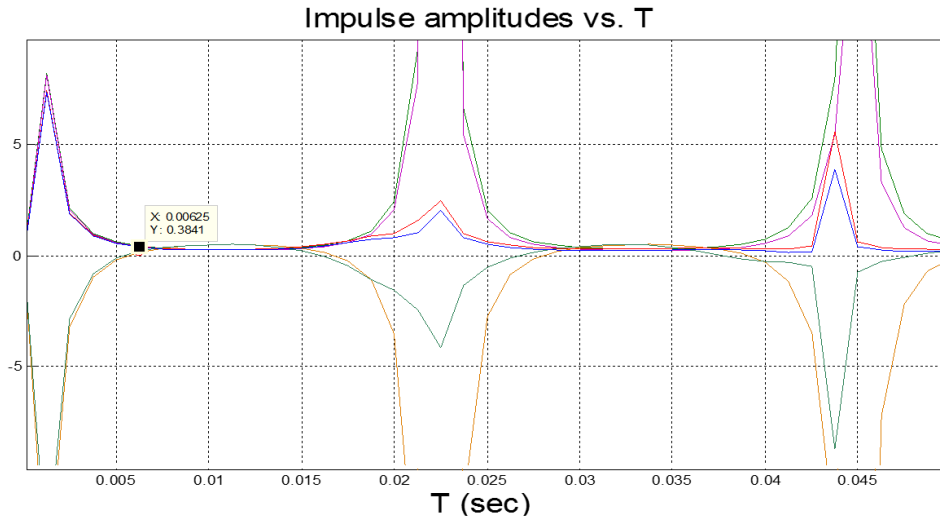

Figure 6.25: Impulse amplitudes as a function to impulse spacing at **25 C**.

The same procedure can be used to calculate shapers impulse amplitudes and spacing at 30, 35 and 40 degrees Celsius. Matrix p at each temperature can be evaluated using system parameters in Table.6.1, and B matrix coefficients derived at that specific temperature. Table.6.3 shows the resultant input shapers parameters at the four temperatures. It is obvious in this table that these parameters are almost identical for the four different selected temperatures, which justifies the controller robust performance shown in the subsequent sections, in both simulation and experimental results.
To simulate the compensated piezotube responses in both direct and cross

couplings, each of the four previously designed input shapers shown in Table.6.3 needs to be augmented separately to the system model. Different configurations can be tested in this context, either to fix the compensator and test its performance with different system models at different temperatures, or to fix the system model at a specific temperature and try it with different compensators designed at different temperatures. Each compensator can be also simulated with the system model which was obtained at the same temperature at which the compensator was derived. Fig.6.26 shows the uncompensated and compensated XX and YY at 35 degrees Celsius when the controller is derived at 35 C. Fig.6.27 shows the direct couplings XX and YY simulated compensated-responses at different temperatures.

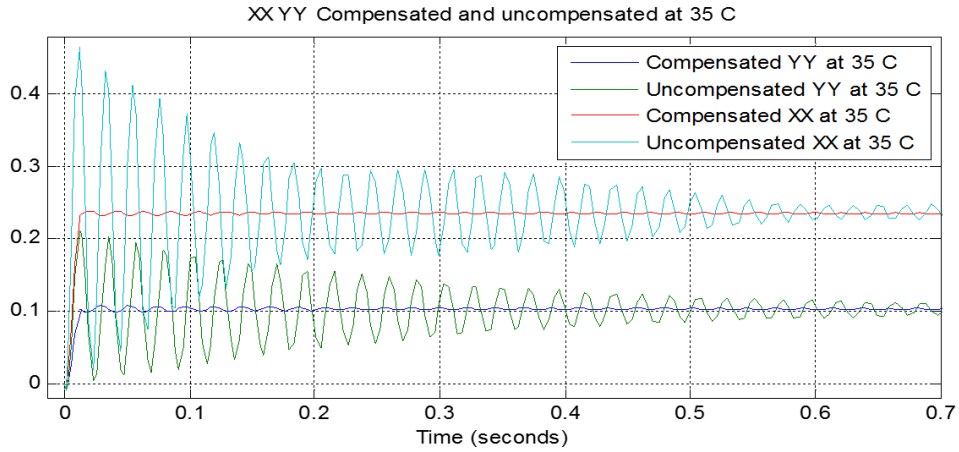

Figure 6.26: XX and YY responses with controller derived at **35 C** (Simulation).

The simulation shows that the designed input shapers performed exactly the same way even when the temperature was changed.

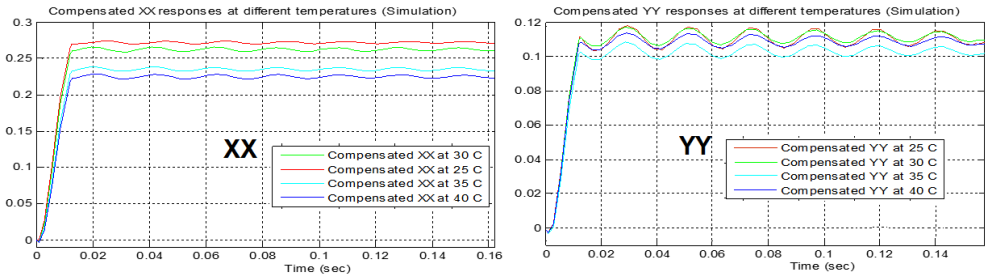

Figure 6.27: XX and YY Compensated responses at different temperatures (Simulation).

25	1st shaper impulse amplitudes	a_{00} a_{10} a_{20}	0.5072	0.0084	0.4842
	2nd shaper impulse amplitudes	a_{01} a_{11} a_{21}	0.4703	0.0707	0.4489
	Impulses time locations	T	0	0.0056	0.0113
30	1st shaper impulse amplitudes	a_{00} a_{10} a_{20}	0.5084	0.0057	0.4858
	2nd shaper impulse amplitudes	a_{01} a_{11} a_{21}	0.4716	0.0681	0.4501
	Impulses time locations	T	0	0.0056	0.0113
35	1st shaper impulse amplitudes	a_{00} a_{10} a_{20}	0.5106	0.0008	0.4885
	2nd shaper impulse amplitudes	a_{01} a_{11} a_{21}	0.4752	0.0623	0.4526
	Impulses time locations	T	0	0.0056	0.0113
40	1st shaper impulse amplitudes	a_{00} a_{10} a_{20}	0.498	0.0277	0.4741
	2nd shaper impulse amplitudes	a_{01} a_{11} a_{21}	0.4657	0.0847	0.4413
	Impulses time locations	T	0	0.0057	0.0115

Table 6.3: Controller parameters at four temperatures.

The experimental compensated responses of the direst and cross couplings at different temperatures when the controller is derived at 25, 30, 35 and 40 degrees are shown in Fig.6.28, Fig.6.29, Fig.6.30 and Fig.6.31 respectively. For example, in Fig.6.30, the controller was derived at 35 degrees Celsius and responses for XX, XY, YX and YY were plotted at different temperature of the piezoelectric tube. The same applies to Fig.6.31, except that the controller was derived from the data collected at 40 degrees Celsius.

All controllers performed the same way within the temperature range of study (25-40 C), and all responses (no matter the data from which the controller was derived or the temperature of the tube at which the experiment was conducted) look exactly the same. The difference in the final value of the compensated response can be neglected in this context since vibrations suppression is the focus in this work. Fig.6.32, Fig.6.33 and Fig.6.34 show different compensated responses when testing different controllers that were derived at different temperatures. Fig.6.32 for example, shows experimental compensated-responses for direct and cross couplings, when tested with different controllers designed with parameters derived at different temperatures and when the tube temperature is at 35 degrees Celsius. In other words, when the piezotube actuator operates at 25 C and we design the compensator using parameters that were derived from the tube model at different temperature, this deviation in system parameters (error) doesn't affect the performance of the compensator when it comes to vibrations reduction. However, the final value of the tube position does affected though, and this can be fixed by other techniques which are beyond the scope of this study.

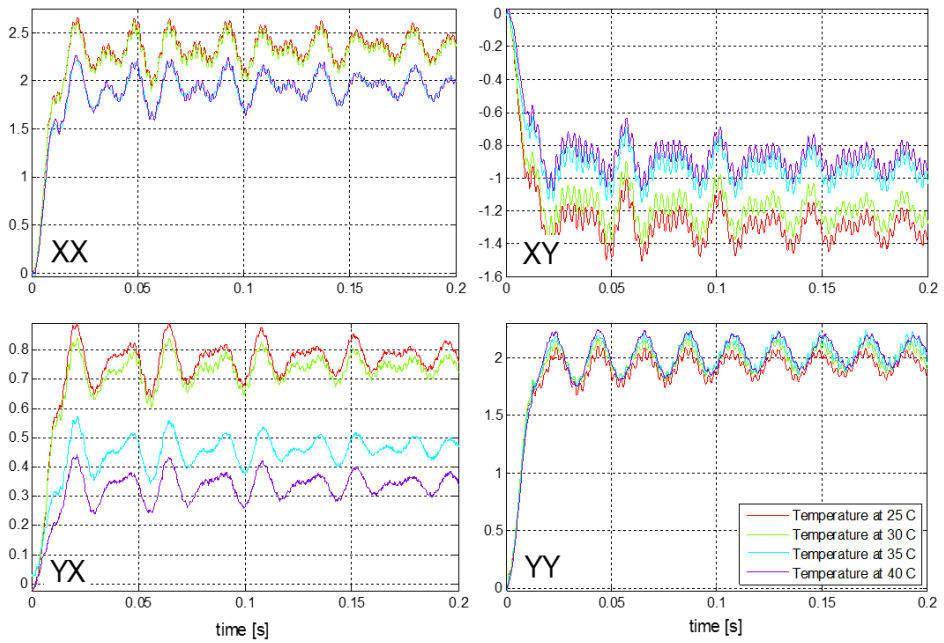

Figure 6.28: XX, XY, YX and YY responses at different temperatures with controller designed at **25 C** (Experimental).

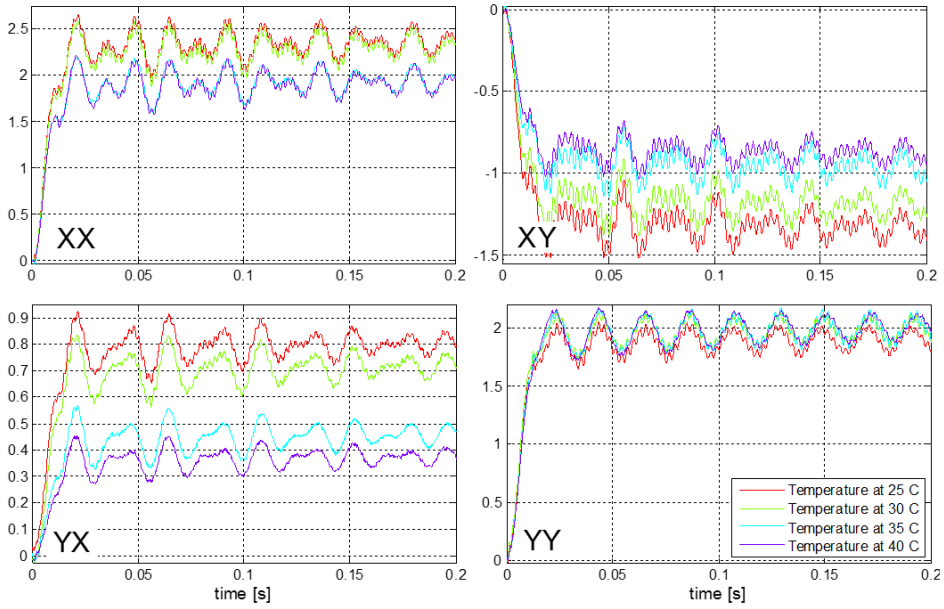

Figure 6.29: XX, XY, YX and YY responses at different temperatures with controller designed at **30 C** (Experimental).

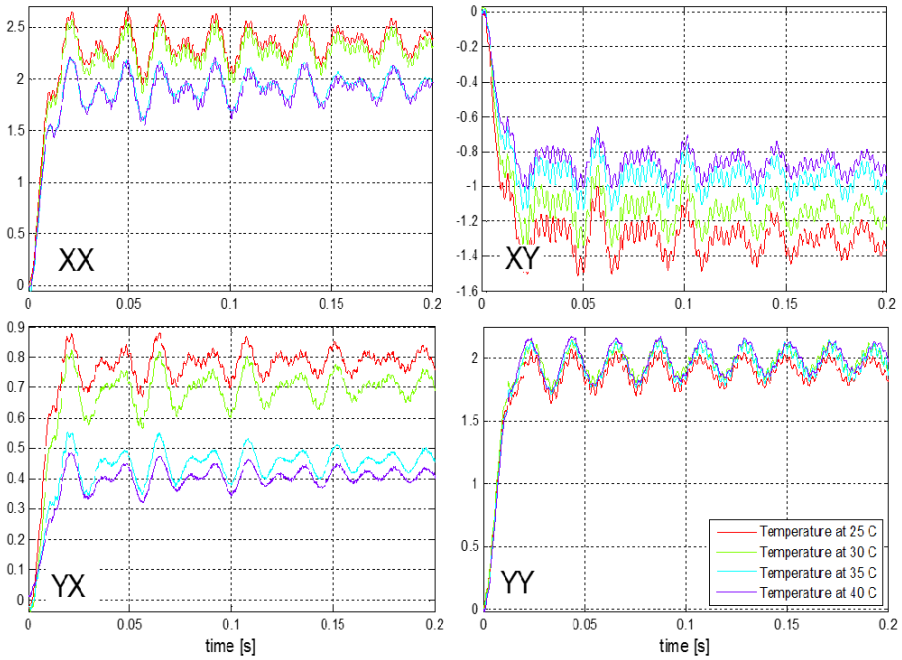

Figure 6.30: XX, XY, YX and YY responses at different temperatures with controller designed at **35 C** (Experimental).

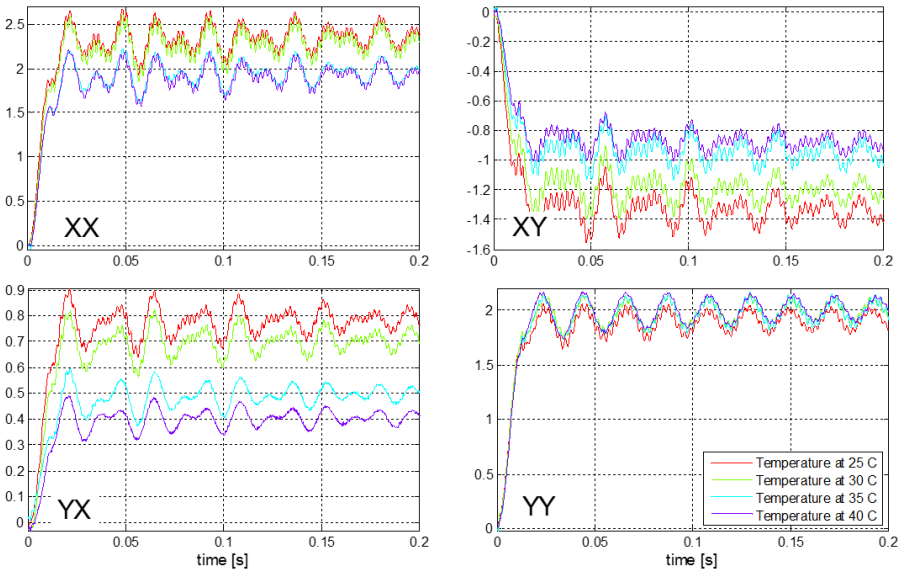

Figure 6.31: XX, XY, YX and YY responses at different temperatures with controller designed at **40 C** (Experimental).

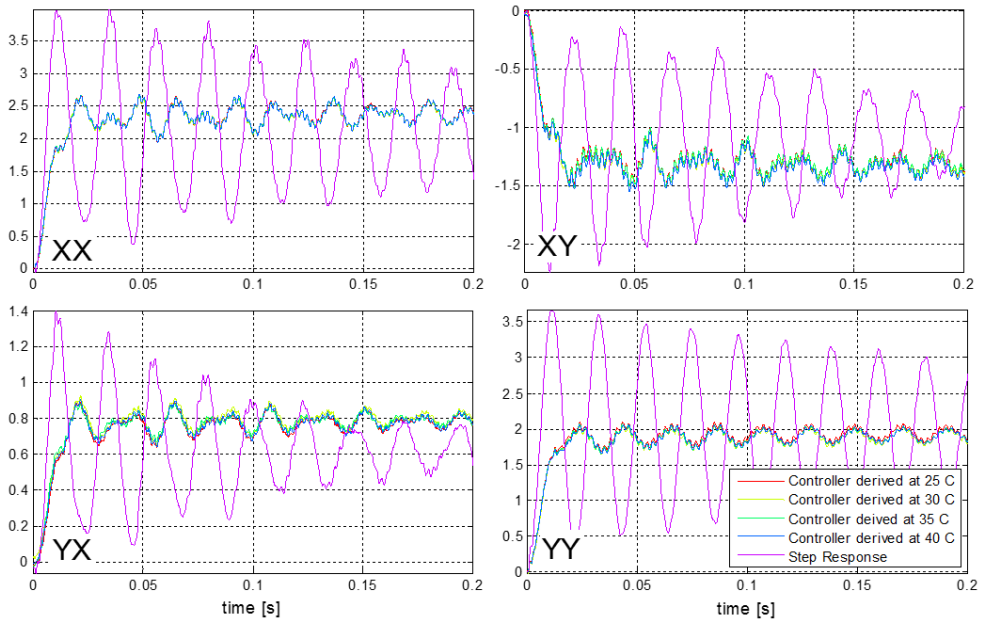

Figure 6.32: XX, XY, YX and YY responses at 25 C with controller designed at different temperatures (Experimental).

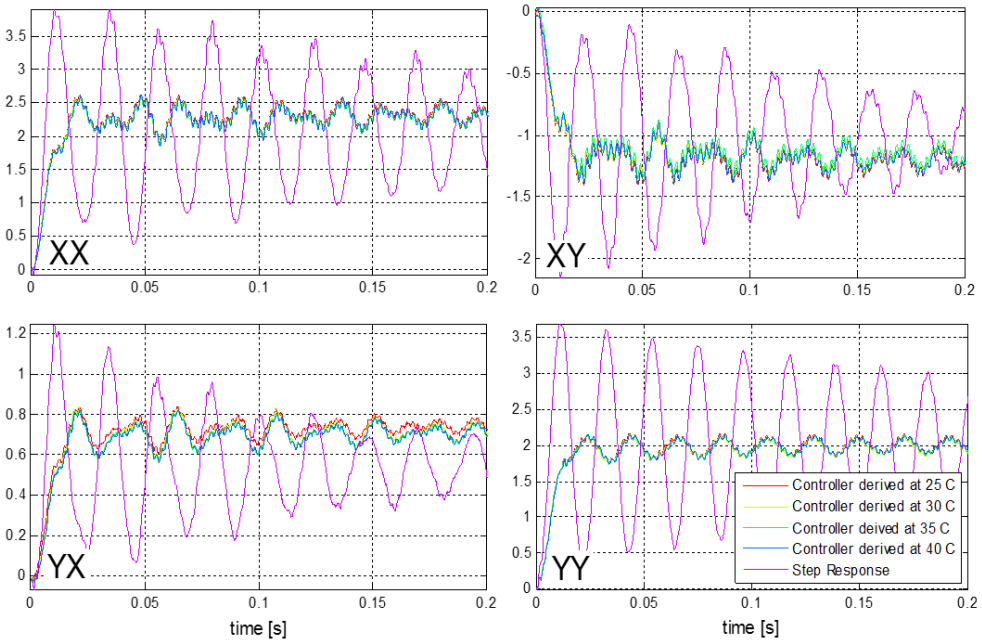

Figure 6.33: XX, XY, YX and YY responses at 30 C with controller designed at different temperatures (Experimental).

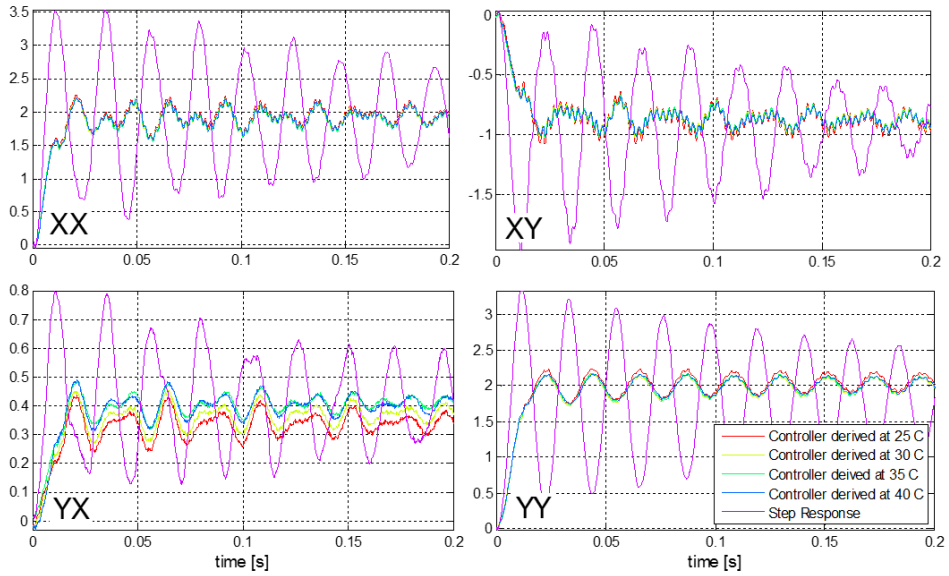

Figure 6.34: XX, XY, YX and YY responses at 40 C with controller designed at different temperatures (Experimental).

In Summary, all figures in both configurations show the robustness of the technique against temperature fluctuations, which in turn means the robustness against uncertainties in the changes in tube structural frequencies and damping ratios caused by these fluctuations.

6.4 Feedforward-feedback control

In Subsection.6.3.1 we presented the experimental results of implementing our newly developed multivariable input shaping technique on the 2DOF piezoelectric cantilever. Fig.6.35 reminds about the detailed scheme of the shaper which is composed of two sub-shapers for the two input voltages u_1 and u_2. In the figure, u_{s1} and u_{s2} are the shaped input voltages that will be applied to the piezoelectric cantilever. Fig.6.35-c shows the simulated step responses with and without the calculated compensator. They clearly show the substantial damping of the vibrations when the compensator is implemented.

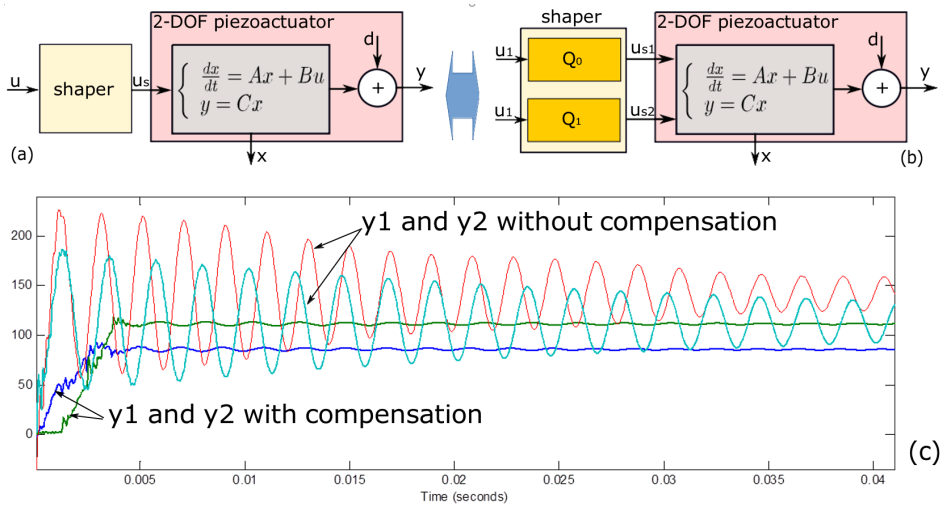

Figure 6.35: (a) The system with the vibrations compensator (shaper). (b) the detailed shaper. (c) simulation results.

If we augment the feedforward compensated system shown in Fig.6.35 by a feedback controller, then the resultant system has a new dynamic as well as a new static parts relative to the initial model in Fig.6.4. Since the output disturbance d(s) which encloses the hysteresis and the creep nonlinearities is a low frequency signal, and since the piezoactuator dynamics has a high frequency characteristics, it is possible to move d(s) at the input (input disturbance) where it is still dominant. In order to maintain the generalization, let us name this input disturbance b(s), instead of d(s). Therefore Fig.6.36 depicts the equivalence of Fig.6.35 when translating the output disturbance at the input. Also, the new model becomes:

$$\sum_{ff} : \begin{cases} \frac{dx(t)}{dt} = A_{ff}x(t) + B_{ff}u(t) + B_{ff}b(t) \\ y(t) = C_{ff}x(t) \end{cases} \tag{6.19}$$

where A_{ff} , B_{ff} and $_{ff}$ are the new state, input and output matrices respectively which are based on A, B and C and on the shaper.

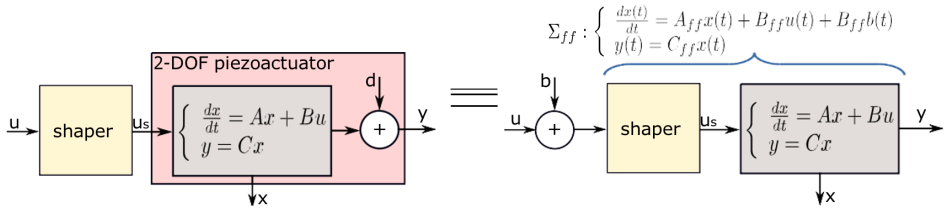

Figure 6.36: Translating the output diturbance d at the input.

In order to further study an output feedback controller, we suggest first to remove the input disturbance b from the feedback. For that a disturbance observer (DOB) is first proposed. The estimate $b(s)$ is afterwards used as a negative feedback such that we have $u+b-\hat{b} = u$ as input of the shaper, see Fig.6.37-a. In this case, the system to be controlled by the output feedback controller is without the disturbance b. The DOB is based on the technique proposed in [154] where $F(s)$ is a filter conveniently chosen for robustness and $\sum_{ff}$ should be identified in a such a way it is minimum phase.

We now use the system with the shaper and with the DOB to construct and to synthesize the output feedback controller. The controller is composed of the output feedback gain K and the prefilter L, see Fig.6.37-b. Remember that the reason why we removed the disturbance b, thanks to the DOB, was to automatically reject this disturbance in the closed-loop. In other word, to obtain $y = y_r$ in steady-state regime whatever b is, where y_r is the reference input. Without this DOB, and thus without removing $b(s)$, there would have been a statical error with this output feedback controller to be designed.
From the model in (Eq.6.19) and the block-diagram in Fig.6.37-b, with consideration of the DOB effect, we have the following governing equations:

$$\begin{cases} \frac{dx}{dt} = A_{ff}x + B_{ff}u \\ y = C_{ff}x \\ u = Ly_r - Ky \end{cases} \tag{6.20}$$

which, after rearrangement, implies the model of the closed-loop:

$$\begin{cases} \frac{dx}{dt} = (A_{ff} - B_{ff}KC_{ff})x + B_{ff}Ly_r \\ y = C_{ff}x \end{cases} \tag{6.21}$$

Thus, K can be designed to impose the dynamics of the closed-loop which is defined by the state matrix $(A_{ff} - B_{ff}KC_{ff})$. For that we use the linear quadratic regulator principle (LQR). Consider the following (quadratic)

performance index:

$$J = \int_0^\infty (y^T Q_y y + u^T R u) dt \tag{6.22}$$

where Q_y and R are diagonal and positive semi-definite matrices that weight the elements of y and u respectively according to their importance in the control problem. The two matrices can also be used to weight in a global manner the input relative to the output or conversely. The objective is to find the feedback gain K such that the cost J is minimized, i.e. the output transient part energy and the input energy are minimized. Introducing $y^T = x^T C^T$ and $y = Cx$ in (Eq.6.22), the problem becomes in finding K such that the following J is minimized:

$$J = \int_0^\infty (x^T Q x + u^T R u) dt \tag{6.23}$$

where $Q = C^T Q_y C$ is diagonal and positive semi-definite.

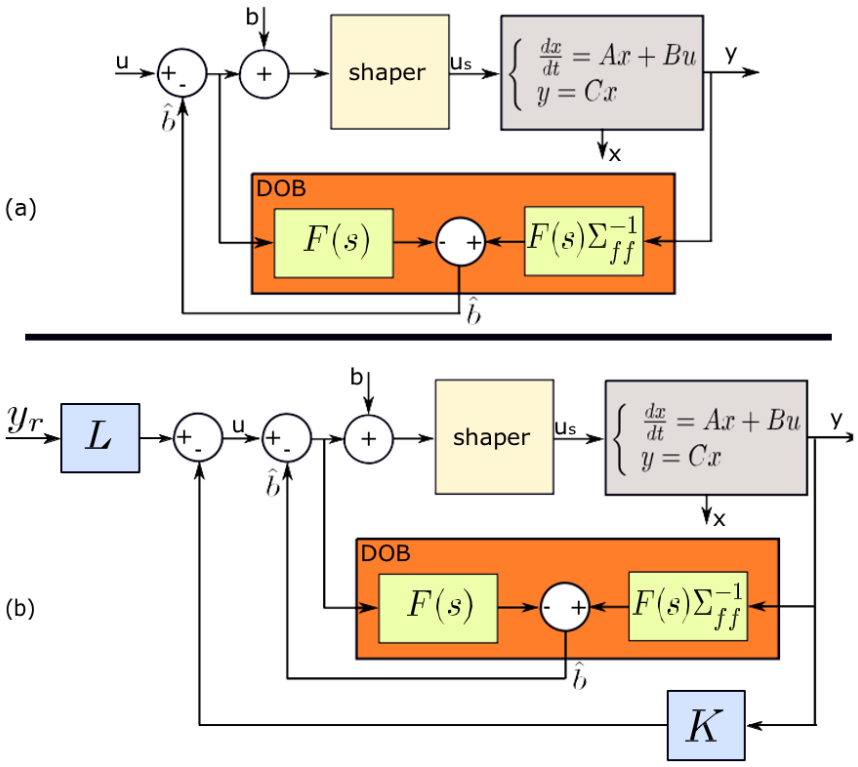

Figure 6.37: (a) Introduction of a DOB to remove the input disturbance $b(s)$. (b) an output feedback control scheme.

Solving the LQR problem for output feedback architecture is not as direct as that of LQR problem in state-feedback architecture. The optimal gain design K is derived as per the equations in [155]. To obtain the prefilter L, the steady-state regime is first calculated. For that, we let $\frac{dx(t)}{dt} = 0$ in (Eq.6.21). We have:

$$y = C_{ff}(B_{ff}KC_{ff} - A_{ff})^{-1}B_{ff}Ly_r \tag{6.24}$$

To make $y = y_r$ at the steady-state regime, from (Eq.6.24), one should have:

$$C_{ff}(B_{ff}KC_{ff} - A_{ff})^{-1}B_{ff}L = I \Leftrightarrow L = (C_{ff}(B_{ff}KC_{ff} - A_{ff})^{-1}B_{ff})^{-1} \tag{6.25}$$

To implement the calculated controller first we apply a step reference input $y_{1r} = 60\mu s$ along y_1 axis. Then, later, we apply a step reference input $y_{2r} = 60\mu s$ along y_2 axis. Fig.6.38-a depicts the response of y_1 relative to these step inputs, while Fig.6.38-b is the response of y_2. As we can see, the output y_1 directly reaches the reference y_{1r} (at about 2.4s) and the statical error is always maintained zero afterwards. The application of the reference y_{2r} at about 5.45s provokes a slight disturbance (cross-coupling) to y_1 but this is quickly rejected. The same performance is also found for y_2: the disturbance (cross-coupling) due to the application of the step y_{1r} at about 2.4s is quickly rejected, and the output y_2 quickly reaches the reference y_{2r} at about 5.45s. These results also show that the statical error is maintained negligible which show the efficiency of the DOB to remove low frequency (internal) disturbance effect. Without this DOB and disturbance rejection, the hysteresis and the creep would have affected the statical error.

The previous results have been zoomed and are shown in Fig.6.39. Fig.6.39-a shows the step response of y_1 and Fig.6.39-d shows the step response of y_2. The settling time is less than 20ms for both. They also show the strongly damped oscillations relative to the responses of the initial system (see Fig.6.3). This is due to the input shaping technique augmented by the feedback controller. Without the input shaping technique, it would have been difficult to find the feedback controller able to reduce the oscillations with simultaneously such settling time. Notice that the settling time of the initial system (see Fig.6.3) was about 100ms. Finally Fig.6.39-b and Fig.6.39-c shows the cross-couplings rejections which are very quick thanks to the feedback controller.

In summary, this section dealt with the control of a 2-DOF oscillating and nonlinear piezoactuator. First the linear model with fictive disturbance that accounts for the nonlinearities and the cross-couplings is expressed. Then, a feedforward controller based on a MIMO input shaping technique was applied to the actuator in order to damp the vibrations. The calculation of

the shaper (vibrations compensator) is based on the model expressed. In order to remove the fictive distortion, we afterwards implemented a disturbance observer and an input disturbance compensation. Finally, an output feedback controller based on a feedback gain and a prefilter is calculated and implemented. The experiments show the efficiency of the whole architecture to damp the vibrations, to reject the effect of the nonlinearities in the precision of the actuator and to have a convenient tracking rapidity.

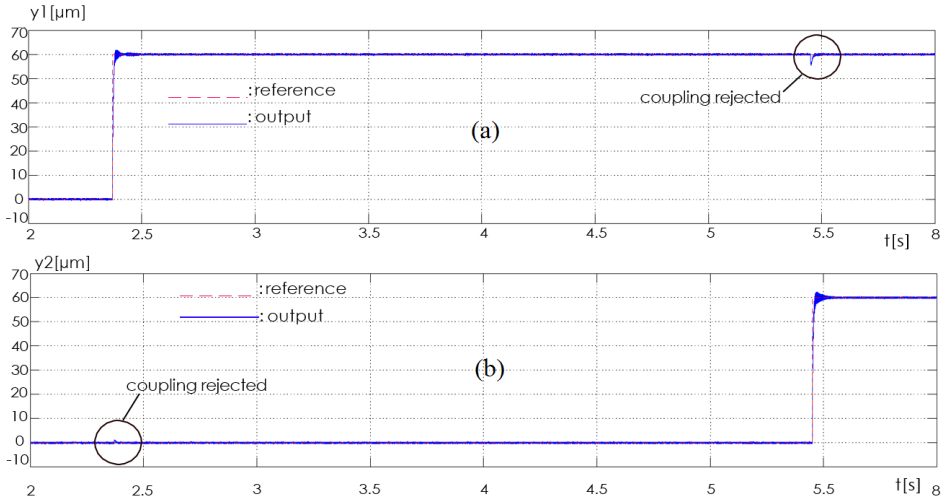

Figure 6.38: (a) Step response along $y1$ axis. (b) step response along $y2$ axis.

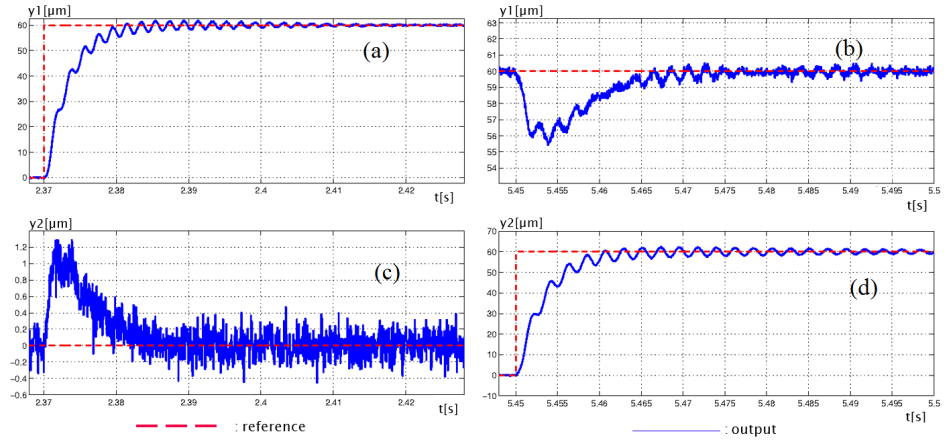

Figure 6.39: Zoom of the different step responses.

6.5 Conclusions

This chapter presented 3 different experimental setups, one cantilever structured actuator and two piezotube actuators of different specifications, all of them were modeled using MATLAB ident toolkit. The vibrations reduction effectiveness of the newly developed multivariable input shaping technique were examined on all of these actuators as a 2DOF or 3DOF systems. It was shown that the design of compensators using this multivariable technique is an easy and straightforward process. However, increasing the number of impulses for shapers to have more than 4 impulses made it very challenging when it comes to figuring out the proper and small T value that would make all shaper impulse amplitudes positive. This can be considered as a limitation for this approach, especially when having more than 4 impulses is required to improve the compensator robustness. The simulation and experimental results demonstrated the technique efficiency, permitting to completely remove overshoots of the actuators' initial response. The results showed also that the newly developed mutivariable technique is very promising for systems where using sensors is difficult and impossible. Finally the technique robustness was tested against temperature fluctuations. The modelling of the piezoelectric tube at different temperatures have shown that the tube dynamics change with the variation of the temperature. However, the simulation and experimental results prove the efficacy of the proposed technique in suppressing vibrations without being affected by temperature variation. This technique allowed to suppress vibrations on the X and Y directions and was proved to be effective in the cross couplings as well. In our future works, we will try to improve the robustness of this technique by adding more constraints in the formulation of the proposed technique. Also the effect of number of shaper impulses on the robustness will be investigated.

List of Figures

List of Tables

+-

Bibliographic references

[1] Bristeau, Pierre-Jean, et al. "The navigation and control technology inside the ar. drone micro uav." IFAC Proceedings Volumes 44.1 (2011)

[2] A.Ferreira, J. Agnus, N. Chaillet and J. M. Breguet, "A smart microrobot on chip: design, identification, and control," in IEEE/ASME Transactions on Mechatronics, vol. 9, no. 3, pp. 508-519, Sept. 2004.

[3] B. Aerotech. "Small Step Size Is Key to Big Science." Aerotech InMotion Blog. N.p., 12 Oct. 2012. Web. 20 Feb. 2017.

[4] "Piezoelectric Devices Market by Material, Product and Application - Global Forecast to 2022." Research and Market , Jan. 2017. Web.

[5] Heidemann, John, et al. "Research challenges and applications for underwater sensor networking." Wireless Communications and Networking Conference, 2006. WCNC 2006. IEEE. Vol. 1. IEEE, 2006.

[6] Shrout, Thomas R., et al. "High performance, high temperature perovskite piezoelectrics." Applications of Ferroelectrics, 2004. ISAF-04. 2004 14th IEEE International Symposium on. IEEE, 2004.

[7] Guo, R., et al. "Origin of the high piezoelectric response in PbZr 1 x Ti x O 3." Physical Review Letters 84.23 (2000): 5423.

[8] Moheimani, SO Reza, and Andrew J. Fleming. Piezoelectric transducers for vibration control and damping. Springer Science and Business Media, 2006.

[9] Rakotondrabe, Micky, and M. Janaideh. Smart materials-based actuators at the micro/nano-scale. Springer, 2013.

[10] D. Habineza, M. Rakotondrabe and Y. Le Gorrec, 'Characterization, Modeling and H-inf Control of n-DOF Piezoelectric Actuators: Application to a 3-DOF Precise Positioner', Asian Journal of Control, DOI=10.1002/asjc.1224, Vol. 18, No. 5, pp. 1-20, September 2016.

[11] M. Rakotondrabe, Y. Haddab and P. Lutz, 'Plurilinear modeling and discrete -synthesis control of a hysteretic and creeped unimorph piezoelectric cantilever', IEEE International Conference on Automation, Robotics, Control and Vision, pp:57-64, Grand Hyatt Singapour, December 2006.

[12] M. Rakotondrabe, Y. Haddab and P. Lutz, 'Quadrilateral modelling and robust control of a nonlinear piezoelectric cantilever', IEEE Transactions on Control Systems Technology, 17(3), pp:528-539, May 2009.

[13] M. Al Janaideh, M. Rakotondrabe and O. Al Janaideh, Further Results on Hysteresis Compensation of Smart Micro-Positioning Systems with the Inverse Prandtl-Ishlinskii Compensator, IEEE Transactions on Control Systems Technology, doi:10.1109/TCST.2015.2446959, 2016.

[14] Mayergoyz, Isaak D. Handbook of giant magnetostrictive materials. Ed. Gran Engdahl. Elsevier, 1999.

[15] Otsuka, Kazuhiro, and Clarence Marvin Wayman. Shape memory materials. Cambridge university press, 1999.

[16] Duerig, Thomas W., K. N. Melton, and D. Stckel. Engineering aspects of shape memory alloys. Butterworth-Heinemann, 2013.

[17] Wu, Ming H., and L. M. Schetky. "Industrial applications for shape memory alloys." Proceedings of the international conference on shape memory and superelastic technologies. 2000.

[18] APC. "The Top Uses of Piezoelectricity in Everyday Applications." APC International Ltd. APC, 13 Feb. 2015. Web. 30 Jan. 2017.

[19] Held, K. J., and J. D. Barry. "Precision pointing and tracking between satellite-borne optical systems." Optical Engineering 27.4 (1988): 274325-274325.

[20] Giurgiutiu, Victor. "Review of smart-materials actuation solutions for aeroelastic and vibration control." Journal of Intelligent Material Systems and Structures 11.7 (2000): 525-544.

[21] Binnig, Gerd, Calvin F. Quate, and Ch Gerber. "Atomic force microscope." Physical review letters 56.9 (1986): 930.

[22] Binnig, Gerd, and Heinrich Rohrer. "Scanning tunneling microscopy." Surface science 126.1-3 (1983): 236-244.

[23] Stroscio, Joseph A., and William J. Kaiser. Scanning tunneling microscopy. Vol. 27. Academic Press, 1993.

[24] Bottomley, Lawrence A. "Scanning probe microscopy." Analytical chemistry 70.12 (1998): 425-476.

[25] Kamila, Susmita. "Introduction, classification and applications of smart materials: an overview." American Journal of Applied Sciences 10.8 (2013): 876.

[26] Cao, Wenwu, Harley H. Cudney, and Rainer Waser. "Smart materials and structures." Proceedings of the National Academy of Sciences 96.15 (1999): 8330-8331.

[27] lander, Arne. "An electrochemical investigation of solid cadmium-gold alloys." Journal of the American Chemical Society 54.10 (1932): 3819-3833.

[28] Tadaki, T., K. Otsuka, and K. Shimizu. "Shape memory alloys." Annual Review of Materials Science 18.1 (1988): 25-45.

[29] Mavroidis, Constantinos, Charles Pfeiffer, and Michael Mosley. "5.1 conventional actuators, shape memory alloys, and electrorheological fluids." Automation, miniature robotics, and sensors for nondestructive testing and evaluation 4 (2000): 189.

[30] Van Humbeeck, Jan. "Non-medical applications of shape memory alloys." Materials Science and Engineering: A 273 (1999): 134-148.

[31] Schlumberger, Limited. Shape memory alloy technology. cameron.slb.com. 2017. Web. 26 Feb. 2017.

[32] Schetky, L. McDonald. "ShapeMemory Alloys." Kirk-Othmer Encyclopedia of Chemical Technology (1982).

[33] Kundys, B. "Photostrictive materials." Applied Physics Reviews 2.1 (2015): 011301.

[34] Crawley, Edward F., and Javier De Luis. "Use of piezoelectric actuators as elements of intelligent structures." AIAA journal 25.10 (1987): 1373-1385.

[35] Uchino, Kenji. "Piezoelectric ultrasonic motors: overview." Smart materials and structures 7.3 (1998): 273.

[36] Physikinstrumente, Selection guide: linear flexure stages and actuators/nanopositioning systems, http://www.physikinstrumente.com/en/products/nanopositioning/nanopositioninglinear-stage selection.php (2012)

[37] Hemsel, Tobias, and Jrg Wallaschek. "Survey of the present state of the art of piezoelectric linear motors." Ultrasonics 38.1 (2000): 37-40.

[38] Yao, Qing, J. Dong, and Placid M. Ferreira. "Design, analysis, fabrication and testing of a parallel-kinematic micropositioning XY stage." International Journal of Machine Tools and Manufacture 47.6 (2007): 946-961.

[39] Leleu, Sylvaine, Hisham Abou-Kandil, and Yvan Bonnassieux. "Piezoelectric actuators and sensors location for active control of flexible structures." Instrumentation and Measurement Technology Conference, 2000. IMTC 2000. Proceedings of the 17th IEEE. Vol. 2. IEEE, 2000.

[40] Grossard, M., et al. "Flexible building blocks method for the optimal design of compliant mechanisms using piezoelectric material." 12th IFToMM World Congress. 2007.

[41] Chu, ZhongYi, and Jing Cui. "Experiment on vibration control of a two-link flexible manipulator using an input shaper and adaptive positive position feedback." Advances in Mechanical Engineering 7.10 (2015): 1687814015610466.

[42] Tian, Yanling, Bijan Shirinzadeh, and D. Zhang. "A flexure-based mechanism and control methodology for ultra-precision turning operation." Precision Engineering 33.2 (2009): 160-166.

[43] Eaton, Peter. AFM Artifacts-Scanner Artifacts - Effects due to the peculiarities of the piezoelectric scanner. http://www.fc.up.pt/. Mar. 2007. Web. 26 Feb. 2017.

[44] Yong, Y. K., et al. "Multivariable Control Designs for Piezoelectric tubes." IFAC Proceedings Volumes 44.1 (2011): 2030-2035.

[45] Xu, Qingsong. "Intelligent Hysteresis Modeling and Control of Piezoelectric Actuators." Smart Materials-Based Actuators at the Micro/Nano-Scale. Springer New York, 2013. 171-185.

[46] Ge, Ping, and Musa Jouaneh. "Generalized Preisach model for hysteresis nonlinearity of piezoceramic actuators." Precision engineering 20.2 (1997): 99-111.

[47] Su, Chun-Yi, et al. "Adaptive variable structure control of a class of nonlinear systems with unknown Prandtl-Ishlinskii hysteresis." IEEE Transactions on automatic control 50.12 (2005): 2069-2074.

[48] Al Janaideh, Mohammad, et al. "Generalized Prandtl-Ishlinskii hysteresis model: Hysteresis modeling and its inverse for compensation in smart actuators." Decision and Control, 2008. CDC 2008. 47th IEEE Conference on. IEEE, 2008.

[49] Croft, Donald, G. Shedd, and Santosh Devasia. "Creep, hysteresis, and vibration compensation for piezoactuators: atomic force microscopy application." American Control Conference, 2000. Proceedings of the 2000. Vol. 3. IEEE, 2000.

[50] Mokaberi, Babak, and Aristides AG Requicha. "Compensation of scanner creep and hysteresis for AFM nanomanipulation." IEEE Transactions on Automation Science and Engineering 5.2 (2008): 197-206.

[51] "Hysteresis and Aging." Hysteresis and Aging-SPM Training Guide. N.p., n.d. Web. 26 Feb. 2017.

[52] Devasia, Santosh, Evangelos Eleftheriou, and SO Reza Moheimani. "A survey of control issues in nanopositioning." IEEE Transactions on Control Systems Technology 15.5 (2007): 802-823.

[53] Tamer, Nabil, and Mohammad Dahleh. "Feedback control of piezoelectric tube scanners." Decision and Control, 1994., Proceedings of the 33rd IEEE Conference on. Vol. 2. IEEE, 1994.

[54] Chu, ZhongYi, and Jing Cui. "Experiment on vibration control of a two-link flexible manipulator using an input shaper and adaptive positive position feedback." Advances in Mechanical Engineering 7.10 (2015): 1687814015610466.

[55] Tuma, Tomas, et al. "A Hybrid Control Approach to Nanopositioning." Smart Materials-Based Actuators at the Micro/Nano-Scale. Springer New York, 2013. 89-120.

[56] Bashash, Saeid, and Nader Jalili. "Robust adaptive control of coupled parallel piezo-flexural nanopositioning stages." IEEE/ASME Transactions on mechatronics 14.1 (2009): 11-20.

[57] Zhong, Jinghua, and Bin Yao. "Adaptive robust precision motion control of a piezoelectric positioning stage." IEEE Transactions on Control Systems Technology 16.5 (2008): 1039-1046.

[58] Vaughan, Joshua, Aika Yano, and William Singhose. "Comparison of robust input shapers." Journal of Sound and Vibration 315.4 (2008): 797-815.

[59] Jos L. Pons, 'Emerging actuator technologies : a micromechatronic approach', Wiley, ISBN 0-470-09197-5, 2005.

[60] Micky Rakotondrabe, Alexandru Ivan, Sofiane Khadraoui, Philippe Lutz and Nicolas Chaillet, 'Simultaneous displacement and force self-sensing in piezoelectric actuators and applications to robust control of the displacement', IEEE/ASME - Transactions on Mechatronics (T-mech), Vol 20, No 2, Page 519 - 531, April 2015.

[61] Ioan Alexandru Ivan, Omar Aljanaideh, Jol Agnus, Philippe Lutz and Micky Rakotondrabe, 'Quasi-static displacement self-sensing measurement for a 2-DOF piezoelectric cantilevered actuator', IEEE - Transactions on Industrial Electronics (TIE), DOI.10.1109/TIE.2017.2677304, 2017.

[62] Fairweather, J.A. (1998). Designing with Active Materials: An Impedance Based Approach, Ph.D. Thesis. Rensselaer Polytechnic Institute, New York.

[63] Carol Livermore, course materials for 6.777J / 2.372J Design and Fabrication of Microelectromechanical Devices, Spring 2007. MIT OpenCourseWare (http://ocw.mit.edu/), Massachusetts Institute of Technology. Downloaded on [19 March 2017].

[64] L. Que, J. S. Park and Y. B. Gianchandani, "Bent-beam electrothermal actuators for high force applications," Technical Digest. IEEE International MEMS 99 Conference. Twelfth IEEE International Conference on Micro Electro Mechanical Systems (Cat. No.99CH36291), Orlando, FL, USA, 1999, pp. 31-36.

[65] Jae-Sung Park, L. L. Chu, A. D. Oliver and Y. B. Gianchandani, "Bent-beam electrothermal actuators-Part II: Linear and rotary microengines," in Journal of Microelectromechanical Systems, vol. 10, no. 2, pp. 255-262, Jun 2001.

[66] Izhar, U., A. B. Izhar, and S. Tatic-Lucic. "A multi-axis electrothermal micromirror for a miniaturized OCT system." Sensors and Actuators A: Physical 167.2 (2011): 152-161.

[67] Sehr, H., et al. "Time constant and lateral resonances of thermal vertical bimorph actuators." Journal of Micromechanics and Microengineering 12.4 (2002): 410.

[68] Guo, Hui, and Haixia Zhang. "A novel electro-thermal actuated micro position lock." Solid-State and Integrated Circuits Technology, 2004. Proceedings. 7th International Conference on. Vol. 3. IEEE, 2004.

[69] Syms, R. R. A., et al. "Multistate latching MEMS variable optical attenuator." IEEE Photonics Technology Letters 16.1 (2004): 191-193.

[70] Bollee, B. "Electrostatic motors(Synchronous and asynchronous electrostatic motors based on action of electric fields charges, discussing design and construction)." Philips technical review 30.6 (1969): 178-194.

[71] Horsley, David A., Roberto Horowitz, and Albert P. Pisano. "Microfabricated electrostatic actuators for hard disk drives." IEEE/ASME transactions on mechatronics 3.3 (1998): 175-183.

[72] "Kinetic Energy Harvesting by Magnetostrictive Materials." Sigma-Aldrich. Daniele Davino, n.d. Web. 20 Mar. 2017.

[73] D. Croft G. Shed S. Devasia "Creep hysteresis and vibration compensation for piezoactuators: Atomic force microscopy application", ASME J. Dyn. Syst. Control vol. 123 no. 1 pp. 35-43 Mar. 2001.

[74] I.D. Mayergoyz, "Mathematical Models of Hysteresis", Springer, ISBN-13: 978-1461277675, 1991.

[75] M. A. Krasnoselskii and A. V. Pokrovskii, "Systems with hysteresis", Springer-Verlag, Berlin, 1989

[76] R. Wiesendanger, Scanning Probe Microscopy and Spectroscopy. Cambridge, U.K.: Cambridge Univ. Press, 1994.

[77] S. M. Salapaka and M. V. Salapaka, "Scanning probe microscopy," *IEEE Control Systems Magazine*, vol. 28, no. 2, pp. 65–83, 2008.

[78] D. Croft and S. Devasia, "Vibration compensation for high speed scanning tunneling microscopy", Rev. Sci. Instr., vol. 70, no. 12, pp.46004605, Dec. 1999.

[79] X. Tan and J.S. Baras, Adaptive identification and control of hysteresis in smart mate-rials, IEEE Trans. Automat. Contr., vol. 50, no. 6, pp. 827839, 2005. [26] E. Bayo, A fi-nite-element approach to control the end-point motion of a single-link flexible robot, J. Ro-botic Syst., vol. 4, pp. 6375, 1987.

[80] D. Kwon and W. J. Book, An inverse dynamic method yielding flexible manipulator state trajectories, ASME J. Dyna. Syst., Meas., Control, vol. 116, no. 2, pp. 193200, 1990.

[81] S. Devasia, D. Chen, and B. Paden, Nonlinear inversion-based output tracking, IEEE Trans. Automat. Contr., vol. 41, pp.930943, July 1996.

[82] L. R. Hunt, G. Meyer, and R. Su, Noncausal inverses for linear systems, IEEE Trans. Automat. Contr., vol. 41, pp. 608611, Apr. 1996.

[83] L. R. Hunt, V. Ramakrishna, L. R. Hunt, and G. Meyer, Stable inversion and parame-ter variations, Syst. Control Lett., vol. 34, pp. 203207, 1998.

[84] V. Ramakrishna, L. R. Hunt, and G. Meyer, Parameter variations, relative degree, and stable inversion, Automatica, vol.37, pp.871880,2001.

[85] Tomizuka, M., 1987, "Zero Phase Error Tracking Algorithm for Digital Control," ASME Journal of Dynamic Systems, Measurement, and Control, Vol. 109, pp. 65-68.

[86] H. S. Park, P.H. Chang and D.Y. Lee, "Continuous zero phase error tracking controller with gain error compensation", Proc. of the American Control Conference, vol. 5, pp. 3554-3558

[87] Singh, T. and Vadali, S. R., 1993, Robust Time-Delay Control, ASME J. of Dynamic Systems, Measurement, and Control, Vol. 115, pp. 303-306.

[88] O.J.M. Smith, Posicast Control of Damped Oscillatory Systems, Proceedings of the IRE, 1957, pp.1249-1255

[89] T. Singh and W. Singhose, "Input shaping/time delay control of maneuvering flexible structures," Proceedings of the 2002 American Control Conference (IEEE Cat. No.CH37301), Anchorage, AK, USA, 2002, pp. 1717-1731 vol.3.

[90] M. J. Robertson and W. E. Singhose, Closed-Form Deflection-Limiting Commands, American Control Conference, Portland, USA, 2005, pp.2104-2109

[91] N.C. Singer and W.P. Seering, Preshaping Command Inputs to Reduce System Vibration, Journal of Dynamic Systems, Measurement and Control, 112, 1990, pp.76-82

[92] W. Singhose, E. Crain and W. Seering, Convolved and Simultaneous Two-Mode Input Shapers, IEE Proc. Control Theory Appl., Vol. 144, No. 6, 1997, pp.515-520

[93] W. Singhose and N. Singer, Effects of Input Shaping on Two-Dimensional Trajectory Following, IEEE Trans. on Robotics and Automation, Vol. 12, No. 6, 1996, pp.881-887

[94] Chang, K. Godbole and E. Hou, Optimal Input Shaper Design for High-Speed Robotic Workcells, J. Vibration and Control, Vol. 9, 2003, pp.13591376

[95] Singhose, William, and L. Pao. "A comparison of input shaping and time-optimal flexible-body control." Control Engineering Practice 5.4 (1997): 459-467.

[96] C. F. Cutforth and L. Y. Pao, Control Using Equal Length Shaped Commands to Reduce Vibration, IEEE Trans. on Control Sys. Tech., Vol. 11, No. 1, 2003, pp.62-72

[97] Baumgart, Matthew D., and Lucy Y. Pao. "Cooperative multi-input shaping for arbitrary inputs." American Control Conference, 2001. Proceedings of the 2001. Vol. 1. IEEE, 2001.

[98] Tuttle, T.D. and Seering,W.P., 1994, A zero-placement technique for designing shaped inputs to suppress multiplemode vibration, in Proceedings of the American Control Conference, Baltimore, MD, pp. 25332537

[99] Singhose, W., N. Singer and W. Seering, (1994b). Design and implementation of time-optimal negative input shapers, Intl. Mechanical Engineering Congress and Exposition, DSC 55-1, Chicago, IL, 151-7.

[100] Singhose, W., N. Singer and W. Seering, (1995). Comparison of command shaping methods for reducing residual vibration, Third European Control Conf., Rome, Italy, 2, 1126-1131.

[101] Singhose, W.E. and Mills, IV.W., 1999, Command generation using specified-negative amplitude input shapers, in Proceedings of the American Control Conference, San Diego, CA, pp. 6165

[102] Park, IV.J., Lee, J.W., Lim, IV.D., and Sung, Y.G., 2001, Design and sensitivity analysis of an input shaping filter in the z-plane, Journal of Sound and Vibration 243, 157171

[103] J. Shan, H.-T. Liu, D. Sun, Modified input shaping for a rotating single-link flexible manipulator, Journal of Sound and Vibration 285 (12) (2005) 187207

[104] Grleyk S.S., Optimal Unity-Magnitude Input Shaper Duration Analysis, Archive of Applied Mechanics, Vol.77, No.1, 2007, pp.63-71.

[105] Grleyk S.S., Hacolu R. ve Cinal ., Three-Step Input Shaper for Damping Tubular Step Motor Vibrations, J. of Mechanical Engineering Science, Vol. 221, No.1, 2007, pp.1-9.

[106] Grleyk, Sirri Sunay, et al. "Improved three-step input shaping control of crane system." constraints 6 (2008): 10.

[107] W. Singhose, W. Seering, N. Singer, Residual vibration reduction using vector diagrams to generate shaped inputs, Journal of Mechanical Design 116 (2) (1994) 654659.

[108] W.E. Singhose, L.J. Porter, T.D. Tuttle, N.C. Singer, Vibration reduction using multi-hump input shapers, ASME Journal of Dynamic Systems Measurement and Control 119 (2) (1997) 320326.

[109] Kenison, M. and Singhose, W. ,Concurrent Design of Input Shaping and Feedback Control for Insensitivity to Parameter Variations, Sixth Int. Workshop on Advanced Motion Control, Nagoya, Japan, 2000.

[110] Kenison, M. and Singhose, W., Concurrent Design of Input Shaping and Proportional Plus Derivative Feedback Control, Accepted to the ASME J. of Dynamic Systems, Measurement, and Control.

[111] Bhat, S.P.; Miu, D.K. Solutions to Point-to-Point Control Problems Using Laplace Transform Technique. ASME J. Dyn. Syst. Meas. Control 1991, 113, 425431.

[112] Hyde, J.M.; Seering, W.P. Using Input Command Pre-Shaping to Suppress Multiple Mode Vibration. In Proceedings of the IEEE Robotics and Automation Conference, Sacramento, CA, USA, 911 April 1991; pp. 26042609.

[113] Rappole, B.W.; Singer, N.C.; Seering, W.P. Multiple-Mode Input Shaping Sequences for Reducing Residual Vibrations. In Proceedings of the 23rd Biennial Mechanisms Conference, Minneapolis, MN, USA, 1114 Sep-tember 1994; pp. 1116.

[114] Singh, T.; Vadali, S.R. Robust Time-Optimal Control: A Frequency Domain Approach. Proc. AZAA Guid. Navig. Control Conf. 1994, doi:10.2514/6.1994-3569.

[115] D. Liu, Y. Daming, and Z. Weiping, On optimal control strategy of maneuver of satellites with flexible appendages, in Proc. PISSTA, Beijing, China, June 710, 1987, pp. 530539

[116] Pao, L.Y. Multiple Input-Shaping Design for Vibration Reduction. Automatica 1999, 35, 8189.

[117] Al Hamidi, Y.; Rakotondrabe, M. Multi-Mode Vibration Suppression in 2-DOF Piezoelectric Systems Using Zero Placement Input Shaping Technique. Proc. SPIE 2015, 9494, doi:10.1117/12.2185683.

[118] Santosh, D.; Evangelos, E.; Moheimani, S.O.R. A Survey of Control Issues in Nanopositioning. IEEE Trans. Con-trol Syst. Technol. 2007, 15, 802823.

[119] Cutforth, C. F. and L. Y. Pa0 (1999). A Modified Method for Multiple Actuator Input Shaping. Proc. of the American Control Conf., San Diego, CA, pp. 66-70.

[120] K. K. Leang, Q. Zou and S. Devasia, "Feedforward control of piezoactuators in atomic force microscope systems," in IEEE Control Systems, vol. 29, no. 1, pp. 70-82, Feb. 2009.

[121] Astrom, K. J., Hagander, P., and Sternby, J., 1984, Zeros of Sampled Systems, Autornatica, Vol. 20, No. 1, pp. 31-38.

[122] B. P. Rigney, L. Y. Pao, and D. A. Lawrence, Nonminimum phase dynamic inversion for settle time applications, Provisionally accepted for publication in: IEEE Trans. Ctrl. Sys. Tech., 2008.

[123] J. A. Butterworth, L. Y. Pao and D. Y. Abramovitch, "The effect of nonminimum-phase zero locations on the performance of feedforward model-inverse control techniques in discrete-time systems," 2008 American Control Conference, Seattle, WA, 2008, pp. 2696-2702.

[124] Magee, D. and Book, W., The Application of Input Shaping to a System with Varying Parameters, Japan/USA Symposium on Flexible Automation, 1992.

[125] Singh, G., Kabamba, P. T., McClamroch, N. H., 1989, Planar, Time-Optimal, Rest-to-Rest Slewing Maneuvers of Flexible Spacecraft, J. of Guidance, Control, and Dynamics, Vol. 12, No. 1, pp 71-81.

[126] Ben-Asher, J., Burns, J. A. and Cliff, E. M., 1992, Time-Optimal Slewing of Flexible Spacecraft, J. of Guidance, Control, and Dynamics, Vol. 15(2), pp. 360-367.

[127] Liu, Q. and Wie, B., 1992, Robust Time-Optimal Control of Uncertain Flexible Spacecraft, J. of Guidance, Control, and Dynamics, Vol. 15(3), pp. 597-604

[128] Hartmann, R., and Singh, T., Fuel/Time Optimal Control of Flexible Structures: A Frequency Domain Approach, Journal of Vibration and Control, Sept., 1999, Vol. 5, No. 5, pp 795-817.

[129] Singhose, William. "Command shaping for flexible systems: A review of the first 50 years." International Journal of Precision Engineering and Manufacturing 10.4 (2009): 153-168.

[130] Singhose, W., Bohlke, K. and Seering, W. Fuel-Efficient Pulse Command Profiles for Flexible Spacecraft, J. of Guidance, Control, and Dynamics, Vol. 19, pp. 954-960, 1996.

[131] Singh, T., Fuel/Time Optimal Control of the Benchmark Problem, J. of Guidance, Control, and Dynamics, Vol. 18, pp. 1225-1231, 1995.

[132] Wie, B., Sinha, R., Sunkel, J. and Cox, K., Robust Fuel- and Time-Optimal Control of Uncertain Flexible Space Structures, Proc. Guidance, Navigation, and Control Conference, pp. 939-948, 1993.

[133] Singhose, W., Singh, T. and Seering, W., On-Off Control with Specified Fuel Usage, Journal Dynamic Systems, Measurement, and Control, Vol. 121, pp. 206- 212, 1999.

[134] Singhose, W., Banerjee, A. and Seering, W., Slewing Flexible Spacecraft with Deflection-Limiting Input Shaping, J. of Guidance, Control, and Dynamics, Vol. 20, pp. 291-298, 1997.

[135] Tzes, A. P. and Yurkovich, S., Adaptive Precompensators for Flexible-Link Manipulator Control, 28th IEEE Conference on Decision and Control, Vol. 3, pp. 2083-2088, 1989.

[136] Tzes, A. and Yurkovich, S., An Adaptive Input Shaping Control Scheme for Vibration Suppression in Slewing Flexible Structures, IEEE Transactions on Control Systems Technology, Vol. 1, pp. 114-121, 1993.

[137] Khorrami, F., Jain, S. and Tzes, A., Experiments of Rigid-Body Based Controllers with Input Preshaping for a Two-Link Flexible Manipulator, Proc. American Control Conf., pp. 2957-2961, 1992.

[138] Khorrami, F., Jain, S. and Tzes, A., Adaptive Nonlinear Control and Input Preshaping for Flexible-Link Manipulators, Proc. American Control Conf., pp. 2705-2709, 1993.

[139] Rhim, S. and Book, W., Adaptive Time-delay Command Shaping Filter for Flexible Manipulator Control, IEEE/ASME Trans. on Mechatronics, Vol. 9, pp. 619-626, 2004.

[140] Park, J. and Rhim, S., Extraction of Optimal Time-delay in Adaptive Command Shaping Filter for Flexible Manipulator Control, J. of Inst. of Control, Robotics and System, Vol. 14, pp. 564-572, 2008.

[141] Rhim, S. and Book, W., Adaptive Command Shaping Using Adaptive Filter Approach in Time Domain, Proc. American Control Conference, pp. 81-85, 1999.

[142] Rhim, S. and Book, W., Noise Effect on Time-domain Adaptive Command Shaping Methods for Flexible Manipulator Control, IEEE Trans. of Control Systems Technology, Vol. 9, pp. 84-92, 2001.

[143] N. C. Singer and W. P. Seering, "An extension of command shaping methods for controlling residual vibration using frequency sampling," Proceedings 1992 IEEE International Conference on Robotics and Automation, Nice, 1992, pp. 800-805 vol.1.

[144] Singhose, William E., Warren P. Seering, and Neil C. Singer. "Input shaping for vibration reduction with specified insensitivity to modeling errors." Japan-USA Sym. on Flexible Automation 1 (1996): 307-13.

[145] J. Agnus, P. De Lit and N. Chaillet, 'Micromanipulateur pizolectrique notamment pour microrobotique', french Patent, FR0211934, 2002.

[146] Jol Agnus, Nicolas Chaillet, Cdric Clvy, Sounkalo Dembl, Michal Gauthier, Yassine Haddab, Guillaume Laurent, Philippe Lutz, Nadine Piat, Kanty Rabenorosoa, Micky Rakotondrabe and Brahim Tamadazte,

'Robotic Microassembly and micromanipulation at FEMTO-ST', Journal of Micro-Bio Robotics (JMBR), Volume 8, Issue 2, Page 91-106, 2013.

[147] L. Ljung, "System identification toolbox 7 user's guide," The Mathworks, Natick, MA USA, Oct. 2008.

[148] M. Rakotondrabe, K. Rabenorosoa, J. Agnus and N. Chaillet, "Robust feedforward-feedback control of a nonlinear and oscillating 2-DOF piezocantilever," *IEEE Transactions on Automation Science and Engineering*, vol. 8, no. 3, pp. 506–519, July 2011.

[149] Mohand-Ousaid, Abdenbi, et al. "Design, static modeling and simulation of a 5-DOF precise piezoelectric positioner." SPIE Commercial+ Scientific Sensing and Imaging. International Society for Optics and Photonics, 2016.

[150] De Lit, Pierre, et al. "A four-degree-of-freedom microprehensile microrobot on chip." Assembly Automation 24.1 (2004): 33-42.

[151] https://pharm.virginia.edu/facilities/atomic-force-microscope-afm/

[152] K.H. Martin, B.D. Lindsey, J. Ma, M. Lee, S. Li, F.S. Foster, X. Jiang, P.A. Dayton "Dual-frequency piezoelectric transducers for contrast enhanced ultrasound imaging Sensors", 14 (2014), pp. 20825-20842

[153] Micky Rakotondrabe, 'Piezoelectric cantilevered structures: modeling control and measurement/estimation aspects', Springer - Verlag, Monography in preparation.

[154] A.E. El-Shaer, M. Al Janaideh, P. Krejci and M. Tomizuka, "Robust Performance Enhancement Using Disturbance Observers for Hysteresis Compensation Based on Generalized PrandtlIshlinskii Model", ASME Journal of Dynamic Systems, Measurement, and Control, 135, 2013.

[155] F.L. Lewis, D. Vrabie, V.L. Syrmos, "Optimal control", Wiley, ISBN: 978-0-470-63349-6, 2012.

[156] M. Rakotondrabe, J. Agnus and P. Lutz, "Feedforward and IMC-feedback control of a nonlinear 2-DOF piezoactuator dedicated to automated micropositioning tasks," in *2011 IEEE Conference on Automation Science and Engineering (CASE)*, Trieste, Italy, Aug. 2011, pp. 393–398.

[157] A. Hammerstein, "Nichtlineare Integralgleic hungen nebst Anwendungen", Acta Math, 54, pp.117-176, 1930.

[158] N. Wiener, "Nonlinear Problems in Random Theory", New York: Wiley, 1958.

[159] http://www.labex-action.fr/

[160] Tian-Bing Xu et al, U.S. patent Publication/application, 20100096949 (Published on 4/22/2010).

[161] Shashank Priya, Daniel J. Inman, "Energy Harvesting Technologies", Springer Verlag, ISBN: 978-0-387-76463-4, 2009.